DEVELOPMENT OF DOUBLE DRIFT HARMONIC BUNCHER CONCEPTS

DISSERTATION

zur Erlangung des Doktorgrades
der Naturwissenschaften

vorgelegt beim Fachbereich Physik
der Johann Wolfgang Goethe-Universität
in Frankfurt am Main

von

Ezgi Sunar
aus Istanbul, Türkei

Frankfurt am Main, 2023
(D30)

Contents

List of Tables

List of Figures

Kapitel 1

Zusammenfassung

Im Rahmen dieser Arbeit wurde ein verbessertes Buncher-System für Hochfrequenz-
beschleuniger mit niedrigem und mittlerem Ionenstrom entwickelt. Zunächst wird
das vorgeschlagene Konzept und die Beziehung seiner wesentlichen Parameter be-
schrieben. Die entwickelte Methodik hat ermöglicht, ein effektives, vereinfachtes
Buncher-System für die Injektion in HF-Beschleuniger wie RFQs, Zyklotrons, DTLs
usw. zu entwerfen, welches kleine Ausgangsemittanzen und beträchtliche Strahltrans-
missionen erzielt. Die Wirksamkeit und die Realisierungsmöglichkeit eines solchen
Systems wurde mit drei unterschiedlichen Strahlströmen (0, 10, 30 mA) und zwei
Eingangsenergien (60, 100 keV) bei derselben Grundfrequenz von 54 MHz untersucht.
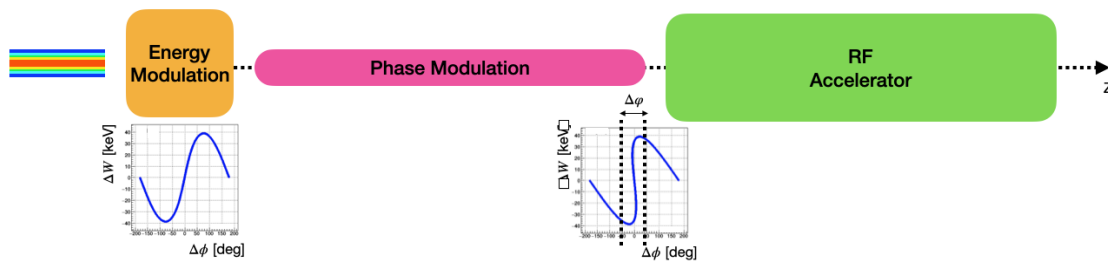
Abbildung 1.1: Schema eines Buncher-Systems, beginnend mit einem Gleichstrom-
strahl, vor einem HF-Beschleuniger.

Wie das Prinzip der Bunch-Formierung im Schema in Abbildung 1.1 zeigt, besteht
der vordere Teil einer Beschleunigerlinie aus Kavitäten mit harmonischen Spannungen
zur Energiemodulation und Driftstrecken zur Längsfokussierung. Daher kann eine
geeignete Kombination von Kavitäten und Driften die Erzeugung von Teilchenpulsen
ergeben, welche von dem nachfolgenden Hochfrequenzbeschleuniger akzeptiert wer-

1

den. Durch Eine Sägezahnwellenform wird die ideale Energiemodulation aufgrund der linearen Abhängigkeit zwischen der Energie der Teilchen und ihren relativen Phasen erreicht. Aufgrund der Einschränkungen der aktuellen Technologie hinsichtlich der in Teilchenbeschleunigern erforderlichen Leistungsniveaus (im kV bis 100 kV Bereich) ist die ideale Alternative einer sägezahnförmigen Hochfrequenzanregung eines einzelnen Resonators jedoch keine Option. Dagegen ist für eine solche Zielsetzung eine räumliche Trennung der sinusförmigen Anregung mit der Grundfrequenz und höheren Harmonischen möglich. Daher wurde in dieser Arbeit ein verbesserter harmonischer Buncher, der sogenannte „Double Drift Harmonic Buncher - DDHB" entwickelt, welcher zahlreiche Vorteilen hat. Eine geringe longitudinale Emittanz sowie finanzielle Aspekte sprechen für diesen Lösungsansatz
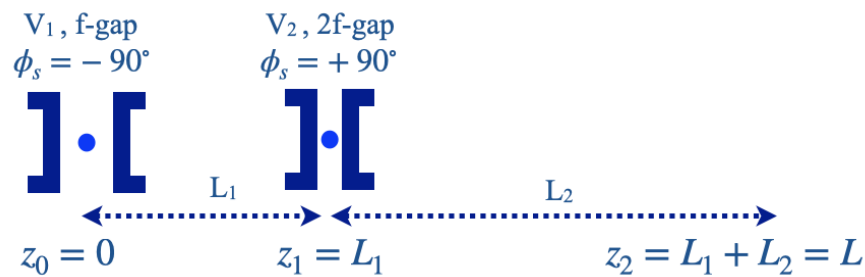
Abbildung 1.2: Schema des DDHB mit vier spezifischen Parametern.

Wie im Schema in Abbildung 1.2 gezeigt, sind die Hauptelemente zwei Kavitäten, die durch eine Driftlänge L_1 getrennt sind, wobei der erste Resonator mit der Grundfrequenz von $-90°$ synchroner Phase und angelegter Spannung V_1 und der zweite Resonator bei der zweiten harmonischen Frequenz mit $+90°$ synchroner Phase und angelegter Spannung V_2 betrieben werden. Schließlich ist eine zweite Drift L_2 am Ende des Arrays für eine longitudinale Strahlfokussierung am Hauptbeschleunigereingang erforderlich. Abbildung 1.3 veranschaulicht diese beschriebenen Schritte. Somit erfüllt ein solcher Aufbau das angestrebte Ziel einer hohen Einfangeffizienz und einer kleinen longitudinalen Emittanz durch Anpassen der vier Designparameter V_1, L_1, V_2 und L_2. Darüber hinaus könnten bei Vorhandensein von höheren Strahlströmen die Bunch-Ergebnisse durch die raumladungskräfte sogar vorteilhaft beeinflusst werden. Was die Raumladung betrifft, verhält sich der Kern der Strahlverteilung nach der Erzeugung der anfänglichen Bunch-Formierung anders als der Rand. Da sich die
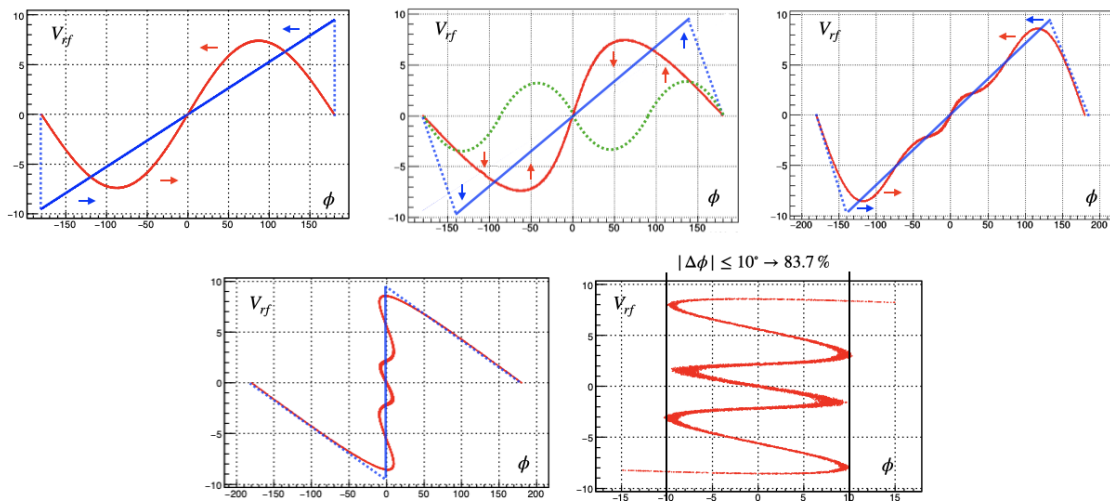
Abbildung 1.3: Die Grafiken zeigen den Mechanismus des DDHB-Konzepts. In diesem Beispiel ergibt die geforderte Phasenbreite $\pm 10°$ eine Akzeptanz von $\sim 84\%$ der als Gleichstrom einfallenden Teilchen.

Geschwindigkeit der Randteilchen relativ stark von der des Kerns unterscheidet (aufgrund der Energieverteilung der Teilchen), können sie unter Raumladung eine eigene Dynamik entfalten. Andererseits wirkt die Raumladungskraft der Bündelung im Kern entgegen, sodass sich die Kernverteilung langsamer bewegt als die äußeren Teile des Strahls. Diese Untersuchung des vorgeschlagenen harmonischen Doppeldriftbunchers bietet großes Potenzial für die Verbesserung der Ergebnisse und die Vereinfachung des Aufbaus.

Das Verständnis des Fokussierung, ausgehend von einem Gleichstromstrahl, einschließlich der Raumladungskräfte, ist einer der wesentlichen Bestandteile der Strahlphysik. Viele kommerzielle Codes (z.B. LORASR [1], TraceWin [2]) bieten Simulationsmöglichkeiten in diesem Anwendungsbereich; Ihre Ansätze bleiben jedoch meist verborgen. Mit anderen Worten: Ein Benutzer kann nicht wissen, welche Art von Operation dieses Programm verwendet. Daher bestand eine Hauptaufgabe dieser Arbeit darin, einen speziellen Multi-Particle-Tracking-Beam-Dynamics-Code (BCDC) zu entwickeln, bei dem der Raumladungseffekt während des Bunch-Vorgangs, ausgehend von einem DC-Strahl berechnet wird. Der BCDC-Code enthält elementare Routinen wie Drift und Beschleunigungsspalt oder magnetische Linse für die transversale Strahlfokussierung und Raumladungsberechnungen unter Berücksichtigung der Auswirkungen der nächsten Nachbar-Bunche (NNB).
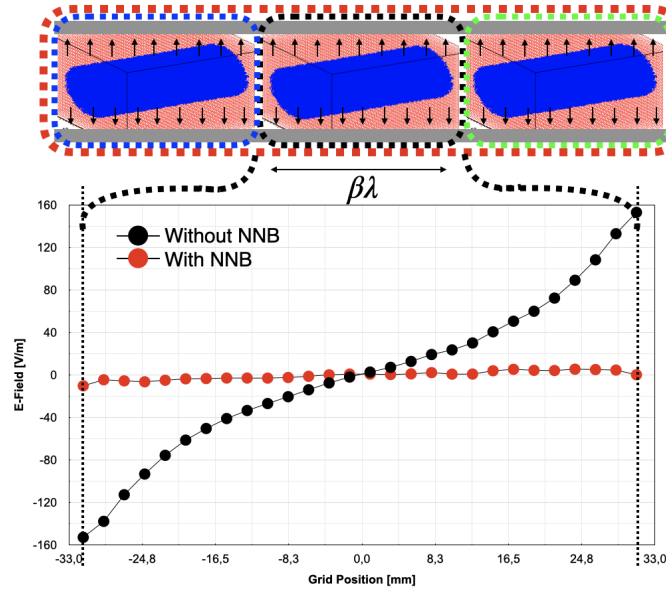
Abbildung 1.4: Die longitudinalen Feldberechnungen an einem Gleichstromstrahl ohne und mit dem NNB-Konzept für einen Strahlstrom von 0.5 mA.

Der Raumladungsalgorithmus in BCDC basiert auf einer direkten Coulomb-Gitter-Gitter-Wechselwirkung und Berechnungen des elektrischen Feldes durch Lokalisierung der Ladungsdichte auf einem kartesischen Gitter. Um Genauigkeit zu erreichen, werden die Feldberechnungen in Längsrichtung um das zentrale Bucket ($\beta\lambda$-Größe) erweitert, so dass das Simulationsfeld dreimal so groß ist symmetrisch. Die zentrale Partikelverteilung wird dann nach jedem Schritt in die benachbarten Buckets kopiert. Anschließend werden die resultierenden Felder im Hauptgitterfeld neu berechnet, indem die elektrischen Felder im Hauptgitterfeld mit denen aus benachbarten Regionen überlagert werden. Es ist offensichtlich, dass ein kontinuierlicher Strahl, keine Raumladungsfeldkomponente E_z hat. Das resultierende Feld ist jedoch ungleich Null, wenn man die zylindrische Verteilung auf die Länge $\beta\lambda$ reduziert, wie im Diagramm mit der schwarzen Kurve in Abbildung 1.4 gezeigt - ohne Berücksichtigung der Nachbar - Bunche. Ein solches unphysikalisches Ergebnis kann durch die Anwendung der NNB-Technik bereits weitgehend eliminiert werden, wobei das berechnete Feld in dieser Abbildung durch die rote Kurve dargestellt wird.

Darüber hinaus zeigt Abbildung 1.5 die Ergebnisse bei Abwesenheit (symbolisiert durch ein Dreieck) und Anwesenheit (gekennzeichnet durch einen Kreis) des NNB-Konzepts. Die Feldberechnungen wurden in einer Testsimulation für eine Reihe
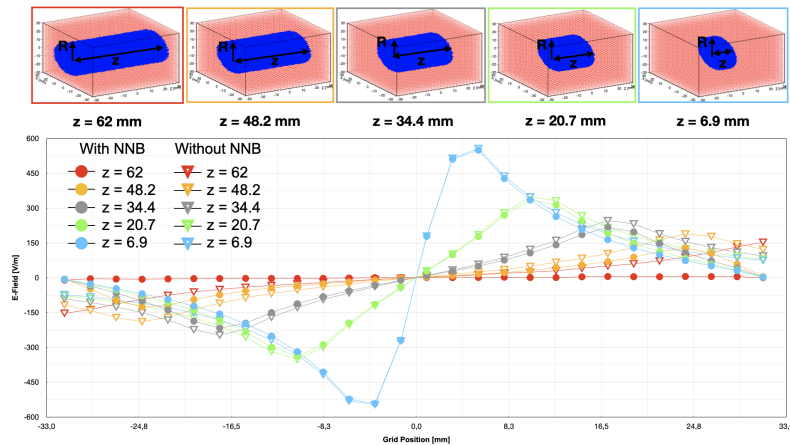
Abbildung 1.5: Die Auswirkungen auf die Feldberechnungen für unterschiedliche Strahlgrößen während der Strahlformierung, ohne und mit dem NNB-Konzept.

von Verteilungen mit unterschiedlichen Bunch-Längen durchgeführt für die Sequenz aus einem ungebündelten Strahl (rot) und durchgeführt. Die hohen E_z-Felder vier unterschiedlich langen Bunchen in der Nähe der bei $\pm\beta\lambda/2$ definierten Wände werden durch diese Methode drastisch reduziert, insbesondere für den Gleichstromstrahl (rot markiert). Zusammenfassend lässt sich sagen, dass das NNB-Konzept ein leistungsstarkes Werkzeug für Linac-Simulationen ist,Für die Berechnung der Bunch-Formierung aus einem Gleichstromstrahl ist es absolut notwendig. Andererseits kann man feststellen, dass die Mitnahme weiterer Nachbarbunche offensichtlich nur sehr kleine Zusatzkorrekturen bringt.

Zusätzlich zum NNB-Feature verfügt das BCDC über einen weiterer Besonderheit, nämlich die sogenannte Raumladungskompensation (SCC). Aufgrund der Ionisierung des Restgases kommt es entlang des Niederenergiestrahltransports zu einer teilweisen Raumladungskompensation, am und hinter dem Bunchersystem mit unterschiedlichen Prozentsätzen. Da eines der Hauptziele des DDHB-Konzepts darin besteht es, für Hochstromstrahlanwendungen zu entwickeln, ermöglicht die teilweise Raumladungskompensation, dass das Design, in der Praxis erreichbare höhere Stromniveaus erreicht. Dadurch ist das BCDC-Programm ein leistungsstarkes Werkzeug für Simulationen in künftigen, stromstarken Projekten, während Proof-of-Principle-Designs in dieser Arbeit entwickelt wurden.

Die Simulationen für verschiedene Anwendungen in der Arbeit zeigen, dass der

flexiblen Eigenschaften des Ausgangsstrahls ausschließlich unter Verwendung des DDHB-Konzepts erhalten werden. Das Entwurfsziel der in Kapitel 5 gezeigten Anwendungen besteht darin, abhängig vom folgenden HF-Beschleuniger eine hohe Teilchenakzeptanz und/oder eine schmale Phasenbreite zu erreichen. Während ein Anwendungsbeispiel mit einem 100 keV Protonenstrahl bei einer Grundfrequenz von 54 MHz für eine Zyklotroninjektion ausgewählt wurde, wurden zwei Beispiele mit 60 keV, 10 mA und 100 keV, 30 mA Protonenstrahlen bei derselben Frequenz ausgewählt für Hochstrom-Ionenstrahlanwendungen, wie ein RFQ oder eine DTL-Injektion. Bei der Zyklotroninjektion mit einem Niederstromstrahl wurde eine ausreichende Einfangrate von etwa 80% innerhalb einer schmalen Phasenbreite und einer akzeptablen Energiebreite von 2% erreicht, um eine transversale Defokussierung während des Beschleunigungsprozesses im Zyklotron zu vermeiden. Die beiden anderen Anwendungen mit Hochstromstrahlen bis zu 30 mA betreffen kompakte Bunch-Systeme mit Teilchenformierungen von etwa 70–80% in den Bereich von ±5° bis ±20° Phasenfokussierung. Im Fall der DTL-Injektion sind die Eigenschaften des Ausgangsstrahls eine akzeptable Teilchenübertragung für die Phasenbreiten von typisch ±5° oder ±10° bei in einer angemessenen Energieverteilung von $5 - 6\%$ erreicht worden. Bezüglich der Injektion in einen RFQ liefert ein Beispiel mit einem Strahlstrom von 10 mA einen Ausgangsstrahl mit einer beträchtlichen Einfangrate von 74% in einem bemerkenswerten verengten Phasenfenster von ±5°. Andere mit 30 mA erfüllen eine höhere Akzeptanz von 85% innerhalb ±20° Phasenbreite. Somit kann im Fall der RFQ-Injektion ein weites Spektrum von Pulsen mit unterschiedlichen Teilchenakzeptanzen angeboten werden.

Zur Erklärung des Schemas des DDHB-Konzepts zeigt Abbildung 1.6 die resultierende Struktur für das Bunchen eines 60 keV, 10 mA Protonenstrahls. Das obere Schema in der Abbildung stellt die transversale Strahlenveloppe und die transversalen Phasenraumverteilungen in der $XX'-$Ebene dar. Als wesentliche Elemente für den transversalen Fokus sind zwei Quadrupoltripletts in Permanentmagnetausführung vorgesehen. Die Diagramme in der Mitte und unten geben die Teilchenverteilungen in den longitudinalen Phasenraumclustern (in $X - Z$- und $\phi - W$-Ebenen) entlang der Struktur wieder. Während die Positionen mit den Nummern $P2$ und $P3$ die kritischen Orte sind, an denen die Bündelbildung innerhalb der Buncher-Kavitäten
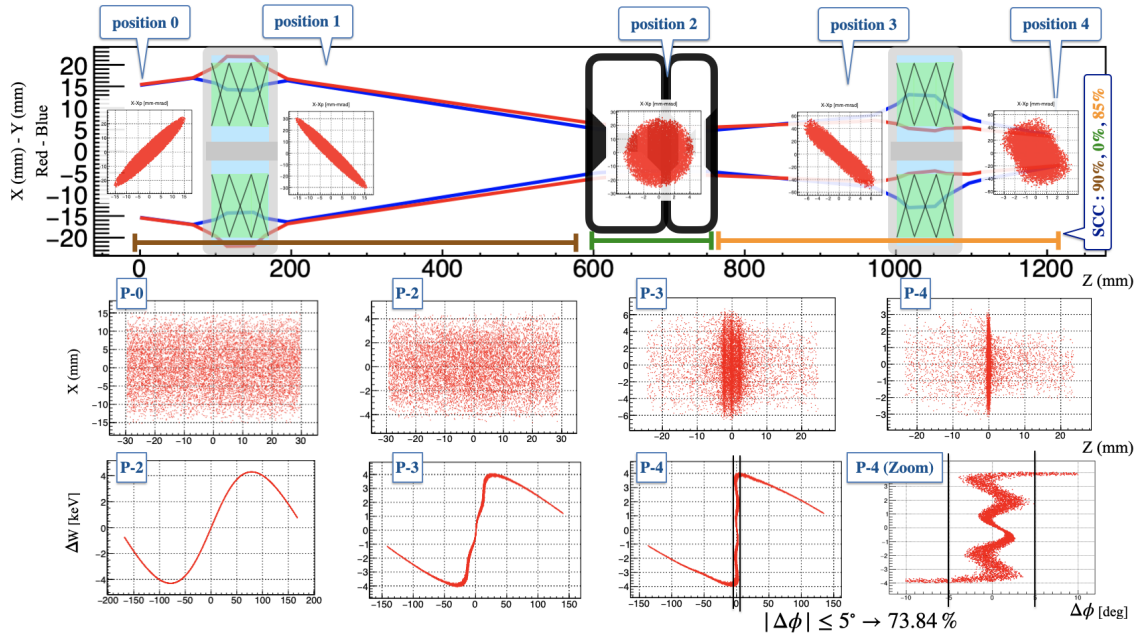
Abbildung 1.6: Beispiel eines mit dem BCDC-Code simulierten DDHB-Designs. Das Diagramm oben zeigt die transversale Strahlhülle für einen 60 keV- und 10 mA-Protonenstrahl und die transversalen Phasenraumverteilungen in der XX'-Ebene mit den angegebenen Positionen. Während die Diagramme in der Mitte die Teilchenverteilungen in der $X-Z$-Ebene an markierten Positionen veranschaulichen, zeigen die Diagramme unten die Teilchenverteilung an den angegebenen vier Orten.

stattfindet, zeigt das Diagramm mit der Nummer $P4$ den fokussierten Strahl am Ende der Struktur. Die Wirkung der zweiten Driftstrecke zur Bunch - Formierung wird hier deutlich sichtbar. Da eine typische RFQ-Phasenbreite etwa $\pm 25°$ beträgt, kann das Design mit dem DDHB-Konzept ein viel kleineres Phasenfenster bereitstellen als der RFQ, alleine. Die Kombination aus externem Buncher und RFQ soll mit dieser Arbeit zusätzlich motiviert werden.

7

Chapter 2

Introduction

Particle accelerators can be divided into two classes which are electrostatic and radio-frequency (RF) accelerators. In the initial type, the acceleration is provided by an electrostatic field, constant in time; however, the accessible peak energy is limited by the maximum terminal voltage due to field emission and the related voltage breakdown. The RF accelerators are based on oscillating electromagnetic fields, i. e. they lean on radio-frequency alternating fields that change periodically over time. The latter is more convenient for high-energy and high-intensity particle experiments.

The history of particle accelerators started with experiments in nuclear physics in 1920 [3]. The first attempts at particle accelerators had poor outcomes concerning beam quality, where a lack of exit beam energy or particle transmission could be two examples. Due to requirements for higher energetic beams, the first resonant accelerators were invented and operated by Widerøe, while another concept was developed by Alvarez [4]. An Alvarez-type LINear ACcelerator (linac) structure consists of a series of drift tubes put in a large metallic cylindrical tank. The end plates of the tank oscillate against each other at the full RF voltage amplitude. The drift tube structure divides the full voltage into portions of the individual gap voltages. The drift tubes placed at a distance $d = \beta\lambda$ (where $\beta = \frac{\nu}{c}$ is the relative particle velocity) have a shielding function for the particles that would experience the decelerating phase of the applied voltage. This concept provides stable motion only in the beam propagation direction (the so-called longitudinal plane), so the loss of many particles is inevitable during acceleration due to the lack of transversal

9

focusing of the beam.

In 1950, N. C. Christofilos [5], in first, and E. D. Courant, and H.S. Snyder [6,7], in parallel, presented an alternating-gradient (AG) focusing technique provided by small quadrupole magnets along the beam line as a solution. The idea was to use alternating convergent and divergent magnets, which leads to a net beam-focusing effect in both transverse directions. With the contribution of these geometrical optics, the beam transmission could be improved substantially. In addition, Blewett [8] proposed inserting the quadrupoles into the drift tubes. Consequently, the beginning of the acceleration process has been redefined with supplementary concepts for focusing mechanisms in the transverse and longitudinal planes to fulfill the necessity of beam quality with respect to size, energy spread, etc.
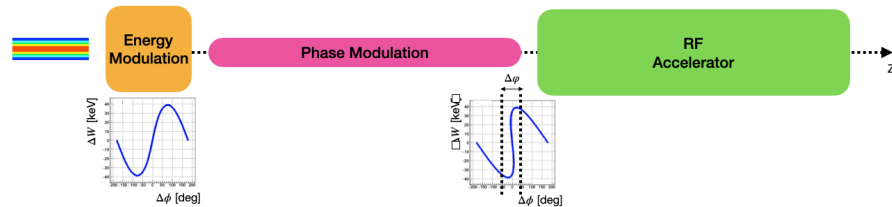
Figure 2.1: Scheme of a buncher forming particle bunches from a DC beam in front of an RF accelerator.

An initial outline of particle accelerators can be described in three fundamental sections; ion source, Low Energy Beam Transport - LEBT, and accelerator units. An ion/particle source is the starting point to generate intended particles by ionizing within a plasma and extraction by a d.c. (static) electric field. Then the LEBT section is defined by several elements such as dipoles for filtering the correct species, quadrupoles (e.g., triplet) and solenoids for beam focusing, or beam diagnostic devices like faraday cups (as a destructive element in the diagnostics). When a d.c.beam is produced and transversely shaped, two alternatives with respect to RF bunch formation can follow in the accelerator line under particular requirements. While a Drift-Tube Linac - DTL, such as an Alvarez-type DTL in Figure 2.2a or an IH-type DTL in Figure 2.2b as one option needs independent bunching and acceleration units, the other, a Radio-Frequency Quadrupole - RFQ, contains bunching, focusing, and accelerating processes all together within one cavity.

The scheme of the front part of the accelerator line mentioned above is composed
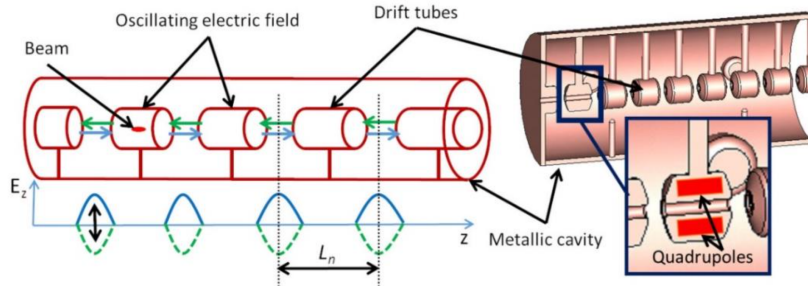
(a) An Alvarez type DTL structure [4].
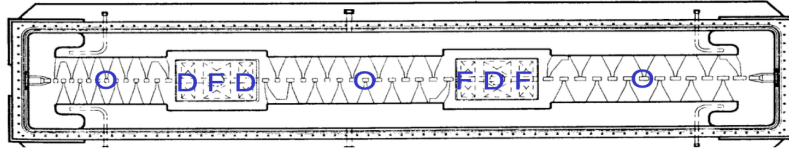
(b) An IH-type DTL structure [9].

Figure 2.2: The variants of DTL structures

of cavities with harmonic voltages for energy modulation and drift sectors for bunch formation and longitudinal focusing, as seen in Figure 2.1, so that a proper combination of both can yield the required beam properties for the subsequent accelerator unit. The design is generally determined according to the input beam distribution. Both options of a DTL or an RFQ begin with a bunching section; since the following RF linac requires a micro-structured beam at the input (bunches with the sequence of the RF frequency of the linac) instead of a continuous one, with a bunch length and energy spread fitting into its input acceptance. While a simple buncher cavity combined with a drift space provides only about 30% of the continuous beam into the DTL acceptance, a modified design concerning an array of buncher cavities can deliver more than 80% of the continuous beam. Since, nowadays, high particle transmission and small longitudinal emittance are demanded high-current linacs, powerful bunching systems are requested.

The proposed concept in this thesis is to design an efficient, compact alternative called "Double Drift Harmonic Buncher - DDHB" for a c.w. beam injection into the next accelerator unit, whose candidates can be a DTL, a simplified RFQ, or a cyclotron. The main elements of a DDHB are two buncher cavities separated with a drift space, L_1, where the first is operated at the fundamental frequency with $-90°$ synchronous phase and applied voltage V_1, and the second buncher cavity at

the second harmonic frequency with $-90°$ synchronous phase and applied voltage V_2, respectively. Finally, a second drift L_2 at the end of the array is needed for a longitudinal beam focus at the DTL entrance. Therefore the properties of this system with respect to the application can be adjusted depending on the four design parameters V_1, L_1, V_2, and L_2.

Nowadays, an RFQ is a typical choice for low and medium energy beams since it provides the three main processes (bunching, focusing, and accelerating), requiring no external focusing within the structure. Although the RFQ can fulfill very high particle transmission into the next unit, the complexity and costs are relatively high. Concerning power consumption, financial perspective, and beam quality, the concept of a DDHB has several benefits, such as flexible output emittances and reduced longitudinal emittance for low and medium current beams. Since the main focus of this research is on the buncher concept, the bunch formation and the multi-harmonic bunching in detail will be discussed in Chapter 4. The potentials/possibilities of the DDHB concept with several demanding designs will be discussed in Chapter 5.

In Chapter 3, an overview of beam dynamics will briefly be reviewed by two topics; longitudinal and transverse beam dynamics. The analytical methods of describing the electromagnetic fields arising from the several components in the accelerator line, such as drift, accelerating gap, and magnetic quadrupole lenses, are needed to understand the behavior of the beam and further investigations on multi-particle tracking. In addition, the interaction of charged particles will be the last topic in this chapter.

A new development of a multi-particle tracking code which is named the "Bunch Creation from a D.C. beam BCDC" has been developed under the study, and its feature will be explained in Chapter 4, as well. The motivation for this development related to the investigation of the DDHB concept is to map all aspects relevant to low-energy beam formation. The program has several specialized features, such as a space charge routine with the influence of the neighboring bunches and an adjustable degree of space charge compensation for each section. The computational performance of the BCDC will also be explained in the scope of the chapter 3 by several comparison methods.

Chapter 3

Linear Ion Acceleration

The goal of an rf linear accelerator is the synchronous acceleration together with a proper focusing of a charged particle beam. An accelerator complex consists of ion sources that produce charged particles, bunchers that get those particles grouped, accelerating units, and various beam diagnostic elements in all these steps. Particular aims like providing high-technological developments in industrial applications or beams of high energy and (good) quality for numerous particle physics experiments/research are fulfilled by RF accelerator structures that will be covered in the first topic of this chapter. One of their most significant types, the so-called Radio-frequency Quadrupole, RFQ, will be explained in the next part in more detail due to being a competitive approach for bunch formation. Analyzing the motion of charged particles in electric and magnetic fields will be the next subject for this chapter. Several fundamental concepts related to beam dynamics, like drift spaces, accelerating gaps, magnetic quadrupole lenses, etc., will be reviewed.

In the second half of this chapter, interactions of particles will be the main topic. Compressing a continuous beam into bunches generates high space charge forces that cause several consequences. The chapter discusses the main aspects, including numerical methods needed for multi-particle simulations.

3.1 Linear Accelerator Structures

The beam formation and acceleration are provided by alternating RF fields generated in a resonant cavity. All approaches have in common that the RF fields are shielded against the beam as long as the field direction is decelerating. Historically, the first type of RF accelerator was the Widerøe-type which is particularly used for low- and medium- energy ion beams. In the Widerøe-type DTL the drift tubes are connected to the conductors of a two-wire transmission line, which is fed by an rf signal. Concerning a match of the accelerating RF voltages with the drift tube positions, synchronization between a reference particle (synchronous particle) and the RF field is needed.
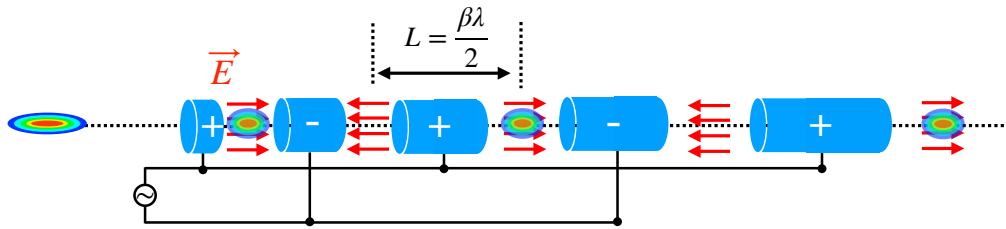
Figure 3.1: Schematic of the Widerøe DTL.

The synchronism in the Widerøe linac is supported by a geometrical relation of drift tubes based on the space between two neighboring gap centers/cells. The distance is given by $L = \beta\lambda/2$ where $\beta = \nu/c$ is the particle velocity w.r.t. the speed of light, c, and λ is the wavelength of operating frequency in voltage/power unit. The RF field was historically generated by various techniques, like two-wire lines (see Figure 3.1), quarter-wave resonators (coaxial type), etc. H-type linacs, mentioned later, are also of the $\beta\lambda/2$-type, but the resonant mode is provided by an rf standing wave in a resonator (seen in Figure 3.4). Designing this linac-type is advantageous at low and medium operating frequencies (up to around 500 MHz). One main limitation of $\beta\lambda/2$-structures is the reduced acceleration efficiency at larger beam velocities, $\beta \geq 0.5$.

In addition to the idea, which uses these alternating fields with opposing polarity between adjacent drift tubes, L. Alvarez proposed an alternative concept based on E-mode acceleration. These resonant cavities provide a particular electromagnetic configuration for efficient particle acceleration (up to $\beta \simeq 0.6$). It is worth noting

that the fundamental resonant mode of a pillbox cavity is the electric E- or transverse magnetic field TM_{010}-mode that provides the necessary longitudinal electric field for particle acceleration. With this knowledge, the Alvarez linac is based on exciting this mode inside a structure, where drift tubes are inserted into a metallic cylinder defining the frequency by its diameter. Many cavities, equipped with many drift tubes in each, can form a long linac. As a different feature from the Widerøe type, the period length of the Alvarez design is $L = \beta\lambda$, instead of $L = \beta\lambda/2$.

Besides providing longitudinal electric fields for acceleration, radial focusing has to be provided by using quadrupole magnets. These small quadrupole magnets are installed in the drift tubes as seen in Figure 3.2.
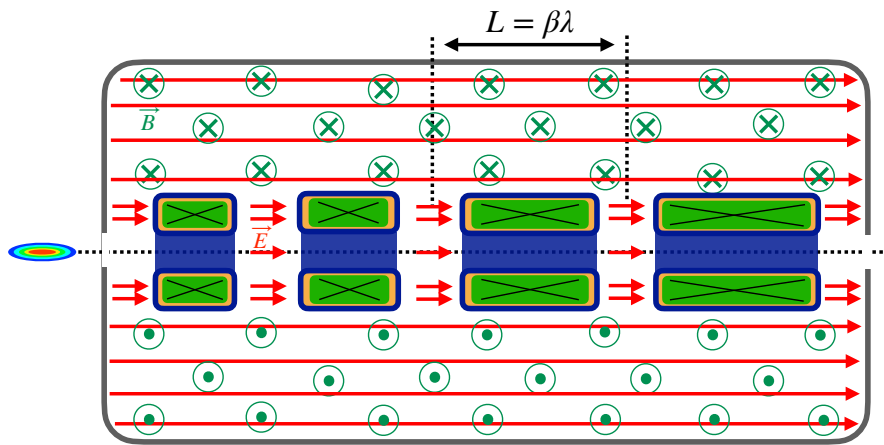
Figure 3.2: Schematic of the Alvarez DTL including electromagnetic field distribution. The green boxes represent magnetic lenses inserted into the drift tubes.Courtesy of H. Hähnel, Dissertation 2017, Frankfurt [10].

The TM_{010}-mode of the Alvarez structure supports the longitudinal electric field along the cavity. The applied voltage on the tank is the integral of the electric field along the beam axis. The electric field in an empty cylinder is constant along the beam axis. With the drift tube insertion, the induced voltage between cavity end walls is divided into gap voltages, $\sum V_{gap} = V_{total}$. On the other hand, H-type structures have dominant transverse electric fields in principle/originally [9]. The fundamental TE_{111}-mode in an empty tank, as seen in Figure 3.3, has a dominant radial electric field, which means the applied voltage is across the cavity diameter. However, with installing the drift tubes, the electromagnetic configuration provides the intended acceleration mode in the longitudinal direction. As seen in Figure 3.4,

the accelerating electric fields are oriented identically at every second gap at a period-length of $\beta\lambda/2$ so that the applied voltage is accelerating the bunches in every gap, when positioned at the entrance correctly.
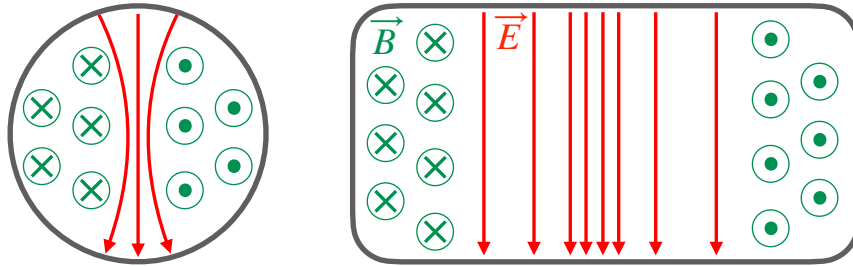
Figure 3.3: The electrodynamic field configuration in the TE_{111}-mode for an empty cavity. Courtesy of H. Hähnel, Dissertation 2017, Frankfurt [10].
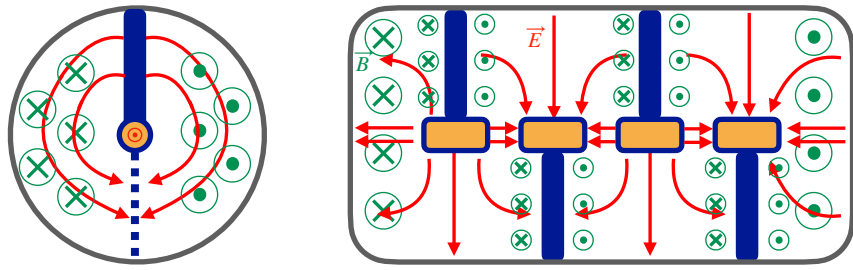
Figure 3.4: The electrodynamic field configuration in the TE_{111}-mode for a drift tube loaded cavity. Courtesy of H. Hähnel, Dissertation 2017, Frankfurt [10].

Assume that an interdigital H-type structure would be designed as seen in Figure 3.4. The adjacent drift tubes are held in opposing directions so that the transverse electric field can produce the longitudinal field configuration for acceleration. Careful drift tube design provides high axial gap field symmetry, though the stems in $\beta\lambda/2$-structures have to be massive, as they carry high RF currents.

3.2 Radio-Frequency Quadrupole Linear Accelerators (RFQs)

In 1970, another kind of linear accelerator scheme was proposed by Kapchinskiy and Tepliakov [11]. The principle is to unify three fundamental processes (bunching, focusing, and accelerating) by an excited RF TE_{210}-quadrupole mode, as shown in Figure 3.7b. With the development of this compact and successful structure, it has become a preferable choice for many linac facilities. Besides being an important concept, it is the alternative option for the proposal in this thesis. Hence the RFQ with its working principle will be described under this new subsection. As a further option, a powerful external buncher system, as proposed in this thesis can be combined with a simplified RFQ, as was already demonstrated successfully by FRIB at MSU [12].

The structure for RFQs consists of four main sections; the radial matching section, the shaper, which adjusts the synchronous phase for bunching the particles, the gentle buncher, and finally the accelerating part. The tasks are fulfilled by the four electrodes inserted into the cavity that provide an electric quadrupole focusing channel, i.e., alternating gradient with the period of the RF. Such an electric quadrupole channel provides so-called strong focusing in the same way as a magnetic quadrupole channel. At low beam energies, electric forces are sufficient. The vane tip geometry has a progressively oscillating structure: Figure 3.5a shows a schematic of the four-vane geometry with the modulated electrode tips. Two electrodes in the same plane are identically machined. The second electrode pair aperture minimum is shifted by $\beta\lambda/2$ against the first pair. While the minimum distance of vane tips is called the aperture a, the maximum is represented by ma with the modulation factor m. The length for a unit cell is $\beta\lambda/2$. The modulation of the electrodes leads to an electric field component in longitudinal (i.e. in beam propagation) direction, which is needed for the beam acceleration.

Since the particle velocity is relatively low and the magnetic fields are oriented along the beam axis, the only forces acting inside the aperture are the electric forces. The electric field arising from the electrodes can be derived from a scalar potential where the Laplace Equation is satisfied. Assume that a time-dependent
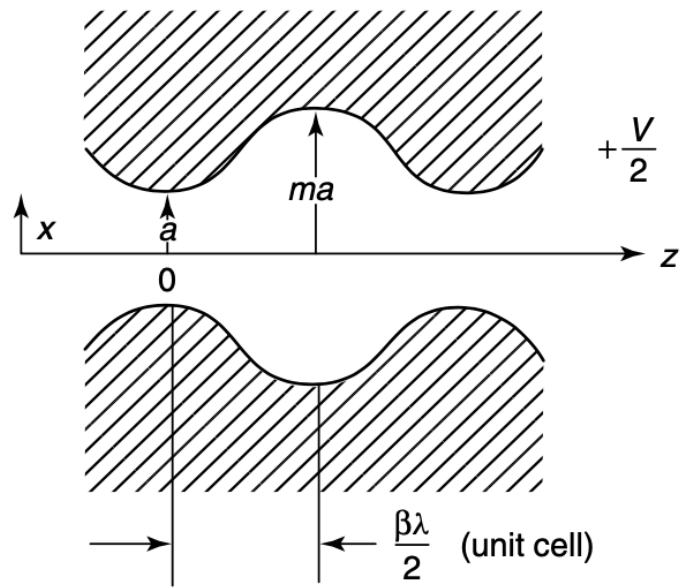
(a) The layout of a four-vane geometry.
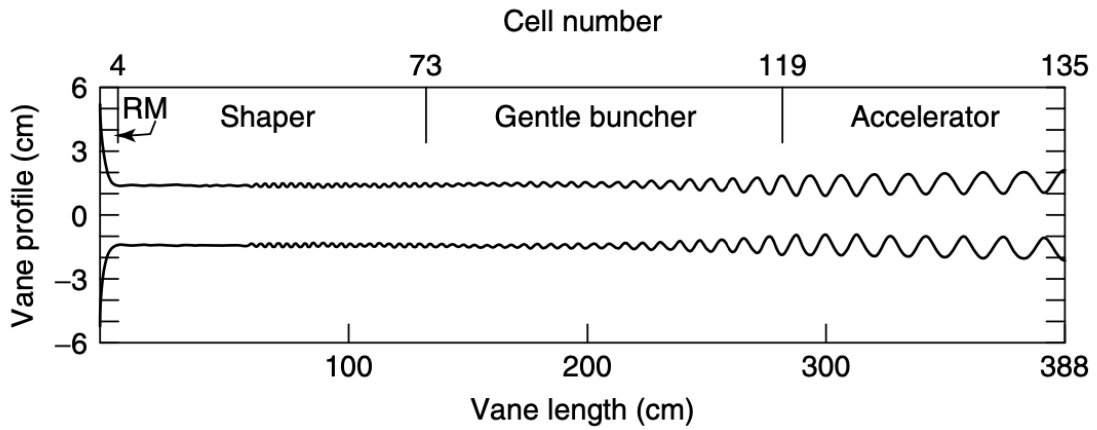
(b) An RFQ schematic of the pole tips with adiabatic bunching.

Figure 3.5: The schematics of an RFQ vane structures [13].

scalar potential U() is given in cylindrical coordinates as :

$$U(r,\theta,z,t) = V(r,\theta,z) \cdot \sin(\omega t + \phi) \quad, \tag{3.1}$$

where $\omega = 2\pi f$ is the RF frequency, ϕ is the initial potential phase, and $V(r,\theta,z)$ is

one solution of the Laplace Equation, given by:

$$\frac{\partial^2 V}{\partial r^2} = \frac{1}{r}\frac{\partial V}{\partial r} + \frac{1}{r^2}\frac{\partial^2 V}{\partial \theta^2} + \frac{\partial^2 V}{\partial z^2} = 0 \quad . \tag{3.2}$$

With the method of separation of variables, the general solution of Equation 3.2 is obtained:

$$V(r,\theta,z) = \frac{V}{2}\Big[\sum_n A_{0n} r_{2n} \cos(2n\theta) + \sum_n \sum_m A_{mn} I_{2n}(mkr) \cos(2n\theta) \cos(mkz) \Big] , \tag{3.3}$$

where V is the voltage between the vanes, I_{2n} is the $2n^{th}$ order of the Bessel function, and $k = \frac{2\pi}{\beta\lambda}$ is the wave number. Although this solution contains all harmonics in an infinite series, the lowest two terms can be mathematically adequate to describe the RFQ electrode potential, according to Kapchinskiy and Tepliyakov, where the name of "K-T potential function" is originated. The K-T potential function can be written as :

$$V(r,\theta,z) = A_{01} r^2 \cos(2\theta) + A_{10} I_0(kr) \cos(kz) \quad , \tag{3.4}$$

where its first part describes the transverse quadrupole term and the second term defines the longitudinal focusing and the acceleration. Applying a voltage of $V/2$ between two adjacent vanes, the terms of focusing A_{01} and of acceleration A_{10} are obtained :

$$A_{01} = \frac{m^2 - 1}{m^2 I_0(ka) + I_0(mka)} \quad , \tag{3.5}$$

$$A_{10} = \frac{1}{a^2}\frac{I_0(ka) + I_0(mka)}{m^2 I_0(ka) + I_0(mka)} \quad . \tag{3.6}$$

Besides these critical geometrical dependencies, space charge forces, especially for high-intensity beams become significant in beam dynamics. Hence, the acceleration should start simultaneously with bunching to reduce the RF defocusing space charge forces from the beginning. The synchronous phase ϕ_s starts from -90 deg and rises first slightly and then with increasing increments until the chosen synchronous phase

for the accelerating criterion is reached (see Figure 3.6).
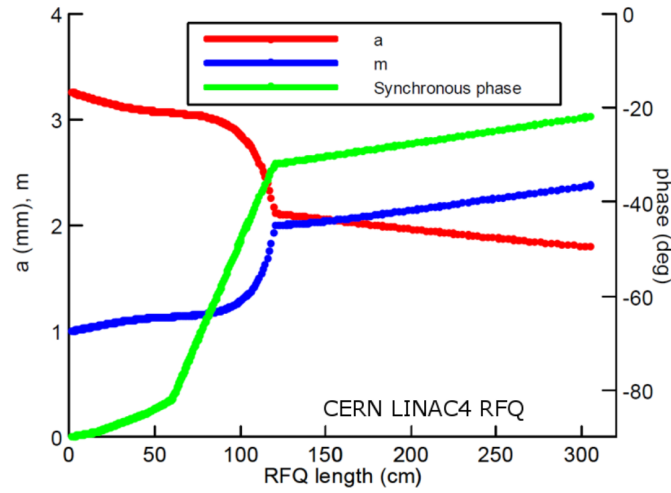
Figure 3.6: Beam dynamics design of the RFQ at CERN, LINAC4 [14].

The operated TE_{210}-mode has to be separated properly from the TE_{110}-mode. This is an issue in four-vane RFQs, while the four-rod RFQ alternative does not show that problem [15].

(a) TE110.   (b) TE210.
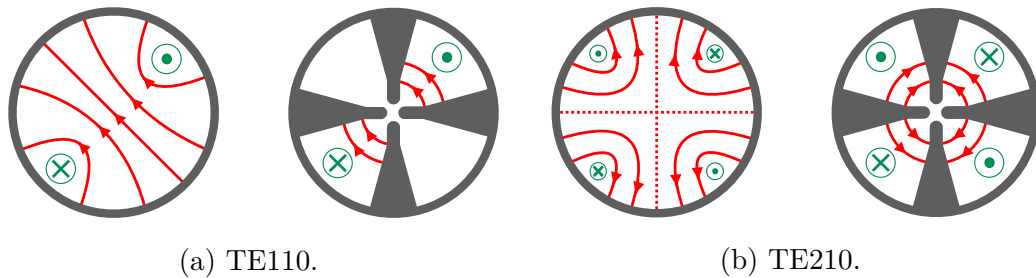
Figure 3.7: The electromagnetic configurations for TE_{110} and TE_{210} in an empty and four-vane loaded cavities [13].

3.3 Longitudinal Beam Dynamics

3.3.1 Single Gap Transformation

An e.m. field is generated in an R.F. cavity with a particular resonant mode. The mode is excited by an R.F. generator at the resonant frequency f_{rf}, which determines the characteristic configuration of that mode and defines the accelerating field, E_z. Regarding this, by using the energy-momentum relation, $\mathcal{E}^2 = \mathcal{E}_0^2 + p^2 c^2$, where $\mathcal{E}$ is the total energy, $\mathcal{E}_0 = m_0 c^2$ is the particle rest energy, m_0 is the rest mass, $p = m\nu$ is the particle momentum, m is the relativistic mass and ν is the particle velocity) and the Lorentz force, the electric field in an accelerating gap can be derived as:

$$\mathcal{E}^2 = \mathcal{E}_0^2 + p^2 c^2 \quad \rightarrow \quad 2\mathcal{E} \; d\mathcal{E} = 2p \; dp \; c^2 \quad ,$$

$$\rightarrow \quad d\mathcal{E} = \frac{m\nu \; c^2}{\mathcal{E}} dp \quad ,$$

$$\rightarrow \quad d\mathcal{E} = \nu \cdot dp \quad ,$$

$$\text{and} \quad \frac{dp}{dt} = q \cdot E_z \quad \rightarrow \quad \frac{dp}{\frac{dz}{\nu}} = q \cdot E_z \quad ,$$

$$\rightarrow \quad \nu \frac{dp}{dz} = q \cdot E_z \quad ,$$

$$\text{hence} \quad \frac{dW}{dz} = q \cdot E_z \quad \Leftrightarrow \quad \frac{dW}{dz} = q \cdot E_z \quad , \tag{3.7}$$

where $W = \mathcal{E} - \mathcal{E}_0$ is the kinetic energy and q is the charge of the particle. The integration of this equation over the accelerating gap, the energy gain per electrode ΔW can be obtained :

$$\Delta W \;\; = \;\; \int_{gap} \frac{dW}{dz} dz = \int_{gap} q \cdot E_z dz \quad . \tag{3.8}$$

The electric field in the gap can be described as a function of time:

$$E_z(z,t) = E_0(z) \cdot \cos(\omega t) \quad , \tag{3.9}$$

where $E_0(z)$ is the field amplitude in the gap within a specific/periodic time and $\omega = 2\pi f_{rf}$ is the angular frequency . After inserting $E_z(z,t)$ into Equation 3.8, the

ΔW can be rewritten as:

$$
\begin{aligned}
\Delta W = \;\; &= \;\; q \int_{gap} E_z(z,t) dz \quad , \\
&= \;\; q \int_{-\frac{L}{2}}^{+\frac{L}{2}} E_0(z) \cdot \cos(\omega t) dz \quad , \\
&= \;\; q \int_{-\frac{L}{2}}^{+\frac{L}{2}} E_0(z) \cdot \cos\left(\omega \frac{z}{\nu} + \phi_s\right) dz \quad , \\
&= \;\; q \int_{-\frac{L}{2}}^{+\frac{L}{2}} E_0(z) \cdot \cos\left(kz + \phi_s\right) dz \quad , \tag{3.10}
\end{aligned}
$$

where $k = \frac{\omega}{\nu}$ is the wave number, and ϕ_s is the synchronous particle phase at the gap. By using the trigonometric identity of $\cos(A + B) = \cos A \cdot \cos B - \sin A \cdot \sin B$, the above equation can be simplified as:

$$
\begin{aligned}
\Delta W \;\; &= \;\; q \int_{gap} E_0(z) \cdot \cos\left(kz\right) \cdot \cos\phi_s dz \quad , \tag{3.11} \\
&= \;\; q \int_{gap} E_0(z) dz \cdot \frac{\int_{gap} E_0(z) \cos\left(kz\right) dz}{\int_{gap} E_0(z) dz} \cdot \cos\phi_s \quad , \tag{3.12} \\
&= \;\; q \cdot V_0 \cdot T \cdot \cos\phi_s \quad , \tag{3.13}
\end{aligned}
$$

where $V_0 = \int E_0(z) dz$ is the maximum voltage given by the cavity, and the transit time factor, denoted as $T = \frac{\int_{gap} E_0(z) \cos\left(kz\right) dz}{\int_{gap} E_0(z) dz}$, is defined as the fraction of energy gain in an RF field compared to the maximum energy gain in a time-invariant field [13]. In a linac structure, a condition for synchronism is defined for a reference particle (the synchronous particle), which crosses the gap center with the synchronous particle phase ϕ_s with respect to the accelerating voltage. For the ith gap number, the effective gap voltage is $V_{eff,i} = V_{0,i} \cdot T_i$ and the effective energy gain of the synchronous particle is $\Delta W_{s,i} = q \cdot V_{0,i} \cdot T_i \cdot \cos\phi_{s,i}$. Since the synchronism permits the synchronous particle to go into the subsequent gap cap with the same phase ϕ_s with respect to the accelerating voltage $V_{eff,c} = \sum_i V_{0,i} \cdot T_i$, where c represents the cavity, one can describe the total energy gain as:

$$
\Delta W = q \cdot V_{eff,c} \cos(\phi_s) \quad . \tag{3.14}
$$

3.3.2 Longitudinal Beam Dynamics For Multi-Gap Structures

As described at the beginning of this chapter, a conventional linac is composed of many accelerating gaps separated by drift tubes. The synchronism between the beam and the accelerating field is maintained by a certain distance between the accelerating gaps in accordance with the formalism as $L_n = \beta_n \lambda_{rf}$, where L_n stands for the period length (distance between gap centers) of the RF-wave at the n$^{\text{th}}$ cell, β_n is the velocity of the synchronous particle at that cell and λ_{rf} is the wavelength of the RF-voltage. As a remark, the index s always denotes the synchronous particle which crosses the gap center at the synchronous phase ϕ_s with respect to the RF-wave maximum. which runs through each gap center with constant synchronous phase ϕ_s [13].

Consider that the motion of particles with phases and energies deviates from the synchronous particle since the synchronous particle travels at each gap center with the coherent phase. When the particles pass through the drift tubes, they do not experience any force. The change/evolution of the synchronous particle phase from one cell to the next is described by Equation 3.15:

$$\phi_n = \phi_{n-1} + \omega \frac{L_{n-1}}{\beta_{n-1} c} + \begin{cases} \pi, & \text{for } \beta\lambda/2\text{-structure} \\ 0, & \text{for } \beta\lambda\text{-structure} \end{cases}, \qquad (3.15)$$

where the cell length is given as:

$$L_{n-1} = N \cdot \beta_{s,n-1} \cdot \lambda \quad \text{with} \quad N = \begin{cases} 1/2, & \text{for } \beta\lambda/2\text{-structure} \\ 1, & \text{for } \beta\lambda\text{-structure} \end{cases}. \qquad (3.16)$$

One can rewrite the period length from the center of one drift tube to the center of the next as $L_n = N(\beta_{s,n-1} + \beta_{s,n})\lambda/2$. Hence the change in phase position for an arbitrary particle i relative to the synchronous particle can be given as:

$$\Delta(\phi - \phi_s)_n = \Delta\phi_n - \Delta\phi_{s,n} = 2\pi\beta_{s,n-1}\left(\frac{1}{\beta_{n-1}} - \frac{1}{\beta_{s,n-1}}\right) \quad . \qquad (3.17)$$

According to the Taylor expansion, one can write the velocity relation as:

$$\frac{1}{\beta_{n-1}} - \frac{1}{\beta_{s,n-1}} = \frac{1}{\beta_s + \delta\beta} - \frac{1}{\beta_s} \approx -\frac{\delta\beta}{\beta_s^2} \quad , \tag{3.18}$$

where $\delta\beta = \frac{\delta W}{mc^2 \gamma_s^3 \beta_s}$ and $\delta\beta << 1$; hence, the equation of phase relation becomes:

$$\Delta(\phi - \phi_s)_n = -2\pi N \frac{W_{n-1} - W_{s,n-1}}{mc^2 \gamma_{s,n-1}^3 \beta_{s,n-1}^2} \quad , \tag{3.19}$$

with the energy change of a particle along L_n with respect to the synchronous particle :

$$\Delta(W - W_s)_n = \Delta W_n - \Delta W_{s,n} = qE_0 T L_n (\cos\phi_n - \cos\phi_{s,n}) \quad . \tag{3.20}$$

This is a system of coupled differential equations where these equations convert to continuous variables along the beam axis $n = \frac{s}{N\beta_s\lambda}$ as:

$$\Delta(\phi - \phi_s)_n \quad \rightarrow \quad \frac{d(\phi - \phi_s)}{dn} \quad \text{and} \tag{3.21}$$

$$\Delta(W - W_s)_n \quad \rightarrow \quad \frac{d(W - W_s)}{dn} \quad . \tag{3.22}$$

Then equations 3.19 and 3.20 become:

$$\gamma_s^3 \beta_s^3 \frac{d(\phi - \phi_s)}{ds} \quad = \quad -2\pi \frac{(W - W_s)}{mc^2\lambda} \quad , \tag{3.23}$$

$$\frac{d(W - W_s)}{ds} \quad = \quad qE_0 T (\cos\phi - \cos\phi_s) \quad . \tag{3.24}$$

When Equation 3.23 is differentiated by the axial distance s and Equation 3.24 is inserted into the differentiated equation, a second-order differential equation for the

longitudinal motion is obtained as:

$$
\begin{aligned}
\frac{d}{ds}\left[\gamma_s^3\beta_s^3\frac{d(\phi-\phi_s)}{ds}\right] &= -2\pi\frac{qE_0T}{mc^2\lambda}(\cos\phi-\cos\phi_s) \quad, \\
\gamma_s^3\beta_s^3\frac{d^2(\phi-\phi_s)}{ds^2} &+ 3\gamma_s^2\beta_s^2\left[\frac{d}{ds}(\gamma_s\beta_s)\right]\left[\frac{d(\phi-\phi_s)}{ds}\right] \\
&+ 2\pi\frac{qE_0T}{mc^2\lambda}(\cos\phi-\cos\phi_s) = 0 \quad.
\end{aligned}
\tag{3.25}
$$

In order to obtain the stable energy-phase area called "separatrix", the solution of Equation 3.26 is approximated as slow acceleration where $\beta_s\gamma_s$, E_0T, and ϕ_S are kept constant.

$$
\frac{d^2(\phi-\phi_s)}{ds^2} + 2\pi\frac{qE_0T}{mc^2\gamma_s^3\beta_s^3\lambda}(\cos\phi-\cos\phi_s) = 0 \quad.
\tag{3.26}
$$

Since the equation represents the total energy oscillation (it is also known as the Hamiltonian equation represents H), a simplified notation can be given as [16]:

$$
\frac{d}{ds}\left[\frac{1}{2}\left(\frac{d\Delta\phi}{ds}\right) + U(\Delta\phi)\right] = 0 \quad,
\tag{3.27}
$$

where $\Delta\phi = \phi - \phi_s$ and the indicated term within the bracket represents the total energy oscillation. Hence two points can be found for the potential function of $U(\Delta\phi)$, where $\frac{dU}{d\Delta\phi} = 0$; a minimum that is the stable point for $\Delta\phi = 0$ is the first one, and the second one is a maximum that is the unstable point for $\Delta\phi = -2\phi_s$. These limits are called fixed points where the velocity in the phase plane is zero. Concerning the fixed points, one can define the separatrix in the phase-energy plane with the division of stable and unstable regions with respect to the energy change ΔW :

$$
\frac{\omega}{2mc^3\beta_s^3\gamma_s^3}(\Delta W)^2 + qE_0T[\sin(\phi_s+\Delta\phi)+\sin\phi_s-(2\phi_s+\Delta\phi)\cos\phi_s] = 0 \quad,
\tag{3.28}
$$

where the separatrix is in range of $[\Delta\phi \cong -2\phi_s \ , \ \Delta\phi = +\ \phi_s]$, the span of $3|\phi_s|$. With the help of this expression, the boundary of minimum and maximum energy

change can be found for $\Delta\phi = 0$:

$$\Delta W = \pm\sqrt{\left[\frac{qmc^3\beta_s^3\gamma_s^3 E_0 T(\phi_s\cos\phi_s - \sin\phi_s)}{\omega}\right]} \quad . \tag{3.29}$$
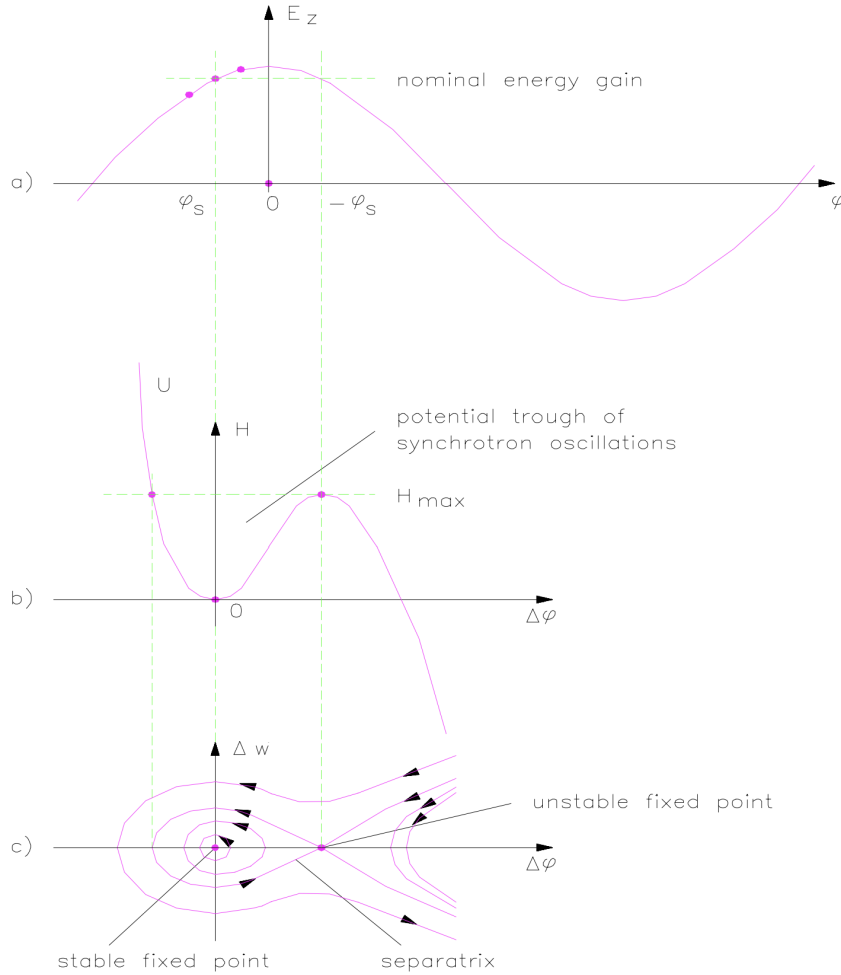
Figure 3.8: a. electric field in z-direction in an rf-gap, b. potential well of the energy-phase oscillation, c. particle trajectories in the energy-phase plane with the separatrix, stable and unstable regions [16].

3.3.3 Phase Stability In A Linac

Consider a negative synchronous phase, $-\phi_s$, as shown in Figure 3.9, is applied the cavity. If particles nearby the reference particle enter the gap later than the synchronous particle, they experience a higher voltage for reaching the synchronous particle by gaining slightly more energy. Correspondingly if particles nearby the reference particle enter the gap earlier than the synchronous particle, they experience a lower voltage for slowing down. This mechanism called the "Phase Stability Principle" provides longitudinal phase focusing.
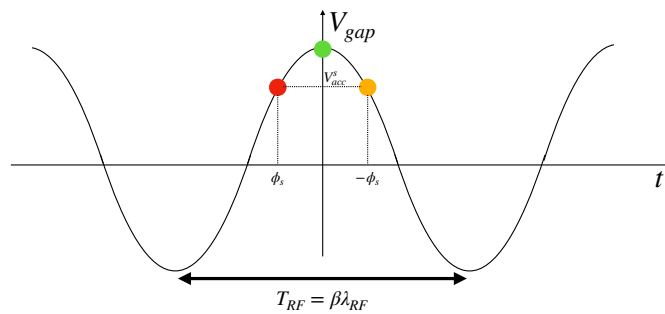
Figure 3.9: Schematic of phase stability.

3.3.4 Single Particle Tracking Formalism for the BCDC Code

In conclusion, the energy-phase relations for several elements are significant for the numeric applications mentioned in Chapter 5. The $\Delta W, \Delta \phi$ transformation in the longitudinal plane for accelerating gap, using the thin gap approximation, can be given as:

$$\Delta W_i^{out} = \Delta W_i^{in} + q \cdot V_{eff} \cdot \left(\cos \phi_i - \cos \phi_s \right) \quad , \tag{3.30}$$

$$\Delta \phi_i^{out} = \Delta \phi_i^{in} \quad , \tag{3.31}$$

where i represents an arbitrary particle. The relation of the drift s pace, the $\Delta W, \Delta \phi$ equations can be written as :

$$\Delta W_i^{out} = \Delta W_i^{in} \quad , \tag{3.32}$$

$$\Delta \phi_i^{out} = \Delta \phi_i^{in} - \Delta W_0^{in} \cdot \frac{1}{A \cdot m_0 \cdot c^2 \cdot \gamma_s^3 \beta_s^3} \cdot \frac{l}{\lambda} \cdot 2\pi \quad , \tag{3.33}$$

where A is the atomic number, m_0 is the mass of the particle, l is the distance, and 2π is for the unit consistency in terms of degree unit.

3.4 Transversal Beam Dynamics

3.4.1 RF Defocusing Effect

Due to the radial component of the rf field in an accelerating gap, the off-axis particles experience a radial force. Since the high-frequency electromagnetic field is concentrated in a relatively small region, the radial component of the electric field becomes inevitable, as can be seen in Figure 3.10. With Maxwell's equations
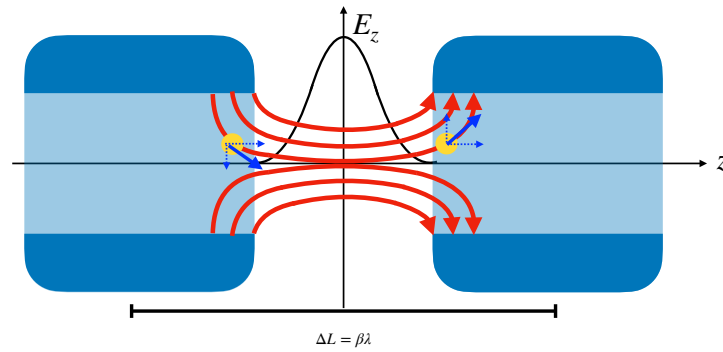
Figure 3.10: The electric field inside an RF accelerating gap.

in vacuum, the transverse forces in cylindrical coordinates, E_r and B_θ, can be obtained. The solution of the electric field (near the axis) in cylindrical coordinates E_r, Equation 3.38, can be solved from Gauss's Law, in Equation 3.35:

$$\nabla \cdot \vec{E} = \frac{\rho}{\epsilon_0} = 0 \quad (\rho = 0) \quad \rightarrow \quad \frac{1}{r}\frac{d(rE_r)}{dr} + \frac{dE_z}{dz} = 0 \tag{3.34}$$

$$\rightarrow \quad \frac{d}{dr}\Big(rE_r\Big) = -r \cdot \frac{dE_z}{dz} \quad . \tag{3.35}$$

For the radial field component $E_R(R,z)$ at the radius R, integration over the radius results in:

$$R \cdot E_r = \int_0^R -r \frac{dE_z}{dz} dr \quad .$$

(3.36)

When E_r is in the region near the axis, where E_z is approximately independent of radius r, the simplified E_r equation can be obtained:

$$E_r = -\frac{dE_z}{dz} \frac{r}{2} \quad .$$

(3.37)

On the other hand, one can divide the radius into small pieces $0, r_i, r_{i+1}, ..., r_{N_{gap}}$ as fixed radii. Then the longitudinal electric field E_z can be computed at each small fixed radius, and the radial electric field E_r become the summation of those fields:

$$E_r = -\frac{1}{2R} \cdot \sum_i^{N_{gap}} \left(\frac{dE_z}{dz}\right)_i \cdot (r_i^2 - r_{i-1}^2) \quad .$$

(3.38)

It is noting that In the rest of the part, Equation 3.37 is used to explain the concept of RF-defocusing. Hence to obtain the magnetic field solution, one should combine Equation 3.37 with Ampere's Law. When Equation 3.37 is inserted into Ampere's Law, the solution of the magnetic field B_θ, Equation 3.40, can be found as:

$$\nabla \times \vec{B} = \frac{1}{c^2} \frac{d\vec{E}}{dt} \quad \rightarrow \quad -\frac{\partial B_\theta}{\partial z} = \frac{1}{c^2} \frac{\partial E_r}{\partial t} \quad .$$

(3.39)

Taking derivative of E_r solution to insert into Equation 3.39, one can get the magnetic field solution:

$$\int -\frac{\partial B_\theta}{\partial z} = \int -\frac{r}{c^2} \frac{\partial^2 E_z}{\partial t \partial z} \quad \rightarrow \quad B_\theta = \frac{r}{2c^2} \frac{dE_z}{dt} \quad .$$

(3.40)

From the Lorentz force ($\vec{F} = q \cdot \vec{E} + q \cdot \vec{\nu} \times \vec{B}$), one can obtain two terms from the contributing electric and magnetic fields :

$$
\begin{aligned}
F_r &= q\Big(E_r - \nu B_\theta\Big) \quad , \\
F_r &= q\Big(-\frac{r}{2}\frac{dE_z}{dz} - \frac{r \cdot \beta c}{2c^2}\frac{dE_z}{dt}\Big) \quad , \\
F_r &= -\frac{q}{2}\cdot r\Big[\frac{dE_z}{dz} + \frac{\beta}{c}\frac{dE_z}{dt}\Big] \quad ,
\end{aligned}
$$

(3.41)

(3.42)

Assume that the velocity change along the gap is small. The radial impulse on particle at radius r can be obtained as:

$$
\begin{aligned}
\Delta p_r &= -\frac{q}{2}\int_{-\frac{L}{2}}^{+\frac{L}{2}} r\Big[\frac{dE_z}{dz} + \frac{\beta}{c}\frac{dE_z}{dt}\Big]\frac{dz}{\beta c} \quad , \\
&= -\frac{qr}{2\beta c}\int_{-\frac{L}{2}}^{+\frac{L}{2}}\Big[\frac{dE_z}{dz} - \big(\frac{1}{\beta c} - \frac{\beta}{c}\big)\frac{dE_z}{dt}\Big]dz \quad , \\
&= -\frac{qr\omega}{2\gamma^2\beta^2 c^2}\int_{-\frac{L}{2}}^{+\frac{L}{2}} E_z(z)\sin(\omega t + \phi)dz \quad .
\end{aligned}
$$

(3.43)

Using the relation of $p = m \cdot c \cdot \gamma\beta \cdot r'$ with $r' = \frac{dr}{dz}$, the impulse equation with an approximation can be obtained in Equation 3.44 and the position relation can be expressed in Equation 3.45:

$$
\begin{aligned}
\Delta(\gamma\beta r') &= -\frac{\pi\, qE_0\, T\sin(\phi)\, L}{m\, c^2\, \gamma^2\beta^2\lambda}\cdot r \quad , \\
\frac{\Delta r'}{r} &= -\frac{1}{\gamma\beta}\cdot\frac{\pi\, q\, V_{eff}\sin(\phi)}{m\, c^2\, \gamma^2\beta^2\lambda} \quad ,
\end{aligned}
$$

(3.44)

(3.45)

where the effective voltage per RF period is defined as $V_{eff} = E_0 \cdot T \cdot L$. If these positions are defined as $\Delta(\Delta X_i') = \Delta X_{1,i}' - \Delta X_{0,i}'$ and $\Delta(\Delta Y_i') = \Delta Y_{1,i}' - \Delta Y_{0,i}'$, as a result of the position relation 3.45, the two transverse planes for the defocusing RF gap at a negative synchronous phase can be written as:

$$
\begin{aligned}
\Delta X_{1,i}' &= \Delta X_{0,i}' - \frac{\pi q V_{eff}\cdot\sin(\phi_s)}{m\gamma^3\beta^3 c^2\lambda}\cdot X_{0,i} \quad , \\
\Delta Y_{1,i}' &= \Delta Y_{0,i}' - \frac{\pi q V_{eff}\cdot\sin(\phi_s)}{m\gamma^3\beta^3 c^2\lambda}\cdot Y_{0,i} \quad .
\end{aligned}
$$

(3.46)

(3.47)

3.4.2 Quadrupole magnetic focusing and field-free space

The transverse RF defocusing effects are usually eliminated by the use of magnetic quadrupole lenses, which are installed within drift tubes in DTLs. Figure 3.11 shows a cross-section of a quadrupole magnet with its magnetic field pattern. Assume that a particle moves along the beam axis with the velocity ν and the charge q. The forces acting on the particle can be written as $F_x = -q \cdot \nu \cdot B_y = -q \cdot \nu \cdot G \cdot x$ and $F_y = q \cdot \nu \cdot B_x = q \cdot \nu \cdot G \cdot y$ where $G = \frac{\partial B_x}{\partial y} = \frac{\partial B_y}{\partial x}$ is the constant transverse quadrupole gradient. For the particle, one can write the equations of motion :

$$
\begin{aligned}
\frac{d^2x}{ds^2} + \kappa^2(s)x &= 0 \quad, \\
\frac{d^2y}{ds^2} - \kappa^2(s)y &= 0 \quad,
\end{aligned}
\tag{3.48}
$$

where $\kappa^2(s) = \frac{|qG(s)|}{mc\gamma\beta}$ with the axial position s. It is worth noting that the quadrupole forces act strongly on the low-momentum particles while bending to the high-momentum ones is much harder.
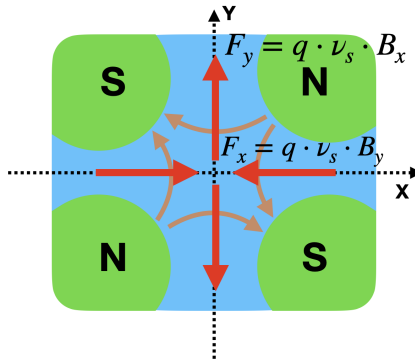
Figure 3.11: The magnetic field pattern for a quadrupole, focusing in x-direction.

A typical optical lattice for quadrupole magnets in a beam transport line is a combination of quadrupoles in opposite/changing polarities instead of using an individual quadrupole lens due to focusing in only one plane. The set of quadrupoles brings the concept of strong focusing. Since the restoring force is a linear function of displacement, e.g. $F_x = -q \cdot \nu \cdot G \cdot x$, the total effect of a dublet or a triplet lens is always focusing [6]. The most common lattice configurations are $FODO$, $FOFODODO$, FDO, or $FDF - A - DFD$, where F is denoted by focusing, D is

denoted by defocusing, O is for drift space between two lenses and A stands for rf acceleration. While the $FODO$ lattice is composed of a set of subsequent singlet magnets, the $FDF - A - DFD$ consists of two focusing triplets preferably used for H-type linacs.

The second-order differential equations 3.48 called "Hill's Equation" are linear function based on a restoring force. A matrix solution is a more convenient method for studying the properties of Hill's equation. The matrix representations of solutions for such a second-order differential equation can be given:

$$
\begin{bmatrix} x_1 \\ x_1' \end{bmatrix} = \begin{bmatrix} a & b \\ c & d \end{bmatrix} \begin{bmatrix} x_0 \\ x_0' \end{bmatrix} \quad , \tag{3.49}
$$

where $x' = dx/ds$ and $x'' = d^2x/ds^2$. The 2x2 matrix R in this representation is called a transfer matrix, and its coefficients (a,b,c,d) are the variables for the effects of the element. Since an accelerator line consists of a set of elements, the total transfer matrix can be calculated as the product of each R-matrices. If the order of the elements is like $1,2,3,\cdots,n$, then the total transfer matrix should be $R_t = R_n \cdot [....] \cdot R_3 \cdot R_2 \cdot R_1$.

In a linac design, three transfer matrices are essential to describe quadrupole lenses. The transfer matrix of a focusing quadrupole singlet can be defined as:

$$
R = \begin{bmatrix} \cos(\sqrt{K} \cdot L_m) & \frac{1}{\sqrt{K}} \sin(\sqrt{K} \cdot L_m) \\ -\sqrt{K} \sin(\sqrt{K} \cdot L_m) & \cos(\sqrt{K} \cdot L_m) \end{bmatrix} \quad , \tag{3.50}
$$

where L_m is the singlet length, and $K = \kappa^2 = \frac{qG}{mc\beta\gamma}$ is the strength of the magnet. The strength K must always be greater than zero for the focusing effect. On the other hand, the defocusing transfer matrix is given :

$$
R = \begin{bmatrix} \cosh(\sqrt{|K|} \cdot L_m) & \frac{1}{\sqrt{|K|}} \sinh(\sqrt{|K|} \cdot L_m) \\ -\sqrt{|K|} \sinh(\sqrt{|K|} \cdot L_m) & \cosh(\sqrt{|K|} \cdot L_m) \end{bmatrix} \quad . \tag{3.51}
$$

Besides quadrupole magnets, a transfer matrix for a field-free region is also important:

$$R = \begin{bmatrix} 1 & L_d \\ 0 & 1 \end{bmatrix} \quad , \tag{3.52}$$

where L_d is the drift length.

In conclusion, the equations of motion for the three essential routines can be indicated in the following equations. The formulas for focusing quadrupole in x-direction can be written as:

$$X_{1,i} = X_{0,i} \cdot \cos(\sqrt{K_i} \cdot L_m) + X'_{0,i} \cdot \frac{1}{\sqrt{K_i}} \sin(\sqrt{K_i} \cdot L_m) \quad , \tag{3.53}$$

$$X'_{1,i} = X_{0,i} \cdot \left(-\sqrt{K_i} \sin(\sqrt{K_i} \cdot L_m) \right) + X'_{0,i} \cdot \cos(\sqrt{K_i} \cdot L_m) \quad , \tag{3.54}$$

where $K_i = \frac{q \cdot B'}{\gamma \ A \ m_0 \beta_i \ c} = \frac{q \cdot B}{\gamma \ A \ m_0 \beta_i \ c \ a}$ is the focusing strength for an arbitrary particle i, $B' = \frac{B}{a}$ is the strength of the magnetic field, and a is the aperture of the pole. On the other hand, the equation of motion for defocusing plane can be given as:

$$Y_{1,i} = Y_{0,i} \cdot \cosh(\sqrt{K_i} \cdot L_m) + Y'_{0,i} \cdot \frac{1}{\sqrt{K_i}} \sinh(\sqrt{K_i} \cdot L_m) \tag{3.55}$$

$$Y'_{1,i} = Y_{0,i} \cdot \left(\sqrt{K_i} \sinh(\sqrt{K_i} \cdot L_m) \right) + Y'_{0,i} \cdot \cosh(\sqrt{K_i} \cdot L_m) \tag{3.56}$$

In addition, the formulas in a field-free region, using a geometrical relation, can be defined as:

$$X'_0 = \frac{dx}{dz} \quad \rightarrow \quad dx = X'_0 \cdot L_d \quad , \tag{3.57}$$

where $dx = X_1 - X_0$ and $dz = L_d$. Hence the equations for drift transformation in the x-direction become:

$$X'_{1,i} = X'_{0,i} \quad , \tag{3.58}$$

$$X_{1,i} = X_{0,i} + X'_{0,i} \cdot L_d \quad . \tag{3.59}$$

3.5 Space Charge

In particle accelerators, in addition to the external fields (e.g., the electric field of an accelerating gap or the magnetic field of a lens), a charged particle distribution generates electric forces called 'space charge' forces. The beam, especially in low-energy regions, like ion source extractions or the LEBT line, produces (unavoidable self-consistent) fields by which the longitudinal-transversal beam stability can be affected. Each particle experiences a repulsion force by the others due to the Coulomb force; hence, the space charge force causes momentum changes in the distribution. Since the effects of space charge on beam dynamics are manifold, the consequence of self-interactions will be the subject of the investigations within the scope of the work in this thesis. Charged particles are always accompanied by their self-electric field
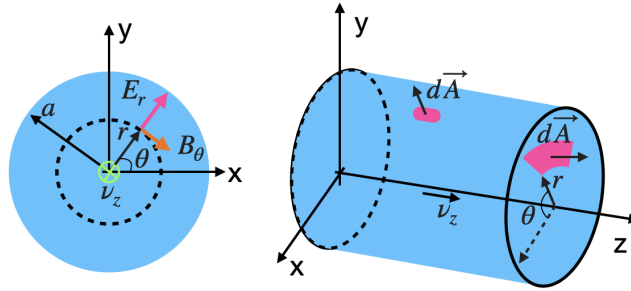
Figure 3.12: A simple model of a continuous cylindrical particle beam with the self-field components E_r and B_θ.

$\vec{E}$, and moving particles by their self-magnetic field $\vec{B}$. A simplified particle beam as a long cylinder with a homogeneous charge density ρ and radius R, which moves with the velocity $\vec{\nu}$ in the $z-$direction as seen in Figure 3.12, can show that the field components E_r and B_θ play an essential role. The field components E_r and B_θ are obtained for the case in Figure 3.12 using Maxwell equations:

$$\frac{1}{\epsilon_0} \int_V \rho \, dV = \oint_A \vec{E} \cdot d\vec{A} \quad \rightarrow \frac{1}{\epsilon_0} \int_V \rho \, r \, dr \, d\theta \, dz = \oint_A E_r \, r \, d\theta \, dz \quad , \quad (3.60)$$

$$\mu_0 \int_A \vec{J} \cdot d\vec{A} = \oint_s \vec{B} \cdot d\vec{s} \quad \rightarrow \mu_0 \int_A \rho \, \nu \, dr \, d\theta = \oint_s B_\theta \, r \, d\theta \quad . \quad (3.61)$$

One can derive the radial electric field E_r and the azimuthal magnetic field B_θ as follows:

$$E_r = \frac{\rho}{2\epsilon_0} r \quad \longleftrightarrow \quad E_r = \frac{I}{2\pi\epsilon_0\beta c}\frac{r}{R^2} \quad , \tag{3.62}$$

$$B_\theta = \frac{\mu_0\rho}{2}\beta c\ r \quad \longleftrightarrow \quad B_\theta = \frac{I}{2\pi\epsilon_0 c^2}\frac{r}{R^2} \quad , \tag{3.63}$$

where the following relations are used as $I = \rho\pi\ R^2\ \nu$, $J = \rho\nu$, and $\mu_0 = \frac{1}{\epsilon_0 c^2}$. While inserting Equations 3.62 and 3.63 into Lorentz force, the radial component of the force, F_r, can be written as:

$$
\begin{aligned}
F_r &= q(E_r - \nu B_\theta) \quad , \\
&= \frac{qI}{2\pi\epsilon_0\beta c}\frac{r}{R^2} - \frac{\nu q I}{2\pi\epsilon_0 c^2}\frac{r}{R^2} \quad , \\
&= \frac{qI}{2\pi\epsilon_0}\frac{r}{R^2}\Big(\frac{1}{\beta c} - \frac{\beta c}{c^2}\Big) \quad , \\
&= \frac{qI}{2\pi\epsilon_0}\frac{r}{R^2}\Big(\frac{1}{\beta c} - \frac{\beta^2}{\beta c}\Big) \quad , \\
&= qE_r(1 - \beta^2) \quad , \\
&= \frac{qE_r}{\gamma^2} \quad .
\end{aligned}
\tag{3.64}
$$

One can interpret that the parenthesis in Equation 3.64 describes the two individual impacts of the electric and magnetic fields; 1 and $-\beta^2$. The primary term indicates electric fields in which the positive sign represents defocusing effect. The latter denotes the magnetic field corresponding to focusing effects. The consequence of the equation in the range of high velocities is the compensation of the repulsive electric force E_r with the attractive magnetic force B_θ. In other words, the space charge has a dominant defocusing effect for non-relativistic cases, mainly relevant for low-energy ion beams with high intensities. Consequently, one of the essential studies on beam dynamics becomes the detrimental effects of space charge.

In computer simulations, space charge calculations necessitate particle tracking to express the transition/evolution of a beam distribution. In theory, the summation of the Coulomb forces between all particles may bring the effects of space charge; however, this approach is not realistic/practical for a 'real' beam distribution, represented

by a collection of particles, since the number of particles is typically 10^8 or more. In practice, the simulations are done by macro-particles of charge q_{mp}. Although computer programs are capable of such numerical calculations, modern computers with advanced technologies/ performances cannot include all particles belonging to the 'real' beam for the calculations.In order to reduce time-consuming/computational exertion, the macro-particle concept is used by using smaller ensembles in the 'actual' beam. Each macro particle carries a multiple of the charge of a real particle, such that the total charge Q_{beam} of the bunch is conserved. As indicated by the number of particles used in the algorithm as N_p, the complexity of the process/ computing operations for space charge calculation by Coulomb force is in the order of $\mathcal{O}(N_p^2)$. A reduction of computing operations can happen when a Cartesian grid is defined by covering the space volume taken by the particle distribution, and the field calculations can be determined to the grid nodes/points. Accordingly, with reasonable simulation particle numbers of N_p, the computing effort, such as $\mathcal{O}(10^{6*2})$ for $\sim 10^6$ simulation particles, can be reduced to the order of $\mathcal{O}(10^{3*2})$ for $\sim 10^3$ grid nodes) as an example. In this regard, macro-particle distribution can be correlated to the simulation particles as:

$$q_{mp} = \frac{Q_{\text{beam}}}{N_p} \quad , \quad \text{and} \quad Q_{\text{beam}} = \frac{I_{\text{beam}}}{f} \quad , \tag{3.65}$$

where Q_{beam} is the charge of the beam, I_{beam} is the beam current, and f is the resonance frequency.

In fact, the algorithm of space charge calculations must fulfill two principles for affordable time consumption and required computational accuracy. While the first one, as mentioned above, is the computational effort of numerical methods concerned with including a large number of macro-particles N_{mp}, the second point is the interpolating methods of the space charge forces related to the suitable calculation techniques. The numerical calculations depend on two particular processes; the meshing technique and the self-field calculation methods. The meshing strategy is one critical feature in the algorithms since well-defined/assigned macro-particles on the spatial grid determine the accuracy of the field calculations on grid coordinates. The Nearest Grid Point (NGP) and the Cloud In Cell (CIC) are two basic techniques,

while the CIC has been used as the primary method in the program BCDC, developed during this thesis. The most direct approach for calculating the self-fields can be provided by the 'Particle-Particle' (PP) method, which needs no grid and no meshing. However, the size of such an algorithm is of order $\mathcal{O}(N_p^2)$, as mentioned before. This complexity can be reduced by distributing the particles on a (Cartesian) grid and calculating the self-field forces between grid points. This method is called the 'Particle-in-Cell' (PIC) algorithm and is of order $\mathcal{O}(N_g^2)$, where N_g is the number of defined grid points.

3.5.1 The PIC Method With Meshing Techniques And The Field Interpolation

Figure 3.13 indicates the diagram of the BCDC program and the outline of such a calculation. The process starts with a number of generated macro-particles from a well-defined and selected initial distribution in spatial and momentum coordinates, and Figure 3.14 shows a beam distribution example within the meshed box. In this example, the equally charged distribution is deposited on a 3D Cartesian/rectangular grid with the dimensions of the selected beam pipe sizes and the period length. Then the space charge fields are achieved by analyzing particle interactions on the grid. The field computations are interpolated to the particles according to their belonging cells, and the resulting particle motions are calculated by giving kicks according to each macro-particle momentum.

The meshing techniques of NGP and CIC

Before depositing the charges on the related grid nodes, one should describe the cells by dividing the grid box length L_x, L_y, and L_z into uniform rectangular meshes of dimensions $N_x \times N_y \times N_z$. The size of one cell is obtained as an example in $x-$direction as $\Delta x = \frac{L_x}{N_x}$, etc. After defining the 3D volume boundaries of the cells, the weighting function of the grid nodes has to be found by partitioning each particle according to the belonging cell. The Nearest-Grid-Point (NGP) and the Cloud-in-Cell (CIC) methods [17], shown in Figure 3.15 are the common choices for computing the weighting function to apply one space charge kick. In the NGP
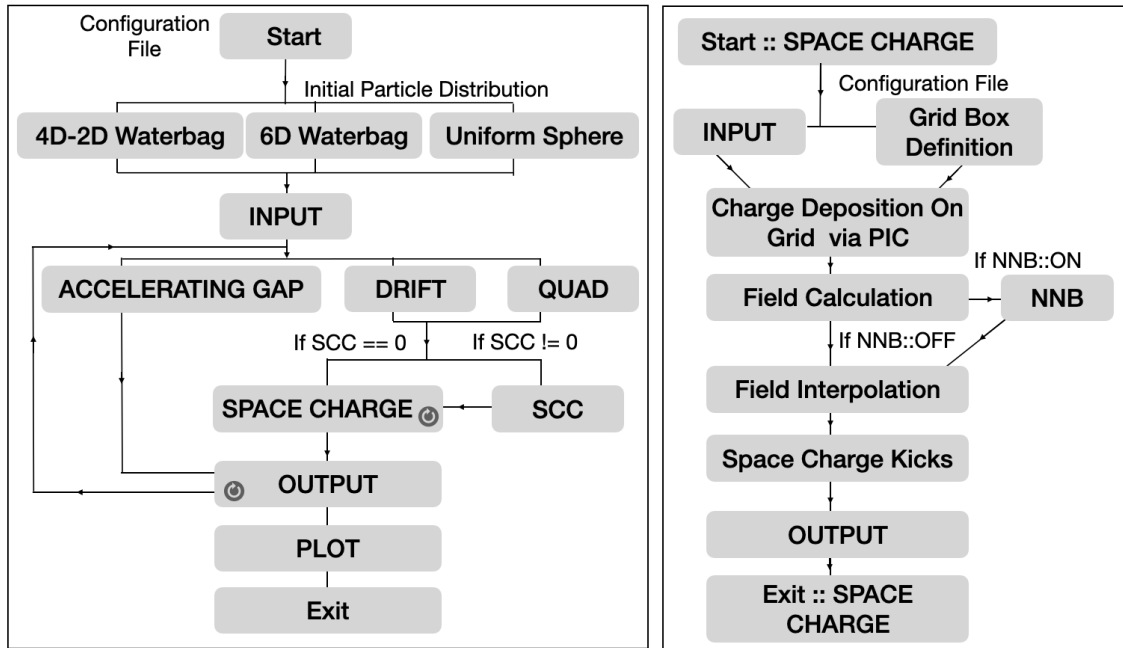
Figure 3.13: The charts of the operations in the BCDC program. The steps in the program (left) and the routine of the space charge (right).

technique, shown in Figure 3.15a, the particles are assigned to the nearest grid points in which the particle is counted as either in or out of a defined region, and the computation becomes a staircase model. Since the electric field near the boundaries evolves critically, the resultant force computation near the borders must be more accurate. Thus this method might be notoriously inaccurate for the charge deposition concerning the purpose of smooth field calculations. On the contrary, as a usual method, the CIC approach is one of the preferences for meshing structures to achieve more precision in the computations; for example, the BCDC simulation program mentioned in Chapter 5 is based on the CIC technique as a good compromise with respect to computing time and accuracy.

According to the CIC, shown in Figure 3.15b, the electric charge of every macro-particle i with its coordinates (x_i, y_i, z_i) is distributed among the nearest eight nodes, where the particle is included in the allocated cell. The charge of each macro particle is distributed to the eight neighboring grid points according to the overlap of the charge density with the eight grid cells, as indicated by the colors yellow, green, blue, and pink. Hence, the weight function $W_g(x_g, y_g, z_g)$ and the charge deposition onto
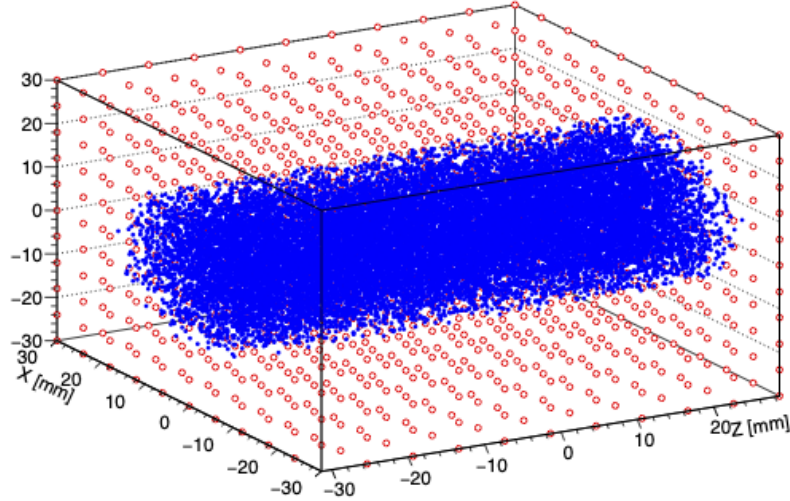
Figure 3.14: The graph shows a represented continuous (4D-KV) beam distribution of transversal radius 18 mm on a grid box of length 60 mm. Each dimension is split into 11 grid points.

the grid $q_g(x_g,y_g,z_g)$ can be described as:

$$W_g(x_g,y_g,z_g) \quad = \quad \Sigma_{i=1}^{N_{mp}}\left(\Sigma_{x_g=1}^{n_x}\Sigma_{y_g=1}^{n_y}\Sigma_{z_g=1}^{n_z}\left(1 - \frac{|x_g - x_i|}{\Delta x}\right)\right. \tag{3.66}$$

$$\left.\cdot\left(1 - \frac{|y_g - y_i|}{\Delta y}\right)\cdot\left(1 - \frac{|z_g - z_i|}{\Delta z}\right)\right), \tag{3.67}$$

$$q_g(x_g,y_g,z_g) \quad = \quad q_{mp}\cdot\left(\Sigma_{x_g=1}^{n_x}\Sigma_{y_g=1}^{n_y}\Sigma_{z_g=1}^{n_z} W_g(x_g,y_g,z_g)\right), \tag{3.68}$$

where the subscript g denotes the coordinates of the grid points/nodes.

Thus, the charge clouds model becomes equivalent to the point charges model by the operation/process of the grid and distribution of charge of every particle among grid nodes. In this regard, the PIC method with the CIC approach satisfies the necessary accuracy and required computing time.

The space charge action has quite different responses according to particle distributions. The uniform spherical in 3D, 4D-KV (Kapchinsky-Vladimirsky), 4D-2D waterbag, and 6D waterbag distributions are defined in the BCDC simulation as the four fundamental distribution functions [19]. The so-called waterbag distributions of $4D - 2D$ $(x,x',y,y',-W,\phi)$ and 6D (x,x',y,y',W,ϕ) are the general use for unbunched beam distributions, respectively. While the 4D space in the transverse plane is

(a) The NGP Method.

(b) The CIC method.
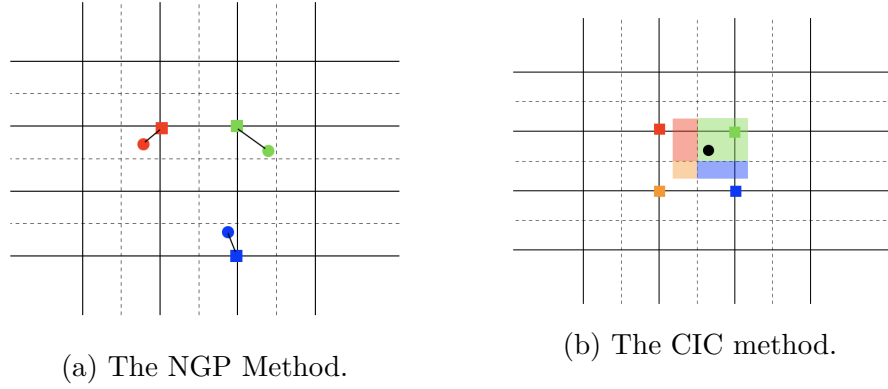
Figure 3.15: Meshing Structures [18]

defined as the phase spaces of x and y, the 2D space is described as the phase space of $W - \phi$. It is worth mentioning that the energy-phase components express the particle energies that are not monoenergetic but uniformly distributed between 0 and a particular maximum. The waterbag distributions in 4D-2D and 6D, as seen in Figures 3.16b and 3.16c respectively, are filled by using the equations shown in Table 3.1. Besides these standard distributions, a uniform 3D spherical distribution, as an example seen in Figure 3.16d with a radius of $R = 20$ mm, is specifically defined in the BCDC program as a test case in benchmarking.

Table 3.1: Inequations for beam distributions [19].

Distribution	Inequation
4D-Waterbag uniform in z	$x^2 + x'^2 + y^2 + y'^2 \leq 1$ and $|z| \leq 1$
4D-2D Waterbag	$x^2 + x'^2 + y^2 + y'^2 \leq 1$ and $z^2 + z'^2 \leq 1$
6D-Waterbag	$x^2 + x'^2 + y^2 + y'^2 + z^2 + z'^2 \leq 1$
Spherical-3D	$r = \sqrt{x^2 + y^2 + z^2}$

The Electric Field Calculation

Utilizing the charge density on the grid, one can begin to compute the Coulomb forces between the grid points under the open boundary conditions. Considering the set of N_{mp} discrete macro particles, the self-electric field $\vec{E}(\vec{r})$ between the grid points can be formulated as:

$$\vec{E}(\vec{r_j}) \;\; = \;\; \frac{1}{4\pi\epsilon_0} \sum_{i=1}^{N_g} q_g \frac{\vec{r_j} - \vec{r_i}}{|\vec{r_j} - \vec{r_i}|^3} \quad , \tag{3.69}$$

(a) The 4D Waterbag, uniform in Z.

(b) The 4D-2D Waterbag.

(c) The 6D Waterbag.

(d) The uniform 3D-sphere.
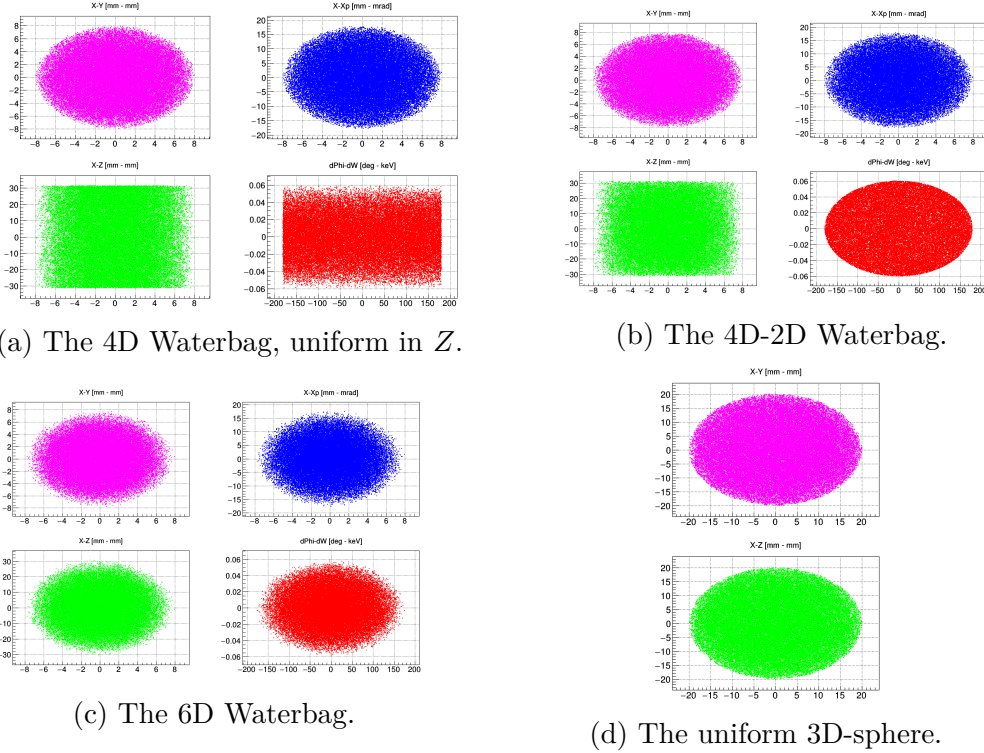
Figure 3.16: The four different types of particle distributions. Each set of the first three distributions is plotted in the two spatial planes ($X - Y$ and $X - Z$) and two of the phase space planes ($X - Xp$ and $\Delta\phi - \Delta W$). The distribution in the $Y-$direction would be similar since the transversal distribution is symmetric. The plot on the bottom right is the uniformly 3D-spherical distribution described as a test case usage.

where $\vec{r_i}$ is the position of the grid point i with the calculated charge q_g, and $r_j \neq r_i$. After calculating the electric field according to the grid-grid interactions as in Equation 3.69, the fields must be interpolated to the positions of the particles, and the resultant force has to be applied to all particles. As an example of the computing procedure, consider that a uniform spherical beam distribution of radius 25 mm within the grid box of the size of ~ 63 mm is simulated with $50k$ (50000) particles as seen in Figure 3.18. In simulations, the box length in the beam axis usually corresponds to the period length, and in this example, the distance between two grid points is equal to $\Delta_g \sim 3.3$ mm for $23 \times 23 \times 24$ grid points in 3D, where $\beta\lambda =\sim 63$ mm. In addition to that, as an example, 18 grid points in the $z-$ direction, out of 24, are included in the particle distribution.

After adjusting the simulated parameters into the described box as seen in Fig-
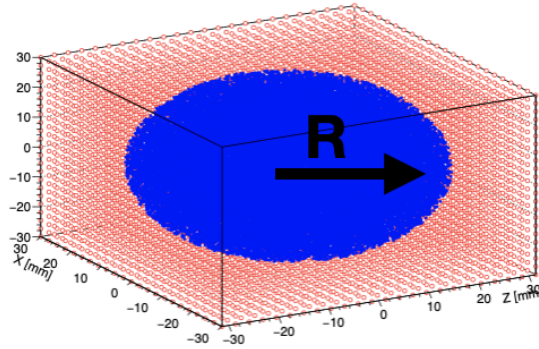
Figure 3.17: The represented beam distribution in a bucket is shown for a uniformly 3D-spherical beam with 25 mm radius filled into the 60 mm ×60 mm ×63 mm sized-grid box.
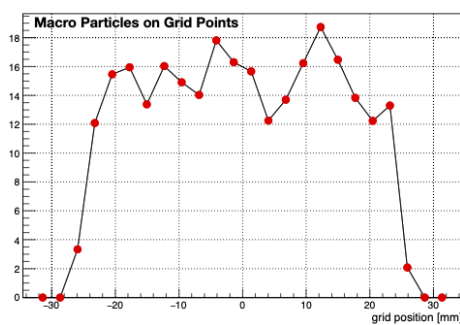
(a) The assigned particles on grid points at the position $(0,0,z)$.
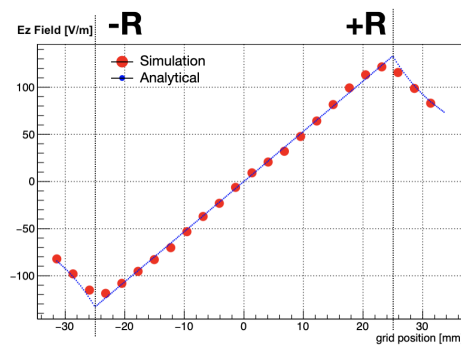
(b) The analytical and calculated electric fields.

Figure 3.18: The plot on the left demonstrates the deposited particles on grid points at the position $(0,0,z)$. The graph on the right shows the analytical and simulated calculations of the electric fields in the $z-$direction.

ure 3.17, the particles are deposited on the grid points according to the CIC method (an example charge assignment at the position $(0,0,z)$ is shown in Figure 3.18a), and the electric fields in the $z-$direction of such a beam are calculated as demonstrated in Figure 3.18b. While, as seen in the figure, the electric fields around the beam center fulfill the analytical solutions, the calculated fields for the beam distribution at closing the edge and outside slightly deviate. These differences bring importance to space charge computations, especially for using a continuous beam, where one of the purposes of developing the BCDC algorithm is to investigate such deviations carefully. In the next section, the statistical discussions on the numeric computations for space charge calculation will be examined as formulated in the program.
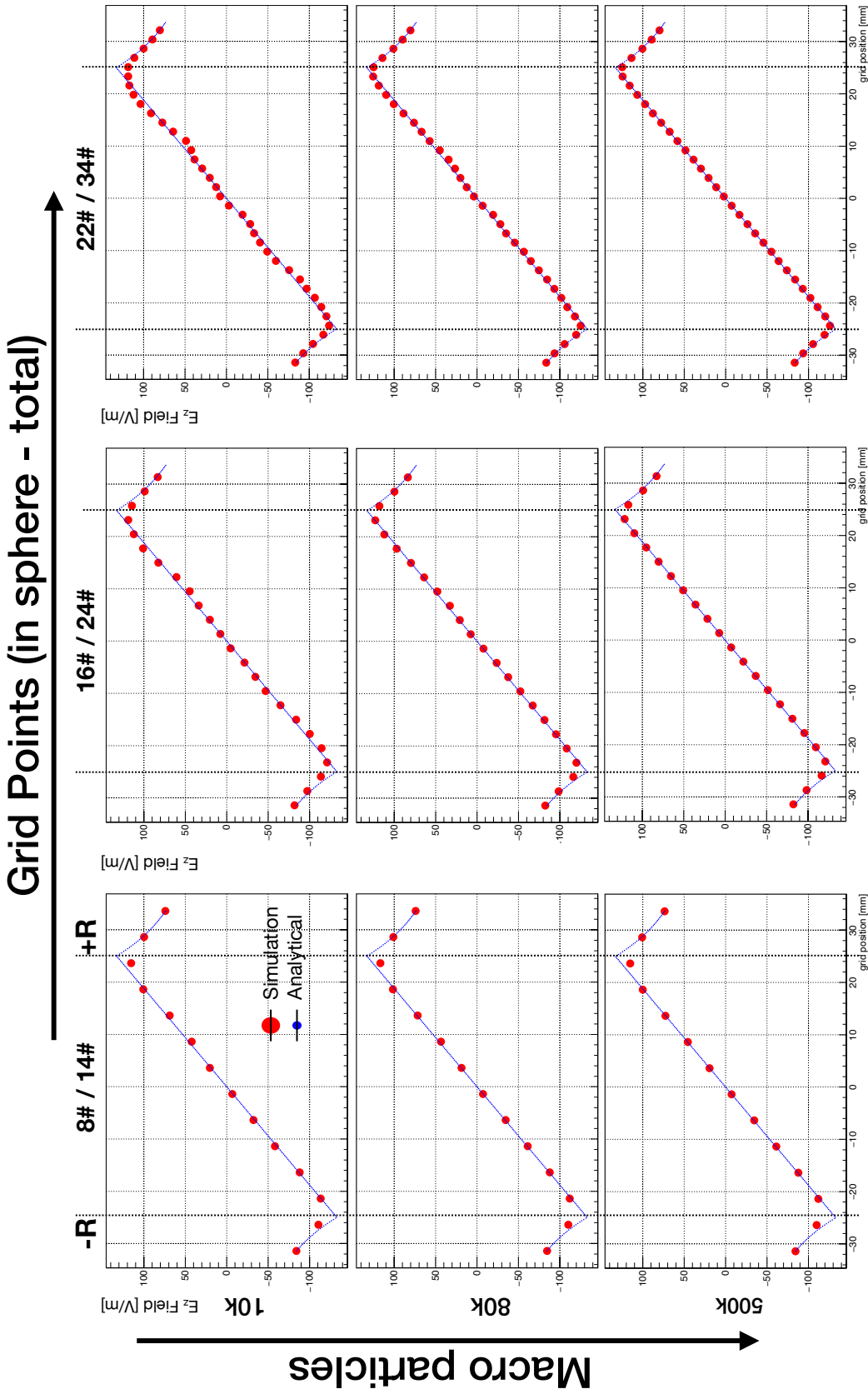
Figure 3.19: The graphs demonstrate the analytic (blue) and the simulation (red) results of the calculated electric field for a uniform spherical distribution. The plots from the left side through the right side show the results with the change of grid numbers at 13, 23, and 33. The graphs from the top through the bottom indicate the calculations done by altering the number of particles used at 10k, 80k and 500k.

Statistical Discussions For BCDC Algorithm

The simplest way of validating a numeric calculation is to compare the numerical computation with the analytical one. The analytical field is $E_r \propto r$ for the inside of the spherical region and $E_r \propto \frac{1}{r^2}$ for the outside area. In this regard, the graphs in Figure 3.19 show the statistical precision of the field computations by using a spherical distribution of 25 mm radius inserted into the rectangular volume with 60 mm×60 mm×63 mm. The results of the analytic calculation (blue) with the simulation (red) are illustrated in the figure. The graphs clearly indicate that the electric fields inside the sphere within the radius of 25 mm are linear, and the electric fields outside are $\propto \frac{1}{r^2}$. Although the compared results of analytical and simulated fields at each plot are agreed with each other, as seen in the figure, the study indicates that the accuracy of the simulation quantitatively depends on two factors; the number of grid points N_g and the number of particles N_p in the distribution. The simulated distributions are uniform spheres with the numbers of $10k$, $80k$, or $500k$ particles, and the grid spacings Δ_g are increased in $\sim 1,8$ mm, $\sim 2,7$ mm, and ~ 5.0 mm, where the grid boxes split into N_gs of $(33 \times 33 \times 34)$, $(23 \times 23 \times 24)$, and $(13 \times 13 \times 14)$ into three dimensions (for an example of visualizing the beam into the box, see in Figure 3.17).

By increasing N_p at a given N_g, the result may be always improved, as seen in the plots from the top through the bottom in the figure. It is evident that the choice of the grid-grid interaction method gives sufficient accuracy in the calculations, even with a much smaller number of grid points N_g, compared to large particle numbers N_p. While the number of macro particles in the simulation influences the precision of the field calculations, the accuracy is particularly based on how many grid points are included in the particle distributions. Although the best accuracy from the field calculations, especially at the edge of beam distributions, is expected, one cannot obtain a case like the simulation, done by the highest N_p and N_g as seen in the plot on the bottom right in Figure 3.19; since such a particle distribution with a sudden drop in density from constant to zero at the border is not realistic. In other words, the transition of the space charge field in the real bunch is usually much softer. Therefore such an extreme case can be a hard test case for benchmarking the algorithm. In practice, a good representation of the field computation in the

simulation might be the one in the middle of Figure 3.19 since the resulting fields of analytical and simulated ones are well-matched. Besides them, the graph on the top right in Figure 3.19 indicates the worst case in this simulation, $33 \times 33 \times 34$ grid points and 10k particles while having N_g similar ranges with N_p brings inhomogeneity in the computation, which means that there are many grid points are completely free of particles. Such a scenario is never used in simulations since it causes increasing the computing time by losing accuracy. Hence, this worst case can be taken as another proof of using the correct/effective method in the algorithm since it is impracticable.
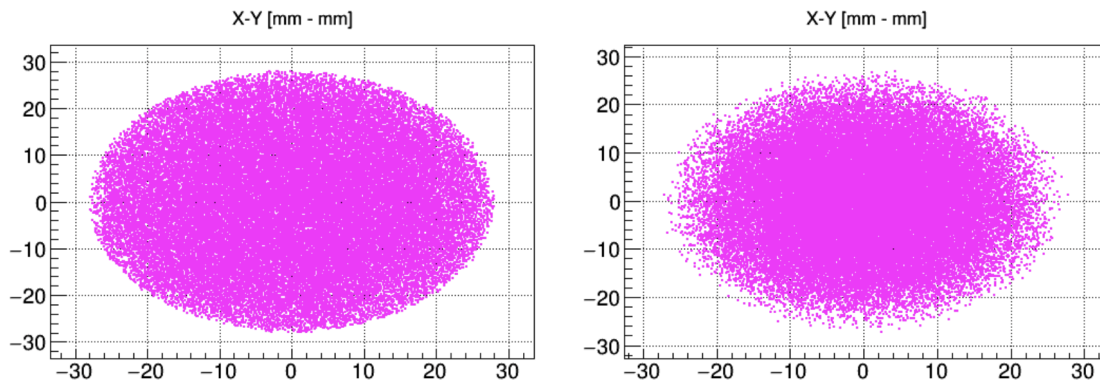
Figure 3.20: The plots show the uniform spherical (left) and 6d waterbag(right) distributions with 28 mm transversal size.

Regarding the dependence of space charge calculations on the beam distribution used in simulations, two specific distribution sorts are compared here as an example; While one is uniformly spherical beam distribution, the other is 6d-waterbag beam distribution, where both distributions, as shown in Figure 3.20, are generated as a round beam with 28 mm radius inserted into the rectangular volume with 60 mm$\times$60 mm$\times$63 mm. The grid box is split into $23 \times 23 \times 24$ with the grid spacing of ~ 2.7 mm, and for example, 20 grid points out of 24 in the $z-$ direction are filled with the simulated distributions. According to these configurations, the resulting field calculations in Figure 3.21 indicate the dissimilarity of these two distributions, where the choice of suitable distribution is an essential factor for simulations.

In conclusion, the number of grid points N_g is an important parameter, especially for an unbunched beam, because the accuracy at the edge of the distribution becomes critical. The number of simulation particles is a decisive factor for the precision of the simulation, especially for a bunched beam. Likewise, both unbunched and
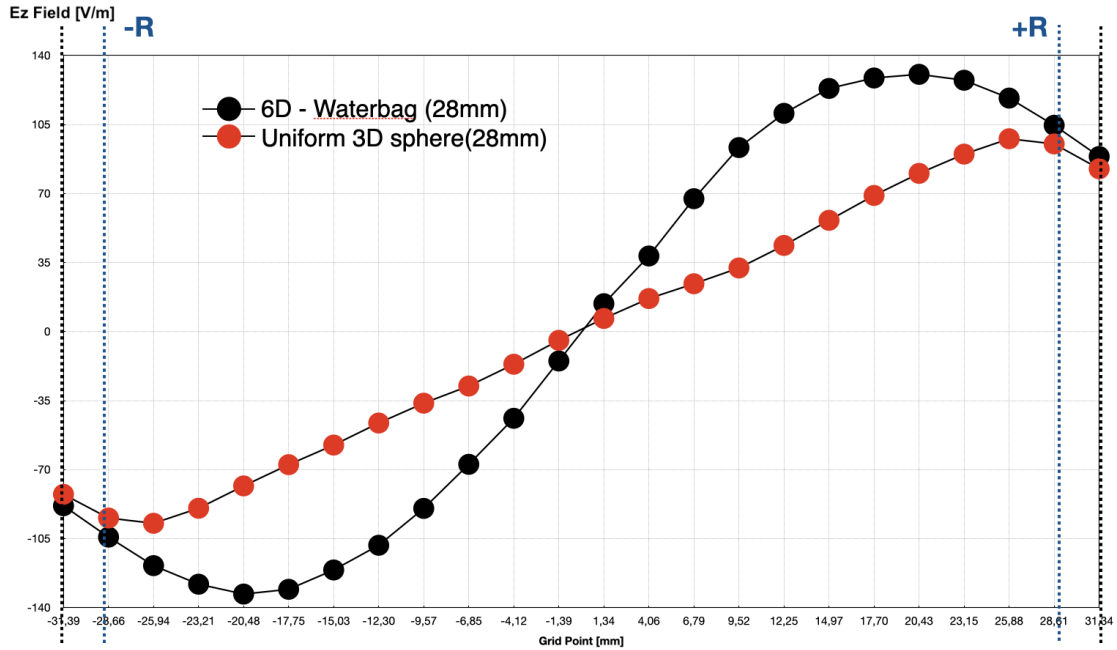
Figure 3.21: The electric field calculations $E_z(0,0,z)$ for the distributions shown in Figure 3.20.

bunched beam representations used in the simulations in this thesis are influenced by the type of distributions.

The Field Interpolation

Since the field calculation is done on the grid nodes due to the reduction of computing complexity, the intermediate values of the field calculation must be constructed by the interpolation method with that discrete set of grid points. The so-called triple interpolation method is used in the BCDC in order to eliminate the staircase model and achieve smooth field calculations [20]. (For a detailed explanation fo the trilinear method and its formulas see Appendix A.)

It is clearly seen in Figure 3.22 that the plots on the left side are the results of the field calculation without using the interpolation method. By increasing the number of particles, the trend of the staircase model becomes much more apparent. Moreover, the tendency shows a limit of discretization of the numerical simulations because of being a statistical study. When the interpolation technique is included in the results, this behavior becomes smoother, as demonstrated in the graphs on
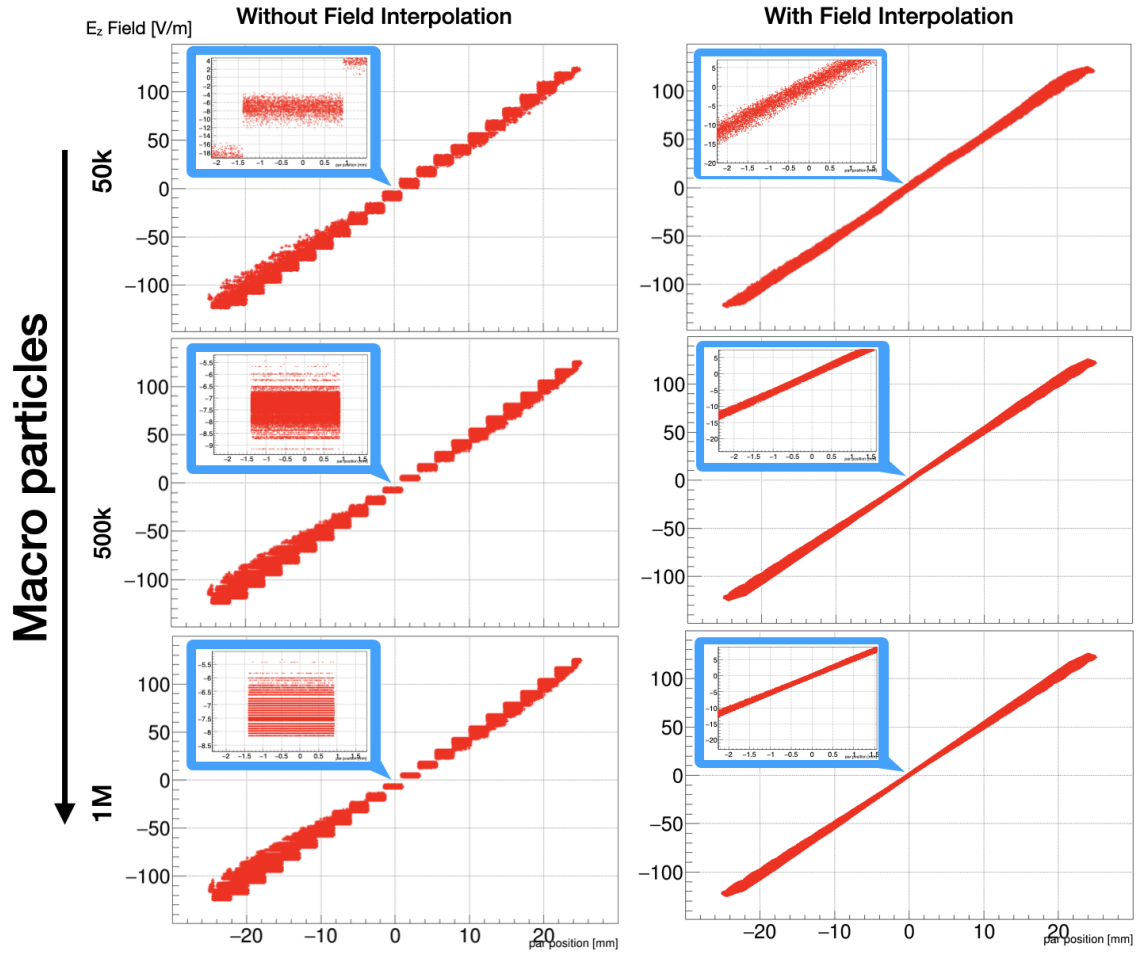
Figure 3.22: The graphs show the electric field calculations without and with interpolating fields of the uniformly 3D spherical distributions by increasing the number of simulated particles to $50k$, $500k$, and $1M$.

the right in Figure 3.22. This statistical study is explained in detail in Appendix B. As a result, the trilinear interpolation fits the purpose of finding the interval values between the calculated electric fields on the grid points and brings accuracy to the simulations.

Space Charge Forces With Equation Of Motion

Since the interactions among the particles become the ones among the grid nodes, the influence on the motions of particles must be interpolated back to the macro-particle position for momentum update. From the Lorentz force equations, the change of the particle motions (i.e. positions and momenta) can be written with respect to the 6D

phase space coordinates as:

$$\Delta x_i = \Delta x_i' \cdot \frac{l}{2} \quad , \tag{3.70}$$

$$\Delta x_i' = \frac{q_{mp} \cdot E_{x,i} \cdot l}{A \cdot m_0 \cdot \gamma_{i,0}(\beta_i^0 \cdot c)^2} \quad , \tag{3.71}$$

$$\Delta W_i = A \cdot E_{z,i} \cdot l \quad , \tag{3.72}$$

$$\Delta \phi_i = \frac{360°}{n \cdot \lambda} \cdot \left(\frac{1}{\beta_{i,1}} - \frac{1}{\beta_{i,0}} \right) \cdot \frac{l}{2} \quad , \tag{3.73}$$

where l is the step length for the space charge calculation, A is the atomic unit of the particle used, m_0 is the mass for proton, c is the speed of light, $E_{x,i}$ and $E_{z,i}$ are the calculated electric fields in x and z directions, respectively, $\gamma_{i,0}$ and $\beta_{i,0}$ are the relativistic factors for the initial conditions of the particle distribution, and $\beta_{i,1}$ is the relativistic velocity of the particle distribution at the end.

3.5.2 Neighbored Bunch Concept

At linac beam simulations, each bunched beam is contained within one RF bucket, whose length corresponds to $L = \beta\lambda$. Therefore the numeric computations must be fulfilled by adjusting the box length according to that. The schematic in Figure 3.23b
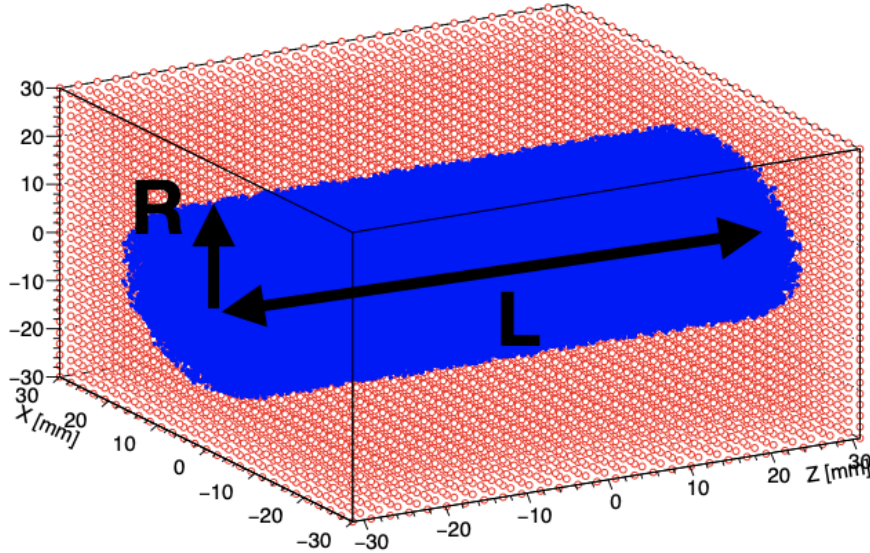
(a) The simulated continuous beam in a defined grid box with length $\beta\lambda$.
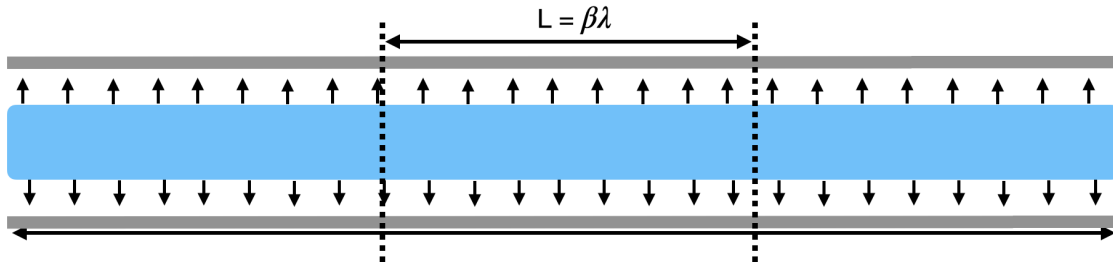
(b) The schematic of a continuous real beam filled into a "3 $\beta\lambda$" grid.

Figure 3.23: The picture on the top indicates a represented beam distribution in a bucket for a continuous cylindrical beam filled with 30 mm diameter and 62 mm length into the 60 mm ×60 mm ×62 mm sized-grid box. The schematic on the bottom shows a three-sized grid filled with a continuous beam, as shown in blue.

indicates a realistic case for a continuous beam that occupies a three-sized bucket. In this reality, the radial electric field E_r will evolve inside the volume, where the electric field outside is $E_r \propto \frac{1}{r}$, and the one inside is $E_r \propto r$. Further, the electric field at the edge of the $z-$ direction E_z is zero due to the continuous distribution. Although this is theoretically correct, in a linac beam simulation for such a distribution, the zero

fields at the border and outside of the $\beta\lambda$-sized grid box are not valid; because the simulation does not include the corresponding field coming from the adjacent regions. Therefore, this non-physical effect can be compensated by adding the previous and the next buckets in which the concept of the next neighboring bunch (NNB) has been developed in the BCDC program.

In the example shown in Figure 3.23a, a uniform continuous distribution of diameter 30 mm and the length of 62 mm is used in the simulation to explain the concept of the NNB, where the radius of the distribution is a similar size to the box of 62 mm. The electric fields along the $z-$ direction near the grid walls should be close to zero according to the law when the beam is continuous; however, the simulation result shows in Figure 3.24a that the electric fields do not get down to zero. Therefore, the NNB concept is integrated into the space charge calculation by filling the adjacent grid volumes to the main one. In Figure 3.24b, while the main box is highlighted by
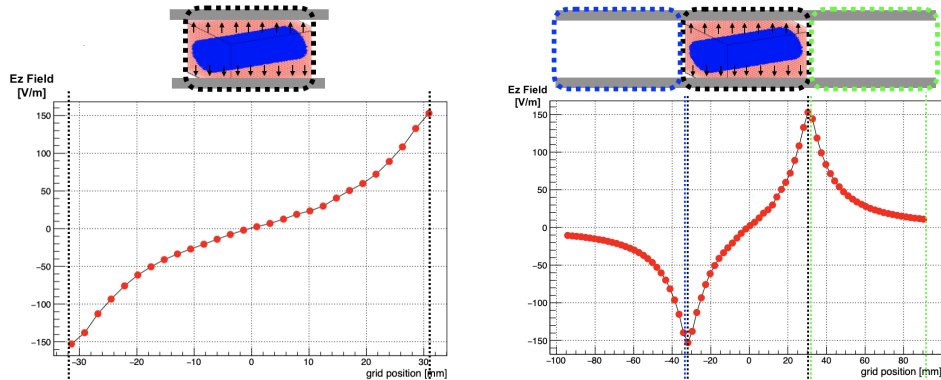
(a) The electric fields on the main box.

(b) The electric fields by extending to the adjacent two boxes.

Figure 3.24: The plots indicate the calculated electric fields in the $z-$direction. While the one on the right shows the resulting field for the main grid box, labeled with black, the other demonstrates the electric field calculation by expanding the previous (blue) and the next (green) regions.

a black rectangle, the previous and the adjacent buckets are labeled with blue and green, respectively. The computation with the 3 $\beta\lambda$ grid gets closer to the expected values (zeros) near the walls.

Since the expanded fields are observed equally for all defined volumes, Figure 3.25 illustrates the contributions of the previous (blue) and following (green) buckets onto the interested region labeled with black. Thus, to achieve the net resulting fields on
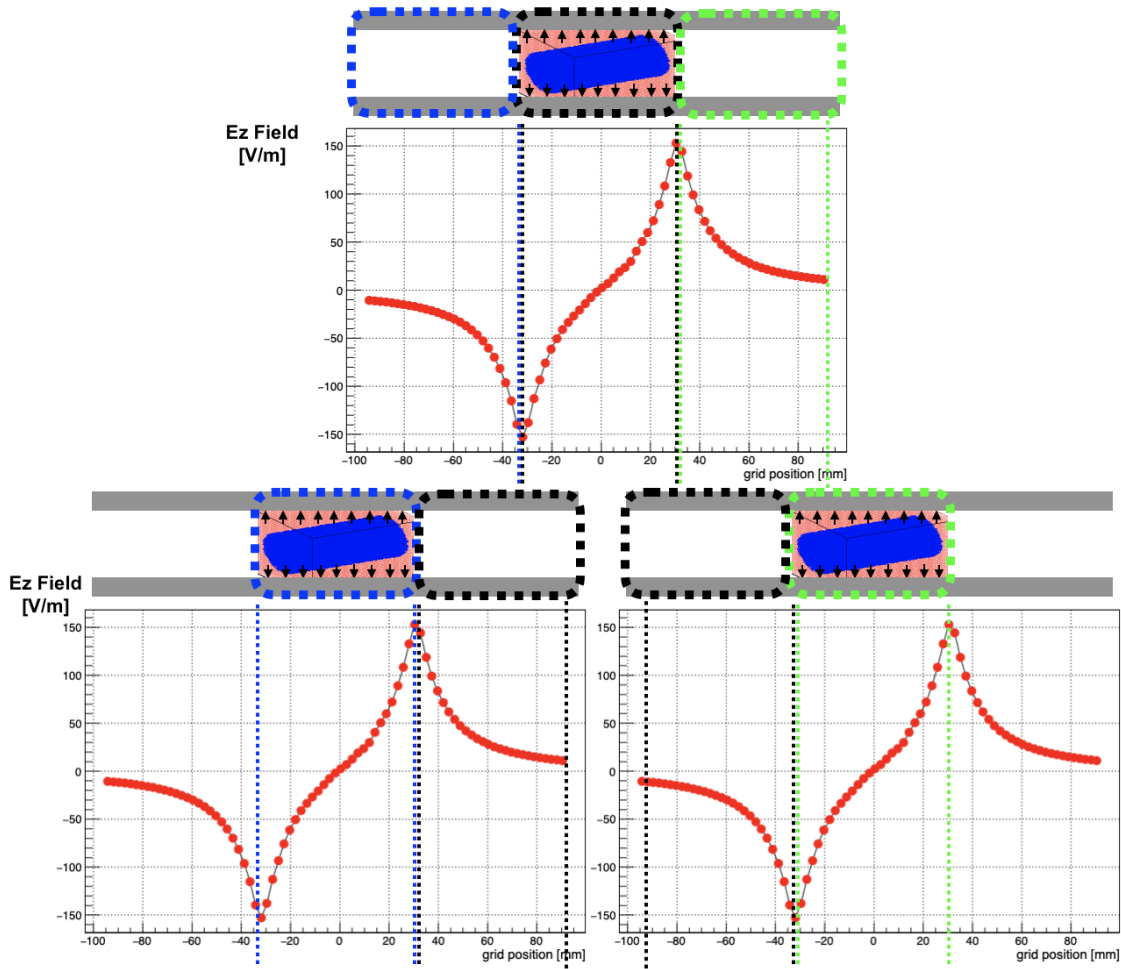
Figure 3.25: The next neighbored bunches concept for shifting the main grids onto the next neighbored ones.

the main box, one can overlap the electric field calculated in the main grid box with the ones from the neighboring regions. The BCDC program uses a shifting technique to get the resulting field computations by calculating the electric fields for the $\beta\lambda$ grid three times larger than the original dimension and shifting these fields to the previous and the front grid boxes. According to the shifts, the resulting fields in the main grid box (labeled with black) are recalculated/redone by overlapping with the electric fields under the black rectangular regions, as seen in Figure 3.25, to find the total and realistic electric forces. With this particular technique, the space charge effect on the borders without or with the adjacent boxes, respectively, can be seen in Figure 3.26, and the simulations become more realistic and accurate.
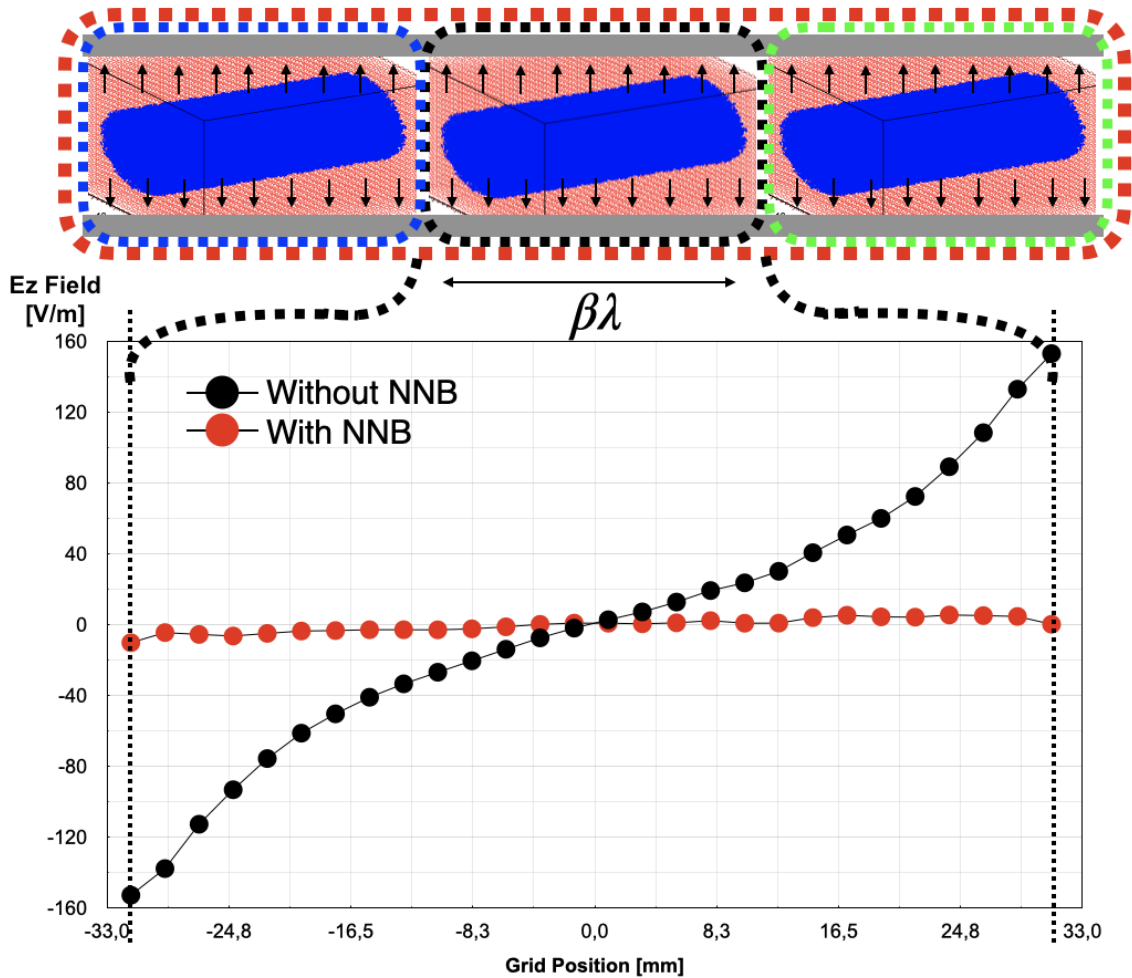
Figure 3.26: The field calculations without and with the NNB concept.

In addition to this example, a set of distributions with distinct lengths for a test simulation are generated as the sequence of one likely unbunched beam and four bunched ones with different sizes. The field computations for four uniformly continuous and cylindrical beams filled with several lengths into the same box dimension, as in Figure 3.23a, are done and plotted to Figure 3.27. While the plots with different colors indicate the simulated beam distributions with various lengths, the traces with the same color and unlike symbols demonstrate the resulting field calculations without and with the NNB concept. In the figure, the difference of the resulting fields between not included and included the next neighboring bunches is obviously seen; but the dramatic effect for the case focused in this study is pointed up the plots labeled with red, where the beam is likely to be a continuous one. With
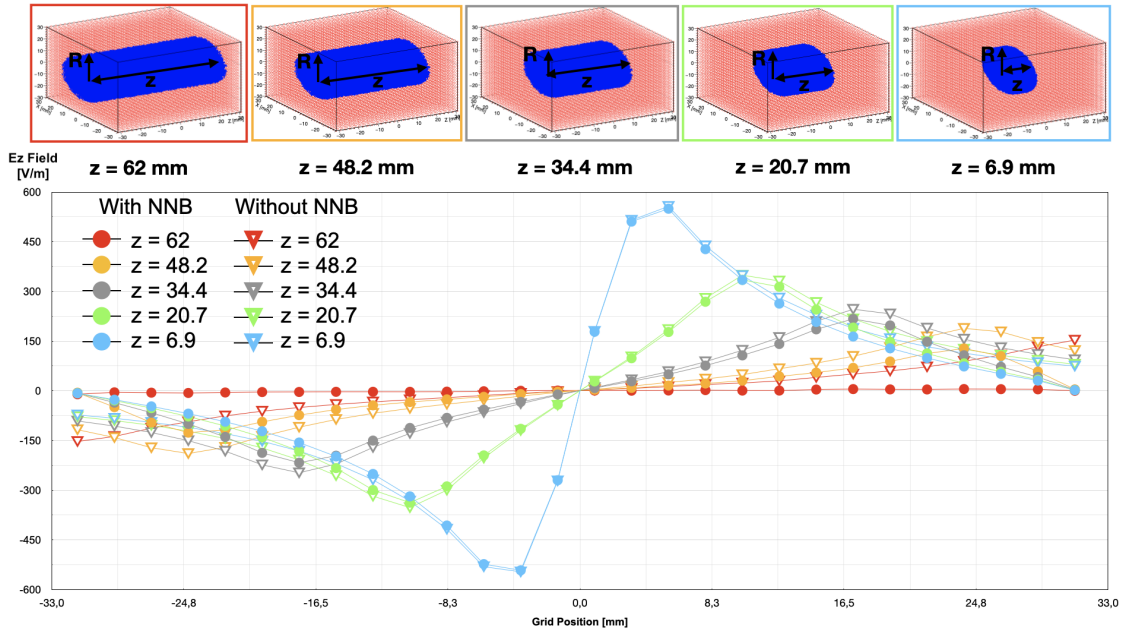
Figure 3.27: The effects on the field calculations for distinct beam sizes during bunch formation, without and with the NNB concept.

the contribution of the neighboring buckets to the space charge computation, the resulting electric field in the $z-$direction is calculated successfully by eliminating the high field estimation at the end of the defined walls, which are the non-physical effects for such a continuous piece of the beam. In conclusion, the NNB concept is a powerful method in linac simulations, especially for realistic field calculations at the borders of the simulated/interested region.

3.5.3 The Impacts of The NNB Routine

In order to understand the performances of the NNB routine, a numeric simulation, including a beam current of 10 mA, has been done under realistic conditions, operating the NNB routine, as shown in the output distributions in Figure 3.28. The same design as described in Section 5.3.3 is used. The voltage settings are optimized for a sharp focus at 0 mA beam current.

Figure 3.28 illustrates the simulation results with 0 mA (left) and 10 mA in the absence (middle) together with the presence (right) of the NNB operation. When the simulation contains a beam current, like 10 mA, the output beam distribution in the focus plane is considerably widened. However, the middle plot in the figure
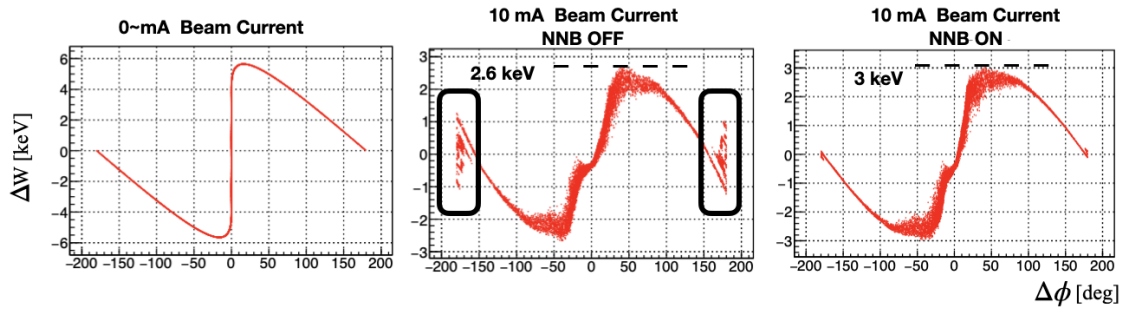
Figure 3.28: The plots show the impact of the NNB routine on a design for 100 keV proton beam.

demonstrates that an artificial impact in the field calculation is observed by a lack of the NNB routine, as marked by circling the head and tail with the rectangular boxes in the figure. When the routine is activated, these non-physical impacts disappear (see the figure on the right). This confirms the findings, as plotted by Figure 3.27. Moreover, the core of the resulting distribution is affected. The energy spread is reduced by the space charge action. However, this effect would be overestimated without including the NNB - action. The bunch width at fixed buncher amplitudes is larger when excluding the NNB - action

3.5.4 The Concept of Space Charge Compensation (SCC) In A Bunching System

At the low energy transport section, the space charge forces cause serious effects, and ionizing the residual gas inside the vacuum chamber would be one solution to reduce this effect [21]. The beam inside the beampipe creates the ionization of the residual gas due to not having a hundred percent vacuum in the chamber (the worse the vacuum pressure - the better the space charge compensation). This unavoidable ionization of the residual gas decreases the charge density of the beam; hence, it leads to some reduction in the total charge density of the beam. Thus, the space charge forces can be less severe depending on the current and velocity of the beam and the vacuum pressure.

A positively charged beam has an attractive potential for negative charges, i.e., electrons. Electrons could be provided by collisions of the primary beam particles with residual gas atoms, which are always present inside the beam pipe (vacuum chamber). Therefore, the residual gas atoms are ionized, and the generated free electrons are trapped inside the potential of the primary beam. Furthermore, due to the ionization of the gas, the positively charged ions in the residual gas are driven out of the beam, and these repulsed ions would hit the metallic walls/chamber. Consequently, secondary electrons would arise and tend to drop the potential of the primary beam additionally. Through the process, the net charge of the beam is reduced by the negatively charged trapped electrons. This process is called space charge compensation and can be defined as a percentage (e.g. 90%) of the beam current. Although the compensation degree can be quite high, sometimes even closer to 100%, in accelerator sections, like drift spaces, which are free of electric fields, the full beam current must be applied for beam dynamics calculations along other accelerator components, like DTLs or RFQs, due to absorption of all electrons by external electric fields.

In the BCDC, the so-called space charge compensation mode - SCC can be activated optionally. All the beam dynamics analyses under this feature follow this concept, as explained above. The level of SCC is determined on different regions of an accelerator line, as shown in Figure 3.29. The green part represents where the bunching system is located, and all simulations are done by assuming zero compensation in this area
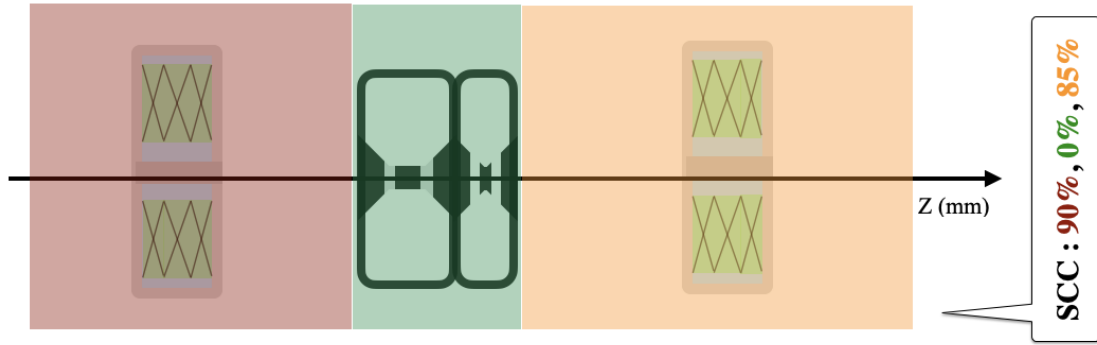
Figure 3.29: The scheme of an accelerator line with a bunching system. Three colors on this line represent different partial SCC ratios that are applied on these regions.

(i.e. full beam current is valid) since the rf fields are dominant inside the system. On the other hand, the other regions include partial space charge compensation in which the typical value of 90% is based on measurements at existing accelerators [21] and theoretical/ numerical investigations [22] on DC beams. Although 90% SCC is assumed at the front side of the buncher system due to having a DC beam, the end drift should contain less space charge compensation (e.g. 85%) due to a bunched beam traveling along the last section. The compensation rate for a bunched beam might be less because the electron capturing rate is different than the content on a continuous beam because of having a more complex electron capture mechanism [23].

Chapter 4

Principles of Harmonic Bunching And Optimized Configurations

The beam dynamics of bunch formation will be the first topic of this chapter. The bunching systems will be explained with several classifications:

- direct linac injection without any buncher system,

- with a multi-harmonic bunching system,

- with one harmonic buncher,

- with drifts between bunchers.

After mentioning the introductory section, a double drift harmonic bunching (DDHB) system, as the keystone of this thesis, will be described in many aspects as a separate section.

4.1 Linac Injection Without A Bunching Systems

Drift tube linacs typically have a limited range of longitudinal phase acceptances, usually around $\pm 20°$. When attempting to inject a continuous beam into a DTL with the phase range of $\pm 180°$ at the fundamental frequency, the DTL would selectively accelerate particles within its specified longitudinal acceptance area. Particles outside this range would either generate a big emittance 'halo' or be lost by hitting the beam pipe. Therefore, the efficiency of the capture rate for an unbunched beam

fed in a linac DTL would be significantly low, approximately around 10% (e.g. $\pm 20°/ \pm 180° \approx 10\%$). Additionally, the big emittance, as the insufficient quality of the accelerated beam, would be a direct consequence of the unbunched beam injection.

The IH-DTL section of the Heidelberg Cancer Therapy facility at the clinic in Heidelberg (HIT Heidelberg) serves as an example to illustrate this behavior. This particular IH-DTL operates at the frequency of 216.816 MHz and covers an energy range of 0.4 to 7.0 MeV/u for a design particle of $^{12}C^{4+}$ with a charge-to-mass ratio of 3, $A/q \leq 3$. Remarkably, the energy gain mentioned earlier is achieved using only one IH-DTL cavity comprising 56 $\beta\lambda/2$ periods and three integrated quadrupole triplet lenses. Further details can be found in the schematic in Figure 4.1 and reference [24]. This linac has routinely been at operation for hadron cancer therapy since approximately 2006.
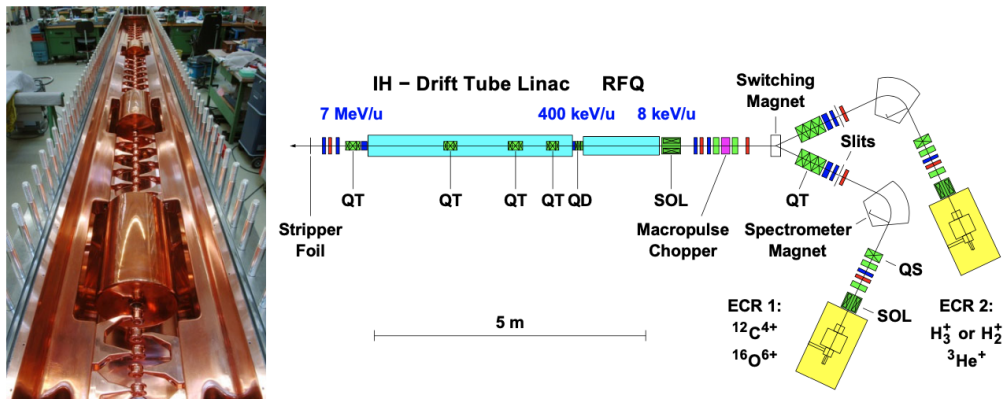
Figure 4.1: View into the 0.4 - 7.0 MeV/u IH-DTL of the Heidelberg Therapy Injector (HIT Facility) and schematic drawing of the injector linac [24].

The beam dynamics concept utilized in this case is referred KONUS, the "combined zero degrees structure" [25]. It allows for highly efficient particle acceleration at low to medium energies, where particles experience an effective acceleration voltage of approximately 20 MV over a length of only 3.7 meters. However, this efficient acceleration gradient provided by the KONUS beam dynamics results in a smaller phase acceptance compared to conventional negative synchronous phase designs. In the current example, when the 0.4 MeV/u beam is injected into the IH-DTL, it has a designed phase spread of $\pm 13.7°$ and an energy spread of $\pm 2.5\%$. In the present investigation [26], the energy spread has been reduced to $\pm 1.0\%$ at injection into the

IH-DTL, and the phase spread has been increased incrementally from $\pm 5°$ to $\pm 10°$, $\pm 15°$, and $\pm 20°$, respectively.

The impact of the IH-DTL longitudinal beam dynamics can be seen in Figure 4.2, which indicates the output beam distributions behind the IH-DTL at 7.0 MeV/u. It becomes evident that there is a significant and sensitive response to variations with respect to the input phase spread. A "tail" formation in the output distribution is created by the "late" and lower energy particles, which is also pronounced at $\pm 15°$. Moreover, this effect becomes more apparent at $\pm 20°$, leading to a filamentation or a halo, and a large increase of the 95% border emittance ellipse would be the consequence. Figure 4.2 shows the specific values, where the output emittance resulting from $\pm 20°$ at the input is more than ten times larger (4.21 keV/u·ns) compared to $\pm 5°$ at the input (0.397 keV/u·ns). This investigation provides a clear opinion that a DTL requires a pre-bunched beam with a typical phase width of around $|20°|$ at its entrance.
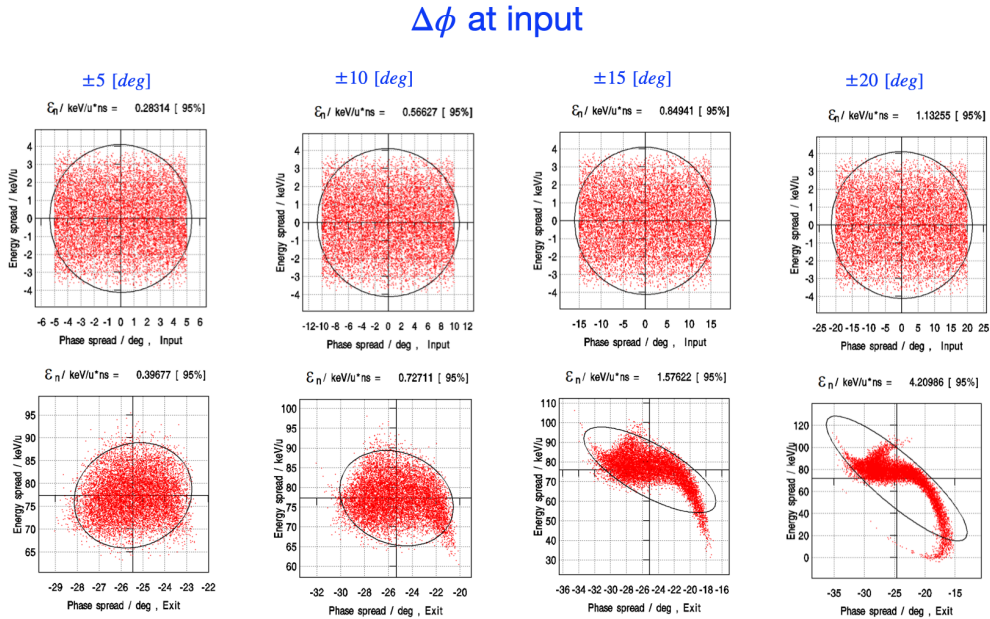
Figure 4.2: Longitudinal particle distributions at the exit (plotted in the bottom) (7.0 MeV/u) of the IH-DTL of the Heidelberg Therapy Injector (HIT Facility) resulting from a variation of the beam phase width at IH-DTL injection (plotted in the top) (0.4 MeV/u) between $\pm 5°$ and $\pm 20°$. Calculations performed with the LORASR code [1] [26].

4.2 Bunching Systems

Before starting with the considerations on a separate bunching system, an accelerator line without such a system can be designed by direct injection into a drift tube linac. However, without prebunching, the limited acceptance of the DTL reduces the performance. Since RFQs unify the three fundamental processes (bunching, focusing, and accelerating) within a compact volume, they are highly demanding structures. Although they provide attractive output beam properties, like high particle transmission and relatively small emittance, due to the complexity of RFQs, more simplified solutions are of interest. Therefore the following section will describe in detail how a separated bunching system can provide the bunches for efficient acceleration in DTLs or cyclotrons, if RFQs with full performance capabilities are not the choice for bunching.

All the individual bunching structures have in common that the buncher system is followed by a drift space, where the energy modulation finally leads to the intended bunch formation at the entrance into the RF accelerator. The bunching systems are investigated in the upcoming section under three categories:

- one buncher cavity acting at the frequency of the RF accelerator,

- one gap fed by a set of harmonic frequencies; including as a basis the accelerator frequency,

- two or more gaps operated at harmonic frequencies and separated by drift spaces from each other.

4.2.1 Bunch Formation

The d.c.-beam, which comes from an ion source, is transformed into particle bunches using buncher cavities followed by drifts and by that matching to the buckets of the next accelerator unit. The saw-tooth voltage would be ideal for bunching; however, the desired ranges/amplitudes, from several kV to about 100 kV, cannot be achieved due to a lack of technological solutions. For a particle beam with an energy uncertainty ΔW at the point of injection, a corresponding phase width results

with a given voltage amplitude in the buncher and a proper drift distance in the longitudinal focus, as seen in Figure 4.3.

(a) Before the buncher.

(b) At the buncher.

(c) After the buncher w/ L.
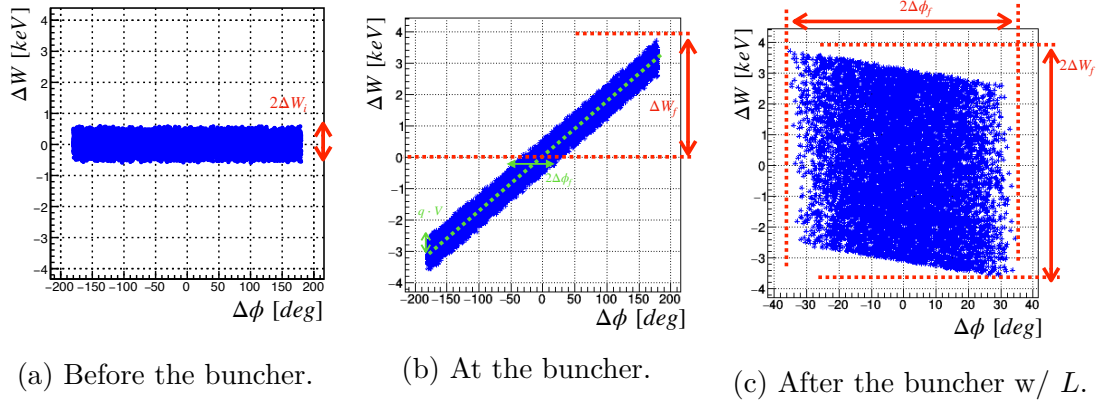
Figure 4.3: The graphs show the transformation in the longitudinal phase space for a saw-tooth buncher with corresponding drift L. $\Delta\phi_f$ represents the semi-phase axis in focus, and ΔW_f stands for the energy semi-axis of the incident beam.

The equation for the RF phase distribution and the position of an arbitrary particle after a drift distance L can be given:

$$\phi(L) = \phi_{z=0} + 2\pi\frac{L}{\nu T} = \phi_{z=0} + \omega\frac{L}{\beta c} \quad , \tag{4.1}$$

where the $\nu = \beta c$ represents the velocity of particle i and the relation between frequency and period is $f = \frac{1}{T}$. In addition to the phase distribution, the phase shift of the particle i, with respect to the synchronous particle s, can be written as:

$$\Delta\phi(L) = \frac{\omega L}{c}\Big(\frac{1}{\beta} - \frac{1}{\beta_s}\Big) \quad . \tag{4.2}$$

Using a Taylor expansion in the case of $|\beta - \beta_s| \ll \beta_s$, the Equation 4.2 becomes:

$$\Delta\phi(L) \cong -\frac{\omega L}{\beta_s^2 c}\delta\beta \quad . \tag{4.3}$$

The relation of the energy offset of a particle and the relativistic parameters β, γ is :

$$\frac{\Delta W}{W_s} = \frac{\Delta\gamma}{\gamma_s} \quad , \tag{4.4}$$

where $W_s = m_0 \cdot c^2 + W_{kin}$ is the total particle energy of the synchronous particle. When one applies the relation given by Equation 4.5 into the energy equation 4.4, one gets:

$$\Delta\gamma \;=\; \gamma - \gamma_s = \sqrt{1 - (\beta_s + \delta\beta)^2} - \sqrt{1 - \beta_s^2} \cong \beta_s \gamma_s^3 \delta\beta \quad, \tag{4.5}$$

$$\rightarrow \quad \frac{\Delta W}{W_s} \simeq \beta_s \gamma_s^2 \delta\beta \quad. \tag{4.6}$$

Inserting $\delta\beta$ from Equation 4.6 into Equation 4.3, one has finally:

$$\Delta\phi(L) \;\cong\; -\frac{\omega L}{\beta_s^3 \gamma_s^2 c} \cdot \frac{\Delta W}{W_s} \quad. \tag{4.7}$$

When the beam is excited by a sinusoidal RF wave $V \cdot \sin(\phi_{i,0})$ followed by a drift L, the energy-phase correlation can be extended for a beam distribution:

$$\text{At z=0 :} \quad \Delta W_i(\phi_{i,0}) \;=\; q \cdot V \cdot \sin(\phi_{i,0}) \quad, \tag{4.8}$$

$$\text{At z=L :} \quad \Delta\phi_{i,L} \;\cong\; -\frac{\omega L}{\beta_s^3 \gamma_s^2 c} \cdot \frac{\Delta W_i(\phi_{i,L})}{W_s} \quad, \tag{4.9}$$

where the index i refers to an arbitrary particle, $z = 0$ denotes the position of the buncher gap, and $z = L$ represents the drift length from the buncher gap center to the focus position.

On the other hand, for example, if a continuous beam with a certain energy spread, as seen in Figure 4.3a, is excited by a sawtoothlike voltage V, as seen in Figure 4.3b, the energy change ΔW is written as:

$$\Delta W = q \cdot V \cdot \frac{\Delta\phi}{\pi} \quad. \tag{4.10}$$

It is apparent in Equation 4.10 that the energy deviation is linearly dependent on the phase change. The plots in Figure 4.3 demonstrate how a bunching formation in the energy and phase transformation is correlated to the buncher voltage and the drift distance.

A wise synthesis of the voltage combined with the distance in focus can provide a bunched beam within an intended phase width. Hence such a bunching system is able to obtain the required output beam features for the following accelerator line. Although the example is given for ideal bunching, the saw-tooth-like voltage cannot be achieved by not only the current technology for the desired amplitudes from kV to 100 kV but also the application method of this ideal wave. Since an RF cavity generates sinusoidal-like or/and harmonic waves, applying a sawtooth voltage is not trivial to excite such a resonance inside the cavity.

4.2.2 Multi-harmonic Bunching Systems

Although the saw-tooth waveform is complicated to generate high voltage amplitudes, the most efficient capture rate is obtained by such an rf voltage. A way of approximating this waveform is to include higher harmonics [27]. A Fourier analysis of a saw-tooth form, as a mathematical representation of these waves, can be written as:

$$
\begin{aligned}
V_{st} &= V_0 \cdot \sum_{n=1} -\frac{2(-1)^n}{n} \sin(n\phi) \quad , \\
&= V_0 \cdot \left(2\sin(\phi) - \sin(2\phi) + \frac{2}{3}\sin(3\phi) - \dots \right) \quad .
\end{aligned}
\tag{4.11}
$$

The system of the Fourier synthesis consists of a combination of one fundamental sine-wave and the superposition of its next higher harmonics. This concept is called "Multi-harmonic bunching - MHB". The MHB system can be designed in two ways; either to overlap the fundamental and its higher harmonics in one bunching cavity or to use independent bunching cavities, which are operated at one specific harmonic frequency each ($f + 2f + 3f + ...$) and separated by drift spaces.

One Gap System With Overlapped Multi-Harmonics

An example of a five-harmonics bunching model following the first option is shown in Figure 4.4. The plots in 4.4a to 4.4e show how an approximate saw-tooth waveform can be obtained by the MHB system, starting with a fundamental frequency at relatively high amplitude (e.g. 2.2 kV) and superposition of its five harmonics (e.g.

0.98, 0.6, 0.4, 0.4 kVs). After an additional drift, the particle distribution, as shown in Figure 4.4e, is transformed into a sharp bunch profile, as plotted in Figure 4.4f. As a result of a good optimization of amplitudes provided for the harmonic voltages and the drift space, the required particle transmission, like $\sim 89.05\%$ accepted within the bars for $\pm 20°$ phase width shown in Figure 4.4f, can be provided for a successful bunching. Concerning these processes shown in Figure 4.4, the superposition of each harmonic provides a supplemental possibility to increase the gain of particle acceptance within a bunch. Goldstein and Laisne mentioned the capture ratios as 65% (fundamental), 81% (fundamental and second harmonic), 86% (fundamental, second, and third harmonics), and 89% (fundamental, second, third, and fourth harmonics), respectively [28]. According to the goal of the application for particle acceleration, such as high current linac applications, the ratios would be sufficient; however, the buncher system requires sophisticated technology. One option could be a combination of two or three $\lambda/4$ resonators, as performed in ATLAS, Argonne National Laboratory [29]. Another technical option for very low-energy beams can be

(a) f   (b) f,2f   (c) f,2f,3f

(d) f,2f,3f,4f   (e) f,2f,3f,4f,5f   (f) f,2f,3f,4f,5f+drift
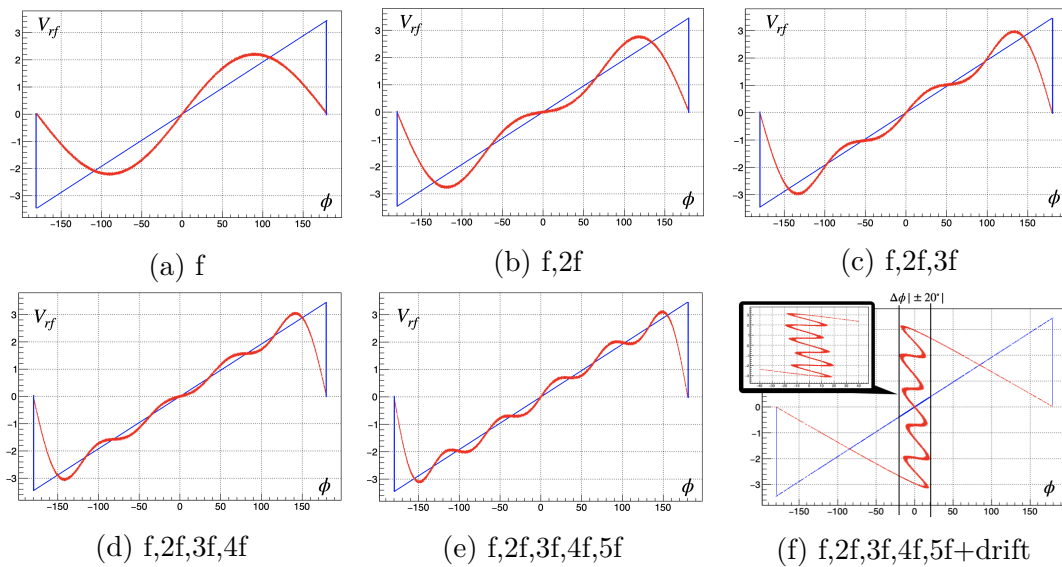
Figure 4.4: The graphs show the fundamental waveform and its successive combination with the first four higher harmonics and the final focus. The blue line corresponds to the ideal linear energy modulation in the range of $\pm 180°$

a buncher formed by a gridded gap as used in ReA3 at ANL [30] [31]; however, this solution is limited to low beam current and very low beam energies. Consequently,

the overlapped multi-harmonic structures require advanced techniques and are more expensive than a simple sinusoidal buncher, like used in FRIB, MSU [12].

One-Harmonic Multi-Drift Buncher

This buncher system applies drifts between harmonic bunchers and offers improved acceptance when compared to a one-gap harmonic system. Every bunching cavity performs at one harmonic frequency $(n \cdot f)$ and is separated from each other by a certain distance. Such a system can improve the linearity of the waveform. A solo buncher with one lower harmonic can evidently be one of the possible structures to fulfill high particle transmission on the beam distribution. In order to support the potential of the one-harmonic buncher system, two numeric examples of the model with the parameters given in Table 4.1 is demonstrated in Figure 4.5.
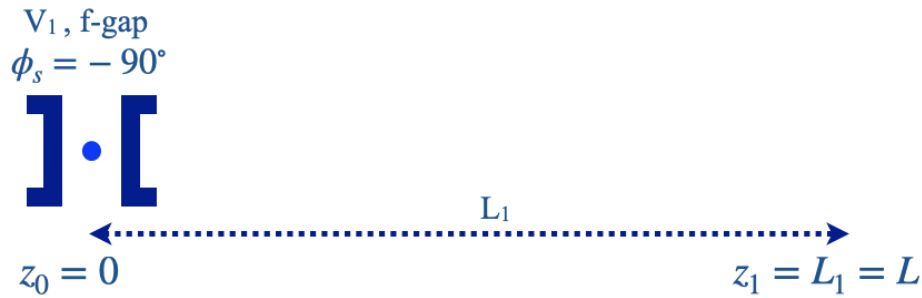
(a) Scheme of one f-buncher with an end drift for longitudinal focus.
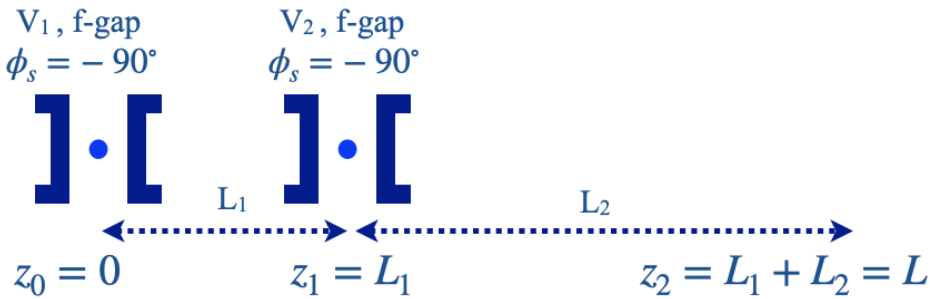
(b) Scheme of two f-bunchers, separeted by a distance, and an additional drift for longitudinal focus.

Figure 4.5: Two examples of double drift buncher models.

According to the parameters given in Table 4.1, the first buncher model is simulated at 54 MHz for a 60 keV proton continuous beam. Since the buncher brings the bunch formation, the beam quality concerning the required ratio of particle capture can

be determined by a chosen/specified phase width according to the next accelerator unit; for example, the bars in Figure 4.6 indicate the selected width of $\pm 10°$ for matching the following section. As a result, one can obtain a capture rate of 46.4% as presented in the example of a simple buncher model.
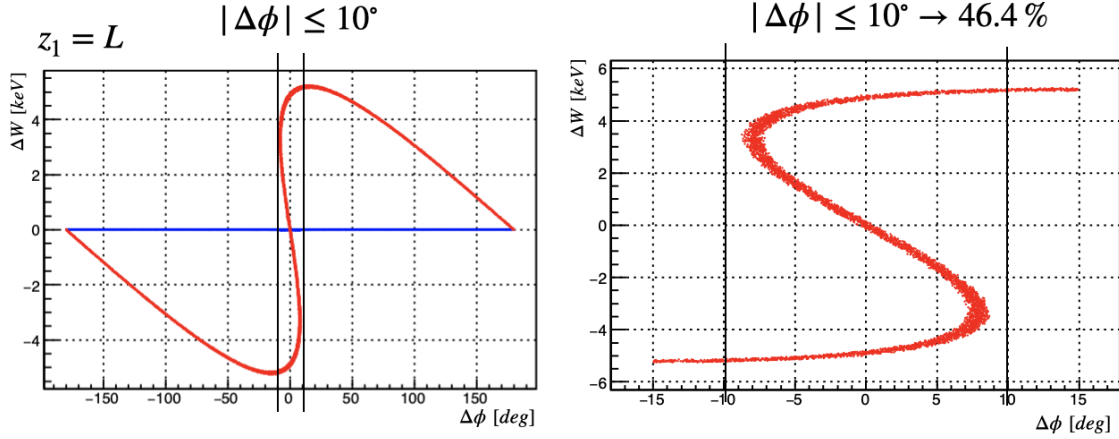
Figure 4.6: Output beam distribution for the one f-buncher model, schematically shown in Figure 4.5a, by given parameters in Table 4.1.

Table 4.1: Parameters of the examples shown in Fig. 4.5.

Parameter	One f-Buncher	Two f-Buncher
Input Energy [keV]	60	60
Frequency (f) [MHz]	54	54
Synchronous Phase	$-90°$	$-90°, +90°$
V_1, V_2 [kV]	5.2	4.1, 4.1
L, L_1, L_2 [m]	0.30	0.30, 0.15, 0.15
Capture Ratio % $_{|\Delta\phi| \leq 10°}$	46.4 %	52.8 %

The second buncher design, schematically shown in Figure 4.5b, consists of two f-bunchers separated a distance to collect more particles into the bucket and an additional drift where the particles travel through the central plane reaching the specified phase width of $\pm 10°$. Figure 4.7 shows the output distribution for a numeric example with the given parameters in Table 4.1.

Although a double-drift buncher system cannot provide high particle transmission, the particle acceptance for the final phase width of $\pm 10°$ can be clearly improved from 46.4% to 52.8%. Concerning the increase in the capture ratio, one can conclude that the one-harmonic double-drift buncher already improves the acceptance by about
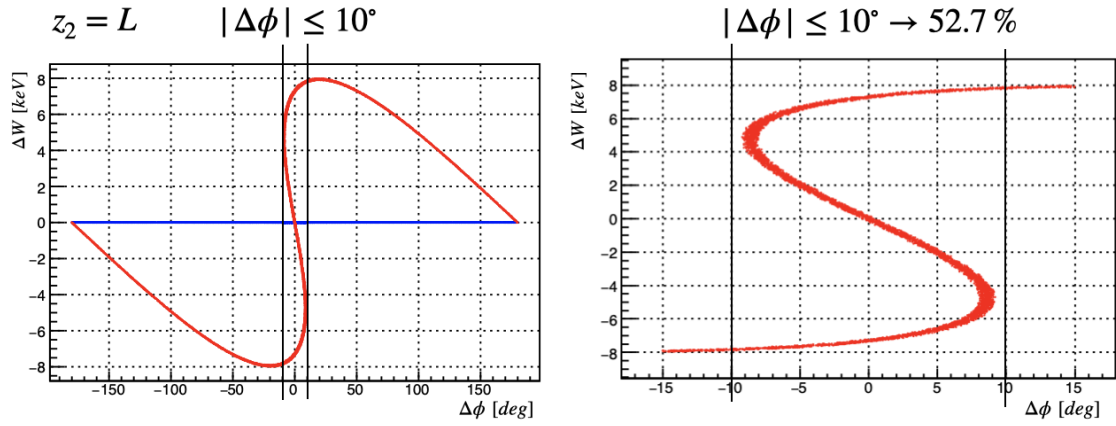
Figure 4.7: Output beam distribution for the double-drift f-buncher model, schematically shown in Figure 4.5b, by given parameters in Table 4.1.

14%. This comparison was made by keeping the phase width at the longitudinal focus at about $\pm 10°$.

In conclusion, the gradual increase of particle acceptance with higher harmonics supports the efficiency of bunch formations. Additionally, inserting drift spaces may improve the bunching efficiency, as demonstrated with two bunchers operated at the fundamental harmonic and separated by a drift. Hence, several results will be presented in the following section, based on the double drift harmonic buncher (DDHB) concept, since it provides significant outcomes for bunching formations by a proper buncher design with a combination of acceptable applied voltages and adequate drift spaces.

4.3 Concept of a Double Drift Harmonic Bunching System

An improved harmonic bunching mechanism is associated with buncher cavities driven at optimized voltages and phases and installed at adequate positions since the energy gain and the beam phase of each particle at the focus point are defined with these two parameters for each cavity, respectively. The main task is to make a successful, robust, affordable design related to that strategy. The proposed concept is based on two buncher cavities separated by a drift from each other, where the bunchers are operated at the first and second harmonics. A final drift distance towards the focus completes that system. It is worth noting that while the calculation of the resulting energy phase distribution of DDHBs by applying Bessel functions as a basis [28] and the graphical method to receive the final distribution [32] have been the ideas implemented in this study, the numerical analysis of the DDHB concept has been explained below.

This design, shown schematically in Figure 4.8, satisfies the envisaged aim of high capture efficiency and a small longitudinal emittance of the formed bunch, as shown in the following. The first buncher in the scheme is operated at the fundamental
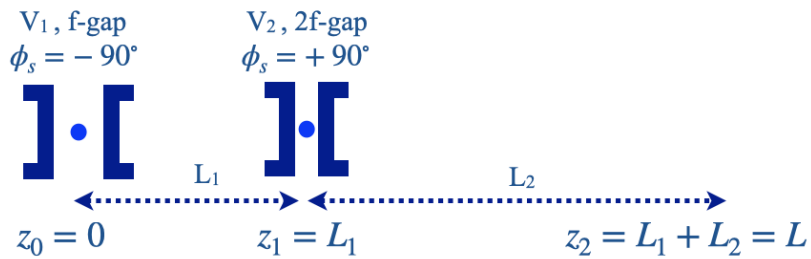
Figure 4.8: Scheme of the DDHB with four specific parameters.

frequency f with $-90°$ synchronous phase and is located at position $z = 0$. It has a gap voltage of V_1. According to the formulae 4.8, an energy modulation for an initially mono-energetic and continuous beam is generated by this sinusoidal signal as written below [13]:

$$\Delta W_i\left(\phi_i^{z_0}\right) = q \cdot V_1 \cdot \sin\left(\phi_i^{z_0}\right) \quad , \tag{4.12}$$

where ϕ_i^0 is the phase of an arbitrary particle i at the buncher with coordinate $z = z_0 = 0$. This initial impact on the energy variation can be seen in Figure 4.9a.

(a) f-wave

(b) f+L_1

(c) f+L_1+2f

(d) f+L_1+2f+L_2

(e) $|\Delta\phi| = \pm 10$
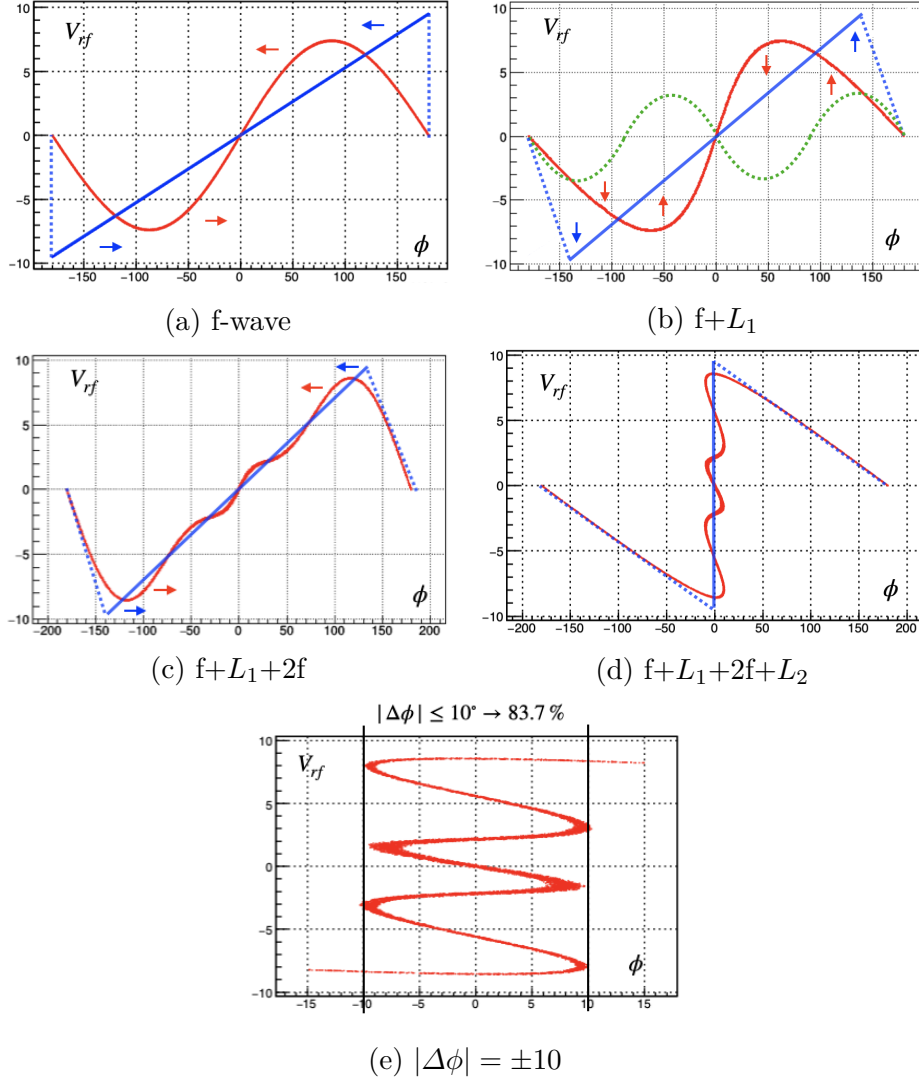
Figure 4.9: The graphs indicate the mechanism of the DDHB concept. For this example, $\pm 10°$ phase width turns out $\sim \%83.7$ particle capture efficiency.

The drift distance L_1 between the buncher cavities contributes to the shift of the particle phase ϕ_i due to the energy modulation of the beam, as shown in Figure 4.9b, and the shifted beam distribution in the phase plane can be written by using Equation 4.9 as:

$$\Delta\phi_i\left(z_1\right) = -\frac{\omega \, L_1}{\beta_s^3 \gamma_s^2 \, c} \cdot \frac{\Delta W_i\left(\phi_i^{z_0}\right)}{W_s} \, . \tag{4.13}$$

where the relative phase is represented by $\Delta\phi_i^1 = \phi_i^{z_1} - \phi_i^0$. The second buncher at the second harmonic $2f$ with a synchronous phase of $+90°$ affects the energy distribution, which is added to the result of the first buncher:

$$\Delta W_i\left(\phi_i^{z_1}\right) = \Delta W_i\left(\phi_i^{z_0}\right) - q \cdot V_2 \cdot \sin\left(2\phi_i^{z_1}\right) \tag{4.14}$$

where V_2 is the applied voltage of this buncher cavity. The effect of the two bunchers combined with the distinct separation L_1 is shown in Figure 4.9c. The plot indicates that by the addition of the second harmonic buncher, more particles are pushed into the desired phase width. The second drift L_2 corresponds to a beam focus at $z = L_1 + L_2$. This last step gives an additional phase shift of the particles against the synchronous particle. This resulting distribution is shown by Figure 4.9d.

$$\Delta\phi_i\left(z_2\right) = \Delta\phi_i(z_1) - \frac{\omega \, L_2}{\beta_s^3\gamma_s^2 \, c} \cdot \frac{\Delta W_i\left(\phi_i(z_1)\right)}{W_s} \; . \tag{4.15}$$

Consequently, the concept relies on four parameters: applied voltages in the buncher cavities V_1, V_2, and the lengths of the drifts L_1 and L_2. The synchronous phases $\phi_1 = -90°$ and $\phi_2 = 90°$ have to be kept constant and refer to the synchronous particle.

4.3.1 Dependence Of the Four Parameters

Various simulations using a 60 keV proton beam at the fundamental frequency of 54 MHz with an assumed small value of the energy spread $\frac{\Delta W}{W} \leq 10^{-4}$, have been investigated as parameters listed in Table 4.2. In the designs, the first drift space

Table 4.2: Summary of the results from Figure 4.11.

Focal Width	L_1/L_2; $L_1 = 84.35$ mm	V_1 [kV]	V_1/ V_2	Capt. Rate %	Capt. Rate % $_{\vert\Delta\phi_f\vert \leq 20°}$
$\vert\Delta\phi_f\vert \leq 2°$	0.19	2.20	2.29	65.04 %	77.01 %
$\vert\Delta\phi_f\vert \leq 3°$	0.22	2.57	2.07	70.82 %	79.45 %
$\vert\Delta\phi_f\vert \leq 5°$	0.24	2.90	1.93	76.33 %	81.24 %
$\vert\Delta\phi_f\vert \leq 10°$	0.29	3.70	1.57	83.70 %	85.64 %
$\vert\Delta\phi_f\vert \leq 20°$	0.35	4.60	1.31	89.06 %	89.06 %

between the two bunchers is kept constant, and by altering the applied voltages on the bunchers, the final drift distance is adjusted in every design. When the ratio of L_1 and L_2 becomes large, the best possible phase width at the exit should also be large to achieve the output beam with the required features. The meaning of a large ratio of L_1 and L_2 is to get L_2 shorter, and the structure becomes more compact. On the contrary, a small ratio of L_1 and L_2 makes the width very narrow, but with less percentage of particle capture, as seen in the outcomes in Table 4.2. According to the optimum cases for the potential small phase widths and the possible highest particle transmissions, respectively, the output beam distributions are shown in Figure 4.11. Moreover, the graph in Figure 4.10 shows the difference in the acceptance rate by changing the ratio of L_1 and L_2 in these five cases. For each L_1/L_2-ratio, the range of minimum phase widths in the focal plane and their acceptance values are limited by the results labeled in blue and green bullets.
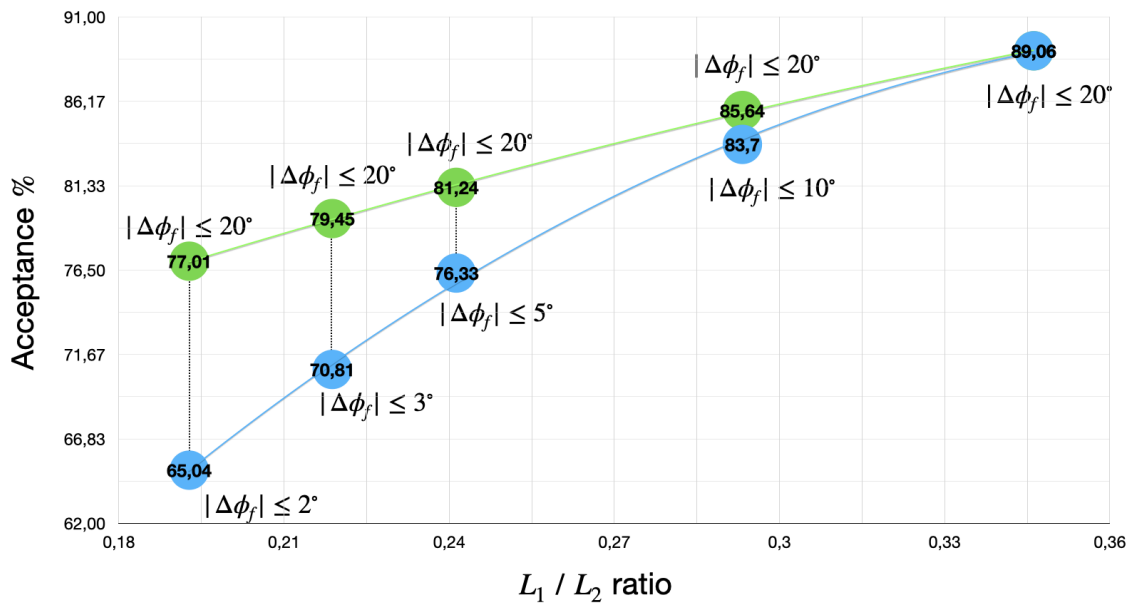
Figure 4.10: $|\Delta\phi_f|$ vs. L_1/L_2 ratio.

Since the goal of the development of the DDHB concept [33] is to use the system in the injectors into RFQ, cyclotron, or DTL, these investigations serve this aim with great potential in practice. While the cyclotron injections require small phase widths to eliminate debunching of the beam at the exit of the cyclotrons, larger phase widths are convenient for RFQ injections due to the need for possible highest

particle transmissions. Additionally, the DTL injections can have values in between based on the required design properties of the DTL.
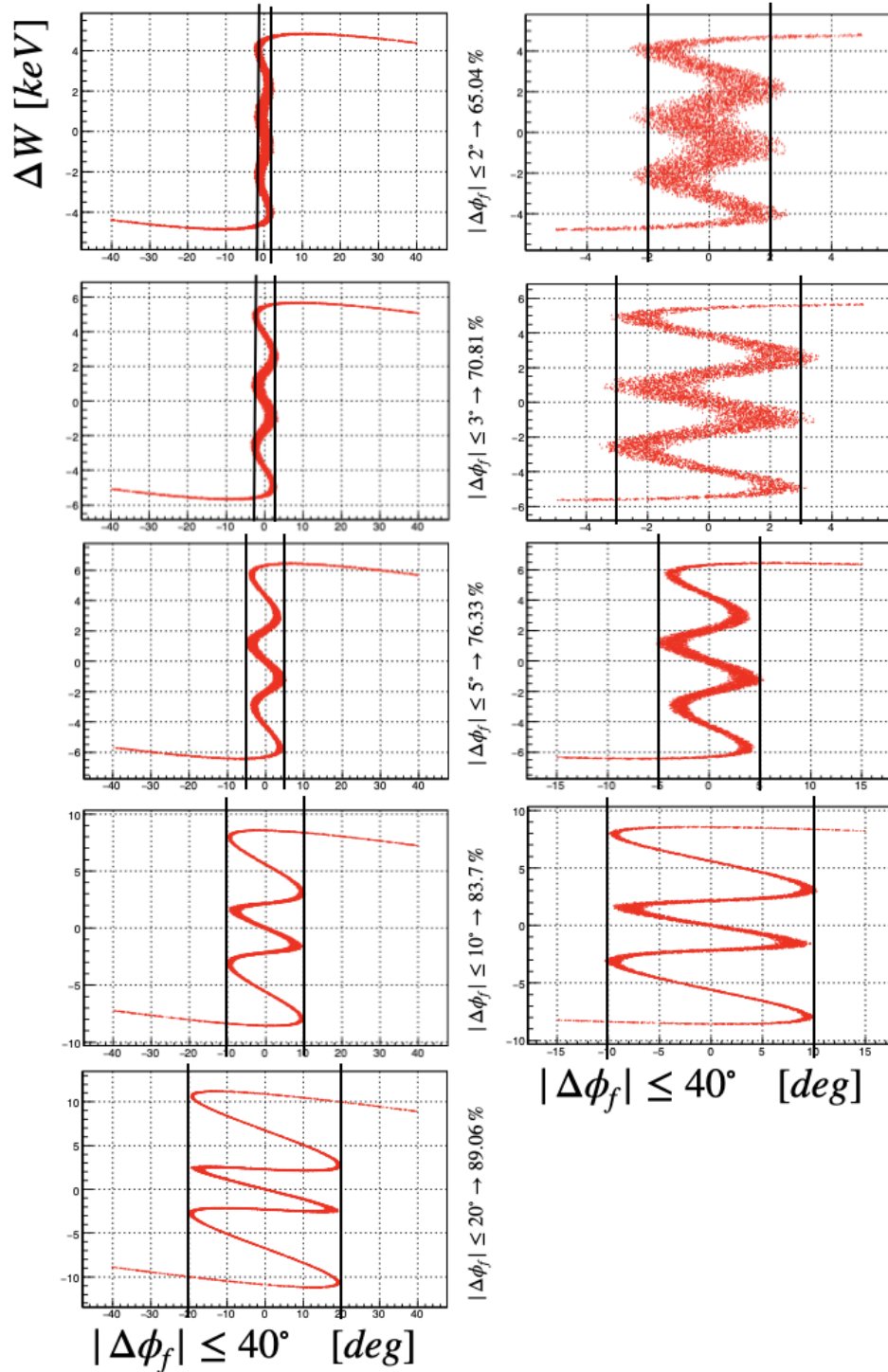
Figure 4.11: The distribution plots show the different designs based on $|\Delta\phi|$.

In addition, the DDHB concept allows fulfilling a distribution like the one with three harmonics, as seen by comparing Figures 4.9c and 4.4c. Concerning this similarity, another simulation with the same beam properties mentioned above (also listed in the parameters in Table 4.3) has been done, and the behaviors of the beam in each are demonstrated in Figure 4.12.

(a) The DDHB concept.

(b) One gap with three harmonics.
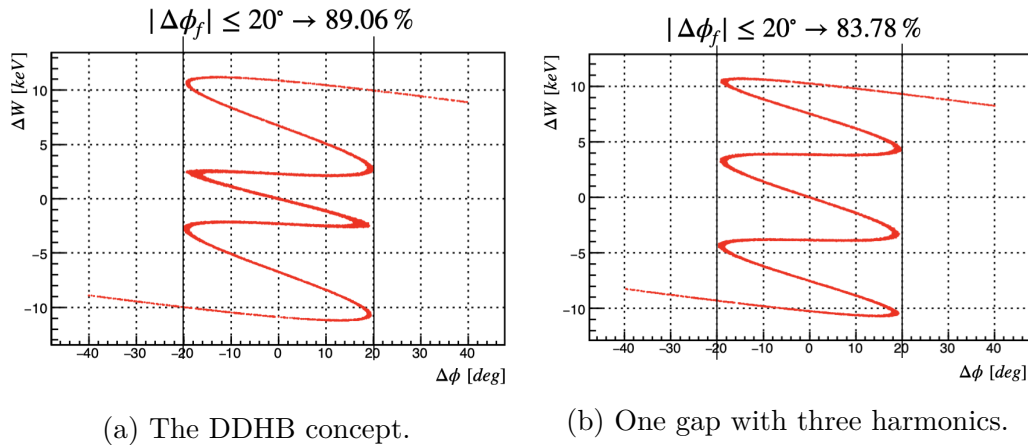
Figure 4.12: The comparison of the designs of the DDHB concept and one gap-multi-harmonic system.

Table 4.3: Parameters of the examples shown in Figure 4.12.

Parameter	DDHB $(f - 2f)$	Triple Harmonics $(f - 2f - 3f)$
Input Energy [keV]	60	60
Frequency [MHz]	54, 108	54, 108, 162
Beam Current [mA]	0	0
Synchronous Phase	$-90°, +90°$	$-90°, +90°, -90°$
L_1, L_2 [mm]	84.35, 243.8	0, 273
V_1, V_2, V_3 [kV]	4.60, 3.51	7.8, 3.4, 2.5
Capture Rate % $_{\Delta\phi| \pm 20°|}$	89.06 %	83.78 %

One can see that the DDHB with focus generates a similar particle distribution of a 3-harmonic buncher. Even though there is a similarity between them, the efficiency of the output distribution for the DDHB with respect to the percentage of particle acceptance is about 5% more than the third harmonic design. In addition to that, the design with the triple harmonic requires more power consumption than the other. In conclusion, the DDHB has advantages concerning consuming power, particle acceptance, and investment costs.

Chapter 5

Simulations and Optimizations of DDHB Design Cases

5.1 Optimization of a Design Based on Zero-Current Input Beam

In various applications, one of the main factors for the output beam quality depends on a chosen phase width at the exit of the DDHB system. On the one hand, the phase width is adjustable by the technique of the bunching concept, but on the other hand, an unavoidable remaining thickness is caused by a d.c. beam extraction from an ion source. Even if the final distribution looks perfectly saw-tooth-like, an unavoidable half-thickness of the beam distribution occurs due to technological constraints. Therefore, in both designs, the simulations are accomplished by using the identical 60 keV, 0 mA proton beam at the fundamental frequency of 54 MHz and assuming a small value of the energy spread, $\frac{\Delta W}{W} \leq 10^{-3}$ to keep away the effect of the ion source. In both designs, the input beam emittance in transverse is around 0.268 $mm \cdot mrad$ and its longitudinal emittance is around 0.131 $keV \cdot ns$ (2.542 $keV \cdot deg$).

The first example in Figure 5.1a indicates an acceptable output beam distribution for continuing the bunching process into an RFQ. The parameter list of the belonging design is given in Table 5.1, and the resultant beam properties as 89.06% particle acceptance within ±20° phase width and $\epsilon_{l,rms} = 3.459\ keV \cdot ns$ output emittance. While these exit features provide a bigger modulation inside the RFQ due to injecting

Table 5.1: Design parameters of two examples shown in Figure 5.1.

Parameter	Design 1: $L_1/L_2 \uparrow$ (High Acceptance)	Design 2: $L_1/L_2 \downarrow$ (Small Phase Width)
Input Energy [keV]	60	60
Frequency $(f - 2f)$ [MHz]	54, 108	54, 108
Beam Current [mA]	0	0
Synchronous Phase	$-90°, +90°$	$-90°, +90°$
L_1, L_2 [mm]	84.4, **243.8**	84.4, **385.8**
V_1, V_2 [kV]	4.60, 3.51	2.57, 1.24
Capture % $_{|\Delta\phi| \leq 3°}$	8.96	**70.81**
Capture % $_{|\Delta\phi| \leq 20°}$	**89.06**	79.45
$\varepsilon_{x,n,\mathrm{rms}}$ [mm.mrad]	0.282 $_{|\Delta\phi_f| \leq 20°}$	0.279 $_{|\Delta\phi_f| \leq 20°}$
$\varepsilon_{l,\mathrm{rms}}$ [keV.deg]	67.23 $_{|\Delta\phi_f| \leq 20°}$	11.25 $_{|\Delta\phi| \leq 3°}$
$\varepsilon_{l,\mathrm{rms}}$ [keV.ns]	3.459 $_{|\Delta\phi_f| \leq 20°}$	0.579 $_{|\Delta\phi| \leq 3°}$

a bunched beam in $\pm 20°$, the length of the RFQ might become shorter due to immediately ramping the acceleration up, and no need to bunch section. As a result of these exit features, the DDHB concept demonstrates its potential for special applications as an injector into an RFQ.

(a) Design 1.

(b) Design 2.
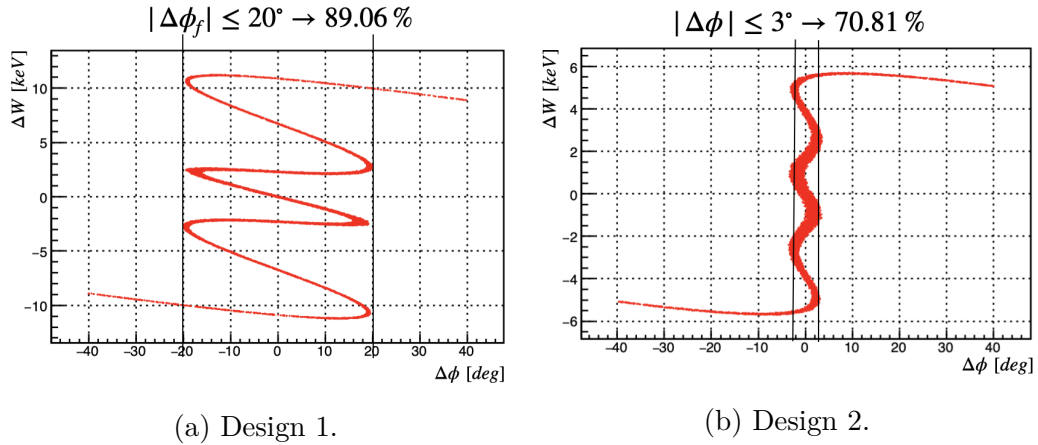
Figure 5.1: The graphs show the output of longitudinal phase spaces for a 60 keV, 0 mA proton beam with the energy spread of $\frac{\Delta W}{W} \leq 10^{-3}$ fulfilling the different aims for various applications of the subsequent accelerator units.

The second example in Figure 5.1b, concerning the possible narrow phase width with a potential high capture rate, is designed with the parameters listed in Table 5.1. In order to obtain smaller longitudinal emittance, the applied voltage must be smaller to get rid of saturating/spreading particles in the energy-phase plane. With

less phase deviation (degree of filamentation), one can achieve a successful smooth bunch formation with a tiny phase width of $\pm 3°$ and 70.81% capture rate, and the longitudinal emittance of $\epsilon_{l,rms} = 0.579 \ keV \cdot ns$. In order to have a meaningful comparison, the capture rate for the same phase width of $\pm 20°$, as used in the first example, is 79.45%. The narrow phase width can be provided by lengthening L_2, in other words, decreasing the ratio of L_1/L_2. While increasing this ratio, as in the first example, the saw-tooth form is centralized with large deviations, and particle transmission can be higher within a larger phase range. Otherwise, as in the second example, the final distribution evolves smoothly with good acceptance. This small phase window is required for acceleration in cyclotrons due to their missing longitudinal beam focusing. Each particle follows its path due to yielding energy itself; hence, beam distribution at the exit might be debunched transversally due to their energy deviation. Concerning these effects, the beam has to be bunched in a very narrow phase width, like $\pm 3°$, as in the example.

Consequently, the degree of filamentation in the beam distribution represents an indicator of the output beam quality; hence, the ratio of L_1/L_2. In one case, a high rate of L_1/L_2 develops a small phase width in the final beam distribution but with less particle acceptance. In another, a large phase width and high capture rate can be achieved by a smaller ratio of L_1/L_2.

Figure 5.2: The plot shows the transverse beam envelope of the *Design* 2 by using the BCDC code.

In addition to the longitudinal beam dynamics, the transversal perspective is also significant for a design. Figure 5.2 shows the transversal beam envelope of the design with a small phase width, as mentioned above. The results on the plot were provided by an input beam radius of about ± 7 mm. Two quadrupole triplets provide the

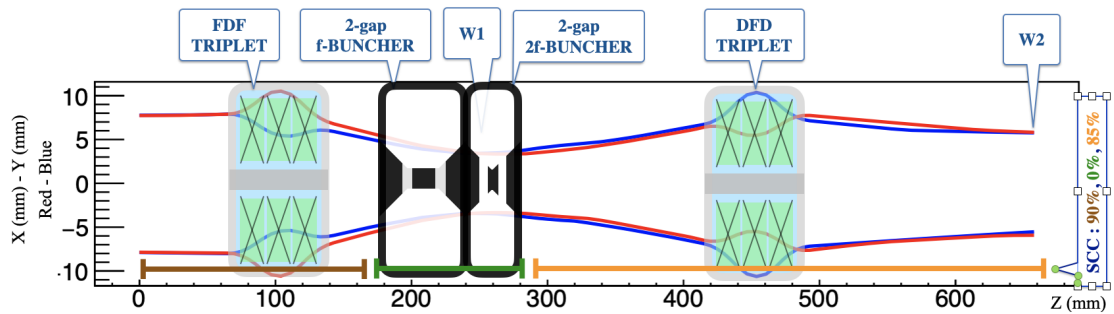transverse focusing. Since the relation between the diameter of the accelerating gaps and the gap length determines the behavior of the electric fields inside cavities [34], the waist position W_1 must be located at the second buncher not to lose particles by hitting the beam pipe wall, and this can be obtained by adjusting the strengths of these quadrupoles. Besides using permanent magnets for a very compact layout, the total length of the structure was achieved in less than 0.7 m. As a main outcome, a beam focus in all three emittance planes was fulfilled at position W2.

5.2 Optimization of a Design Including Beam Current

One of the goals in the study of this thesis is to reach a design for high-current machines. Therefore, in this section, the same example in the previous section, the *Design* 2, would be the reference design labeled *A*, as shown in Figure 5.3, while investigating the effect of space charge concerning the NNB and the SCC concepts. In all optimization steps towards current for this purpose, a 60 keV proton beam was used with 54 MHz operating frequency, and the beam current was increased up to 3 mA by keeping/observing the phase width at the same range of $\pm 10°$. Since this section explains the behavior of designing the DDHB concept with the beam current, all results are achieved under real situations by activating the concept of NNB in all simulations. In addition to including the NNB feature, the SCC routine has also been included in the front and end regions of the buncher system with 90% and 70%. It means the beam current has been fully contained only inside the bunchers.

Table 5.2: Parameters of the optimization steps, *B*1 to *B*6 shown in Figure 5.3, for the impact of the space charge. (Currents with partial space charge compensation).

Designs	L_1/L_2	L_1 [mm]	L_2 [mm]	$V_1/\ V_2$	V_1 [kV]	V_2 [kV]
A (0 mA)	0.219	84.35	385.8	2.07	2.57	1.24
B1 (3 mA)	0.219	84.35	385.8	2.07	2.57	1.24
B2 (3 mA)	0.225	84.35	373.8	1.97	2.84	1.44
B3 (3 mA)	0.233	84.35	361.8	1.97	2.94	1.49
B4 (3 mA)	0.233	84.35	361.8	1.92	2.94	1.53
B5 (3 mA)	0.236	78.35	357.8	1.92	2.94	1.53
B6 (3 mA)	0.236	78.35	357.8	2.01	2.94	1.46

In the presence of 3 mA beam current, the output distribution loses the focus

due to the repelling force of space charge as seen in Figure 5.3 labeled $B1$, when compared to the 0 mA optimisation in Figure 5.3 labeled A. In order to bring it in focus properly, a greater drift length is not sufficient for a desired output beam; therefore, the parameters V_1 and V_2 have been increased. By adjusting an adequate combination of these three parameters L_2, V_1, V_2 as listed in Table 5.2, the focus on the output distribution can be obtained as seen in Figure 5.3 labeled $B2$. A consequence of this adjustment is a widened phase width of $\pm 5°$ instead of $\pm 3°$.
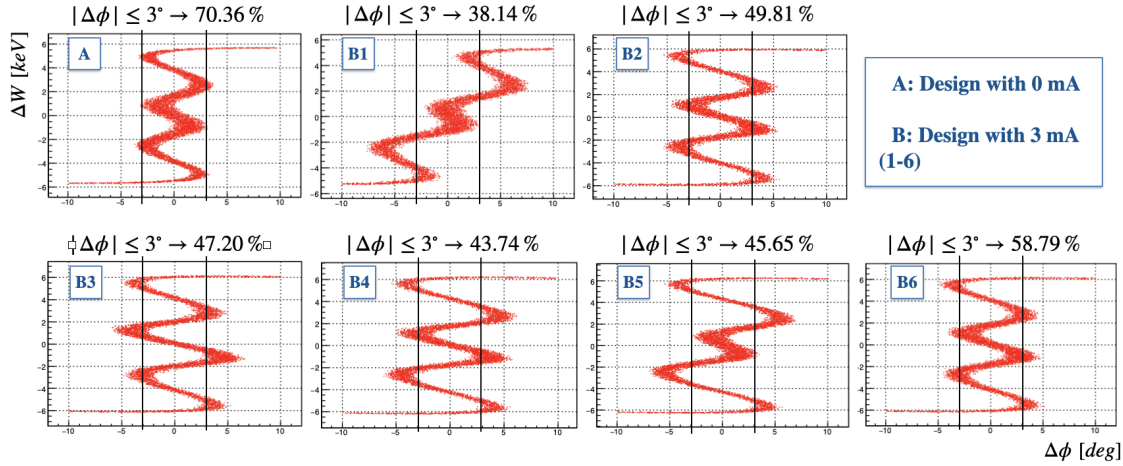
Figure 5.3: The first plot labeled A is the output distribution of the reference design with 0 mA. The other cluster plots from $B1$ to $B6$ are optimized for 3 mA beam current. The design parameters are listed as in Table 5.2.

A higher voltage V_1 is applied in the design in Figure 5.3 labeled $B3$, and V_2 is increased according to the ratio of V_1/V_2 as seen in Table 5.2. Due to the rise of particle acceleration, the last drift has been decreased up to the focal point. Regarding the output distribution, one can interpret that V_2 becomes weak, and one should increase a few percent of its value as can be seen in Figure 5.3 labeled $B4$.

The attempts of the plots labeled $B3$ and $B4$ in Figure 5.3 explain that increasing the applied voltages at the buncher cavities can partially avoid space charge force from the beam current. However, the change in the length between the two cavities can provide a narrower phase width of $\pm 3°$, the previous designs of $\pm 5°$. Concerning this, the drift between two bunchers must decrease as the design shown in Figure 5.3 labeled $B5$. By adjusting the other parameters V_1, V_2, L_2 according to the smaller length L_1, the output distribution in the range of $\pm 5°$ phase width can be achieved

with acceptable capture rates as listed in Table 5.3.

Table 5.3: Capture Rates for each designs as shown Figure 5.3.

Phase Width $\Delta\phi_f$ [°] Design	Capture Rate %					
	$\pm20°$	$\pm10°$	$\pm5°$	$\pm3°$	$\pm2.5°$	$\pm2°$
A (0 mA)	79.45	76.01	73.62	70.81	63.85	52.97
B1 (3 mA)	77.72	73.70	54.58	38.14	32.99	27.91
B2 (3 mA)	80.66	77.82	75.35	51.22	41.08	31.40
B3 (3 mA)	80.94	78.07	74.12	48.23	37.59	28.47
B4 (3 mA)	81.21	78.54	73.12	45.61	36.26	27.40
B5 (3 mA)	81.09	78.47	68.56	45.61	40.45	34.66
B6 (3 mA)	80.44	77.50	75.47	58.79	47.90	36.70

In brief, a design is performed by optimizing the four parameters concerning all these consequences. One consequence is that the ratio of L_1/L_2 is the significant determent for the capture rate of a narrow phase width. Another outcome is that the space charge action reduces the energy spread of the beam distribution by counteracting, as a similar behavior of the bunching process. In the presence of the space charge, the total length of L_1 and L_2 should be small enough to keep the energy spread the same.

5.3 Various Designs for Different Beam Energies and Beam Current Levels

In practice, the geometric feasibility of RF buncher cavities must be considered while developing designs of the DDHB concept. Since the interesting energy range for designs located between the ion source and the accelerating unit, is roughly from 25 keV up to 100 keV (technically much easier than above 150 keV), the parameter scope with a set of $\beta\lambda/2$ period lengths is determined by the chosen fundamental operating frequencies for these energy ranges, as shown in Table 5.4.

Designs with $\beta\lambda/2$ values smaller than 30 mm at the fundamental frequency are impractical due to using multi-gap cavities in the buncher system. In this regard, the

Table 5.4: Range of parameters for geometric feasibility of RF buncher cavities in different applications.

Frequency [MHz] [keV] Input Energy	$\beta\lambda/2$ [mm]		
	27	54	108
100	81.05	**40.52**	20.26
60	62.78	**31.39**	15.70

parameters on the right of the table concerning the fundamental frequencies are not realistic. As an alternative to realizing short period lengths, either $3\beta\lambda/2$ designs or one gap cavity designs might be an option.
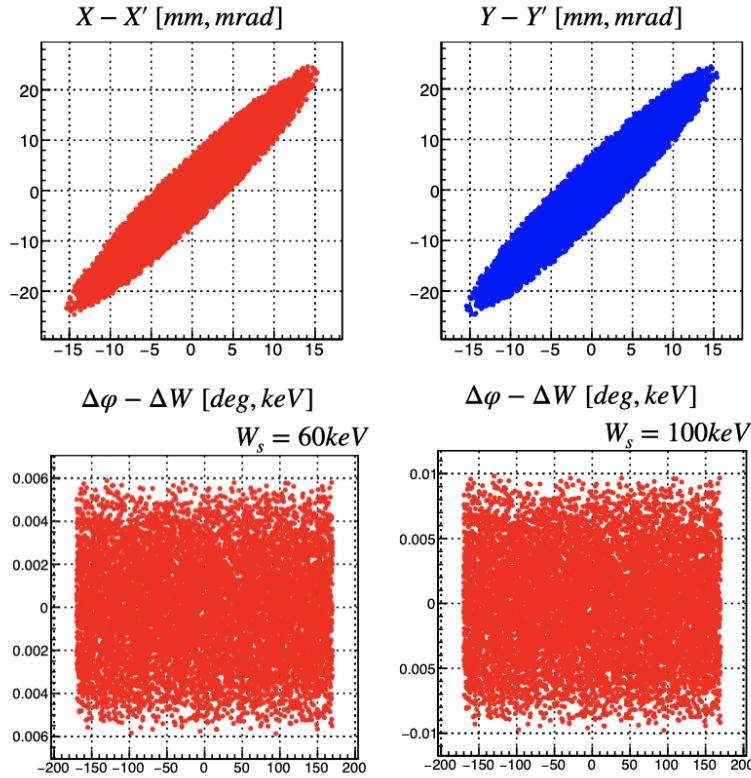

Figure 5.4: The plots show the input distributions in all phase space planes.

In this section, the simulations have been performed with different input beam currents by two sets of parameters, shown in bold font in Table 5.4. The one with a 100 keV proton beam at 54 MHz fundamental frequency was selected for the high

energy low and high current applications for the following units, like cyclotron (low current) or DTL, while the one with a 60 keV proton beam at the same frequency is for medium energy and medium current applications, like injecting into an RFQ. All

Table 5.5: The emittance values of the input beam distributions for 60 and 100 keV proton beams.

Input Emittance	Distribution for 60 keV	Distribution for 100 keV
$\varepsilon_{x,n,\mathrm{rms}}$ [mm·mrad]	0.22	0.28
$\varepsilon_{y,n,\mathrm{rms}}$ [mm·mrad]	0.23	0.29
$\varepsilon_{l,\mathrm{rms}}$ [keV·deg]	0.240	0.401
$\varepsilon_{l,\mathrm{rms}}$ [keV·ns]	0.0123	0.0206

designs are based on similar proton beam distributions with a small but technically reasonable value of the energy spread of $\Delta W/W_{in} \sim 10^{-4}$, as shown in Figure 5.4. The related normalized rms emittance values are written in Table 5.5.
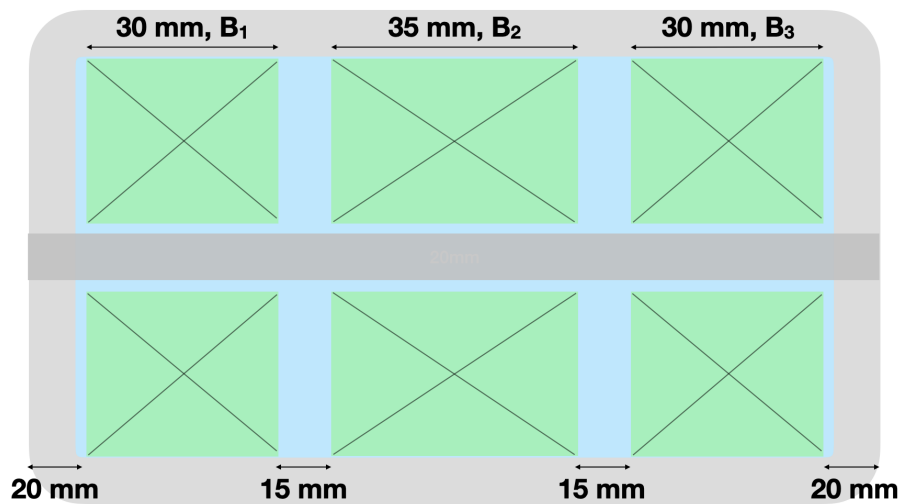

Figure 5.5: The layout of the set of three quadrupole magnets.

In all simulations, the size of the magnets is kept fixed as shown in Figure 5.5, and the strengths of these three series of quadrupoles (B_1, B_2, B_3) are adjusted to the transversal beam distributions for the designs. In addition, the drawing in Figure 5.6 gives an impression on the realistic geometry of a DDHB setup.
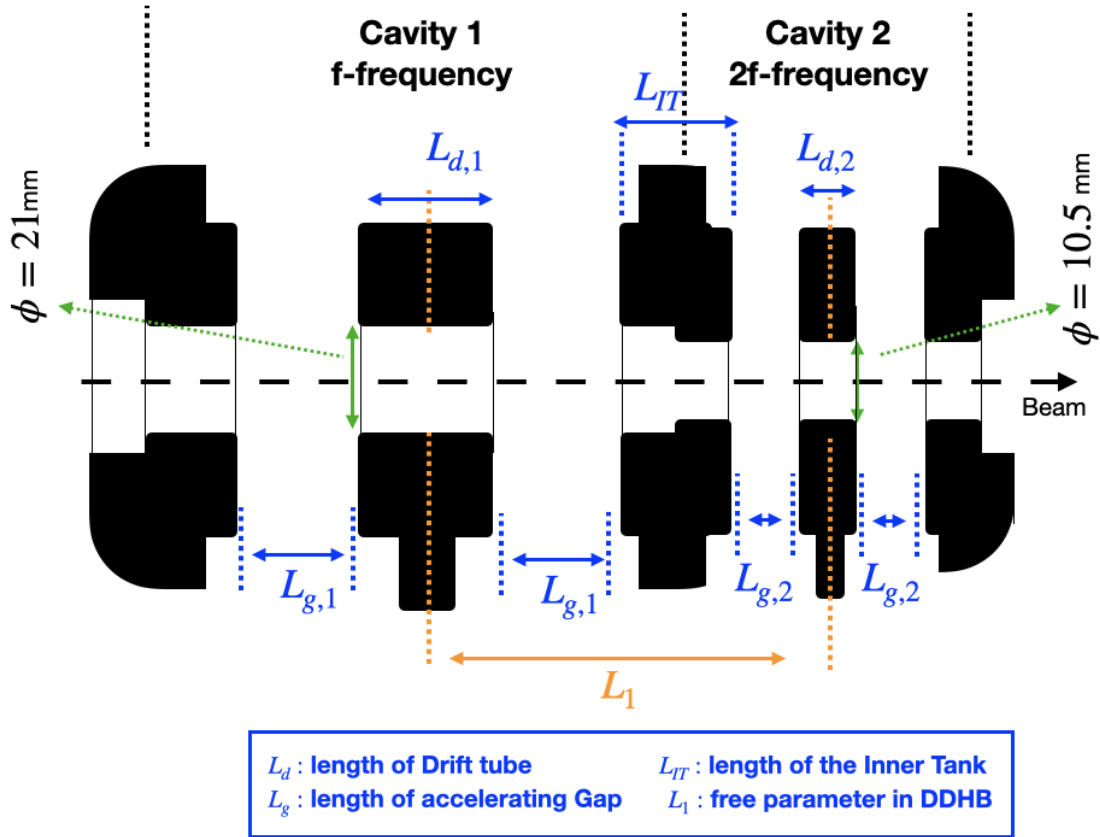
Figure 5.6: The drawing of the buncher cavities in the DDHB concept by attaching f- and 2f-cavities with a free parameter L_1.

5.3.1 Low Current (1 mA) 100 keV Proton Beam Applications

In the low current high energy case, one example of a 100 keV, 1mA proton beam was performed with parameters listed in Table 5.6 and seen its schematic with its envelope traces in Figure 5.7. The interesting positions concerning the transversal and longitudinal beam dynamics are labeled with numbers in the figure. Such an application aims to obtain a focused beam in all planes with an adequate transmission rate. Concerning a simple and cost-efficient bunching system, the indicated example in this section fits an application for a cyclotron injection. Although the total array length of about 3 m is quite a distance, the end free space of about 2 m is needed for the longitudinal beam focus and the required free distance in the cyclotron entrance before the acceleration point.

The concept of a cyclotron utilizes a magnetic field to drive charged particles into

Table 5.6: Design parameters and its results.

Design Parameter	Value	Output Paremeter	Result
Input Energy [keV]	100	$\varepsilon_{x,n,\mathrm{rms}}$ [mm·mrad] $_{|\Delta\phi|\,\leq\,5°}$	0.290
Frequency $(f-2f)$ [MHz]	54, 108	$\varepsilon_{y,n,\mathrm{rms}}$ [mm·mrad] $_{|\Delta\phi|\,\leq\,5°}$	0.296
Beam Current [mA]	1 mA	$\varepsilon_{l,\mathrm{rms}}$ [keV·deg] $_{|\Delta\phi|\,\leq\,5°}$	4.837
Synchronous Phase	$-90°$, $+90°$	$\varepsilon_{l,\mathrm{rms}}$ [keV·ns] $_{|\Delta\phi|\,\leq\,5°}$	0.249
SCC %	90, 0, 85	Capture % $_{|\Delta\phi_f|\,\leq\,20°}$	76.66
L_1,L_2 [mm]	260.2, 2295	Capture % $_{|\Delta\phi_f|\,\leq\,10°}$	72.21
V_1,V_2 [kV]	0.98, 0.35	Capture % $_{|\Delta\phi_f|\,\leq\,5°}$	69.25
		Capture % $_{|\Delta\phi_f|\,\leq\,4°}$	68.26
		Capture % $_{|\Delta\phi_f|\,\leq\,3°}$	58.16
		Capture % $_{|\Delta\phi_f|\,\leq\,2°}$	35.12

circular orbits with an angular frequency ω. The acceleration in each revolution is provided by the acceleration gaps in the structure where the RF voltage is applied. When the circulating particles match with the resonance frequency in the system, the path of the particles becomes spiral due to acceleration. Due to the cyclotron resonance equation $\omega = \frac{e \cdot B}{m}$, the longitudinal focusing feature is missing in the cyclotrons' process since the formula is only dependent on the particle's mass, independent of its energy. Since the acceleration of the particle distribution creates an energy deviation, the phase width of the injecting beam into the cyclotron must be narrow to eliminate transversal defocusing. As a competitor of the conventional ways, this design with the concept of DDHB can provide such a bunch width for a cyclotron injection, where one potential use of the design idea is to be partially embedded into the cyclotron yoke.

Three triplets of a series of three compact permanent magnets, as illustrated in Figure 5.5, are the essential elements for the transversal focus. The first set of quadrupole magnets (10, -16.35, 10 [T/m]) is located at a distance of 450 mm length before the bunching system concerning gentle focusing before starting the bunching process. The second (-11.2, 18.1, -11.2 [T/m]) and third (13.6, -21.5, 13.6 [T/m]) triplets are inserted to keep the transversal dynamics stable.

Figure 5.8 demonstrates the particle distributions in the $X - Z$ plane along the structure associated with the numbers in the figure above, and Figure 5.9 presents the longitudinal phase space clusters of these distributions at the same positions. Since the interested phase width in this example is $\pm 5°$, the sixth plot in the figure

Figure 5.7: Example of one DDHB design simulated with the BCDC code. The plot shows the transverse beam envelope for a 100 keV, 1 mA proton beam and the transversal phase space distributions in the XX'-plane with the indicated positions.
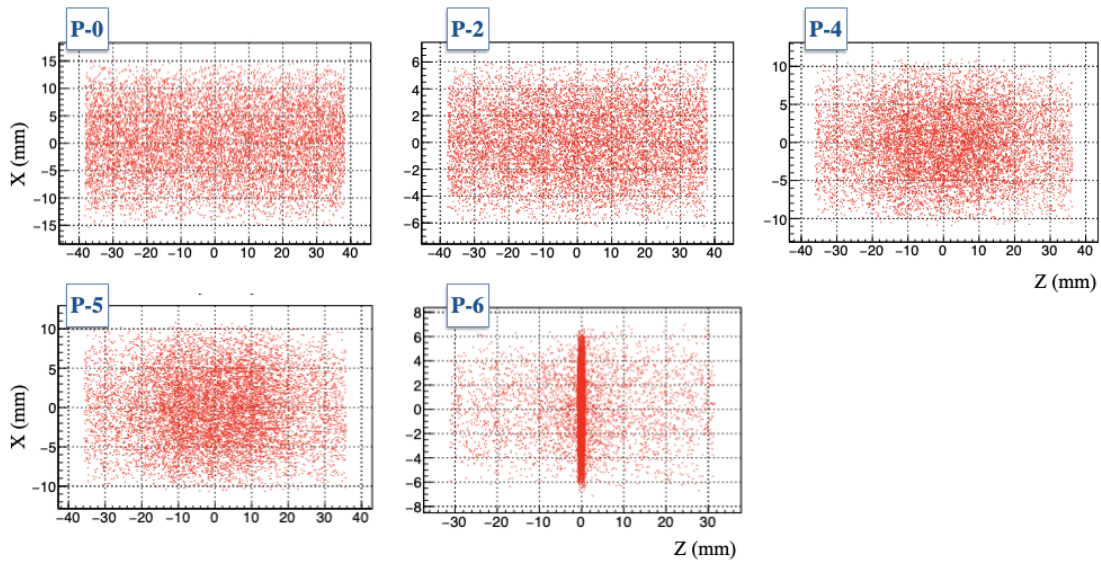
Figure 5.8: The particle distributions in $X - Z$ plane with according positions shown in Figure 5.7.

illustrates what kind of a bunched beam would be injected into the cyclotron. The outcome of the setup is a very sharp longitudinal beam focus with very small emittance and a fair capture rate of around 70%. The design with the concept of
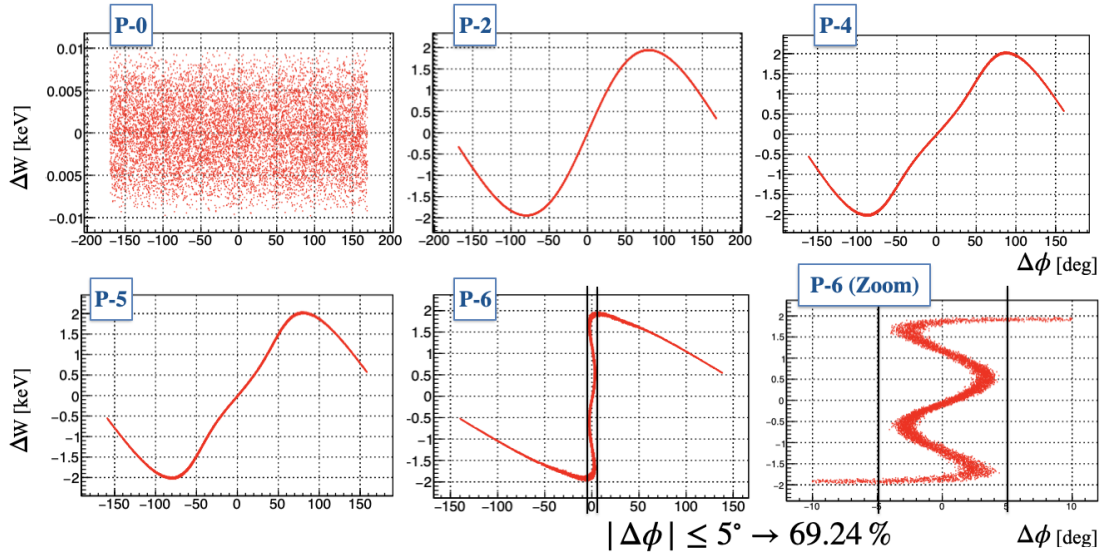
Figure 5.9: The longitudinal relative phase space plots.

DDHB provides a consistent particle transmission within the acceptance range of $\pm 4°$ to $\pm 10°$. Moreover, the small energy spread of ± 2 kev (corresponding to 2%) is fulfilled to keep transversally focused during the acceleration inside the cyclotron.

5.3.2 Medium Current (10 mA) 60 keV Proton Beam Applications

In the medium current medium energy applications, one simulation of a 60 keV, 10 mA proton beam, based on the example presented in the conference of LINAC22 [35], was performed with parameters listed in Table 5.7 and the layout with the corresponding envelope traces are shown in Figure 5.10. The four critical positions w.r.t the transversal and longitudinal beam dynamics are highlighted with numbers in the figure. The operation of a beam with medium current and medium energy aims to get a pre-bunched beam in a short distance by a simple bunching system. While one goal is to get a compact design, another is to achieve a small phase width on the output distribution with a considerable particle transmission, provided by the DDHB concept for medium current and medium energy applications. The example shown in this section fulfills the short-length structure by achieving these required beam properties at the injection point into the following unit, like an RFQ.
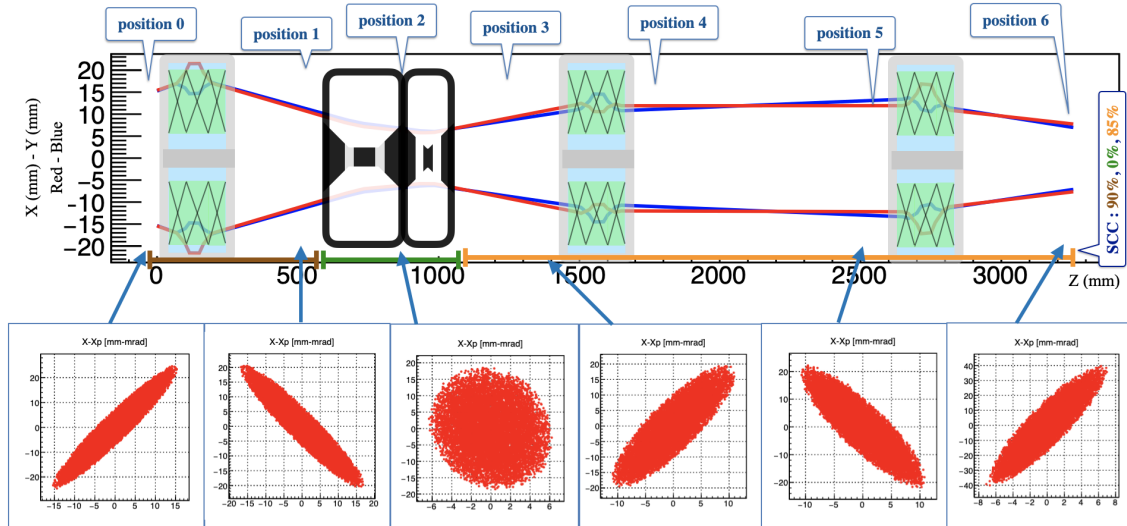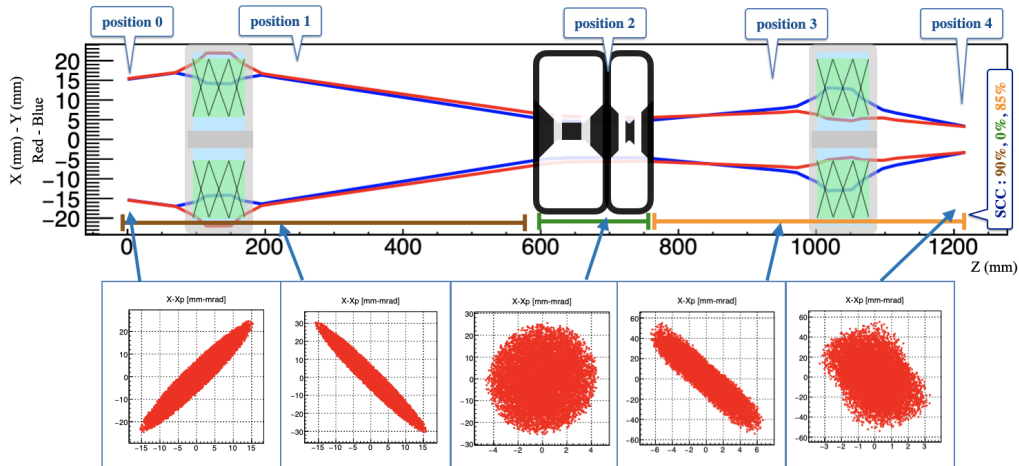

Figure 5.10: Example of one DDHB design simulated with the BCDC code. The plot shows the transverse beam envelope for a 60 keV, 10 mA proton beam and the transversal phase space distributions in the XX'-plane with the indicated positions.

RFQs start with the bunching process at $-90°$ synchronous phase, and about half of the cell is used for this operation. Since the moderated bunching system of DDHB provides the bunched beam, an RFQ can start with the modulation, not at $-90°$, as illustrated in Figure 3.5b, but closer to the accelerating negative synchronous phase,

Table 5.7: Design parameters and its results.

Design Parameter	Value	Output Paremeter	Result
Input Energy [keV]	60	$\varepsilon_{x,n,\mathrm{rms}}$ [mm·mrad] $_{\|\Delta\phi\|\leq 5°}$	0.238
Frequency $(f-2f)$ [MHz]	54, 108	$\varepsilon_{y,n,\mathrm{rms}}$ [mm·mrad] $_{\|\Delta\phi\|\leq 5°}$	0.228
Beam Current [mA]	10 mA	$\varepsilon_{l,\mathrm{rms}}$ [keV·deg] $_{\|\Delta\phi\|\leq 5°}$	8.058
Synchronous Phase	−90°, +90°	$\varepsilon_{l,\mathrm{rms}}$ [keV·ns] $_{\|\Delta\phi\|\leq 5°}$	0.414
SCC %	90, 0, 85	Capture % $_{\|\Delta\phi_f\|\leq 20°}$	80.98
L_1, L_2 [mm]	83.4, 507.8	Capture % $_{\|\Delta\phi_f\|\leq 10°}$	76.73
V_1, V_2 [kV]	2.18, 0.92	Capture % $_{\|\Delta\phi\|\leq 5°}$	73.84
		Capture % $_{\|\Delta\phi_f\|\leq 4°}$	72.93
		Capture % $_{\|\Delta\phi_f\|\leq 3°}$	70.77
		Capture % $_{\|\Delta\phi_f\|\leq 2°}$	60.76

e.g. $\phi_s \approx -60°$. Concerning this advantage, vane design and production would be easier due to having a bigger starting cell size than the original one. Besides, the voltage applied on the vane can start at the acceleration process with higher modulation factor of m by reducing the bunching process; hence, in addition to the manufacturing feasibility, it provides one more advantage in reduced power loss due to shortening the RFQ cavity length. Since the DDHB system allows the bunch formation at subharmonics of the RFQ frequency, options for an efficient accelerator design are possible/available. In other words, a pre-bunched beam can be injected into an RFQ by filling only a subset of offered RFQ buckets. Several benefits can be achieved concerning cost efficiency and practical geometries bu such a method.

In the example presented in this section, two identical triplets illustrated in Figure 5.5 are used in the design as indicated in Figure 5.10. The distance between the first triplets and the buncher cavities is about 380 mm. While the strengths of the first triplet are 8.7, -13.95, and 8.7 [T/m], the ones for the second triplets are -15.2, 22.3, and -15.2 [T/m]. The settings in the design are different from those used in the previous example. Since the current of the input beam is relatively high in this design, the transverse beam at the beginning must be focused gently on the front side of the bunching cavities. Otherwise, in the process of bunching formation, the chromatic abbreviation might occur, and the output beam distribution in the focal plane becomes disturbed. Besides this optical restriction, the transverse envelope must also be fit according to the smallest aperture in the system in order to avoid beam loss at the cavity wall, which that aperture belongs to the second buncher, as
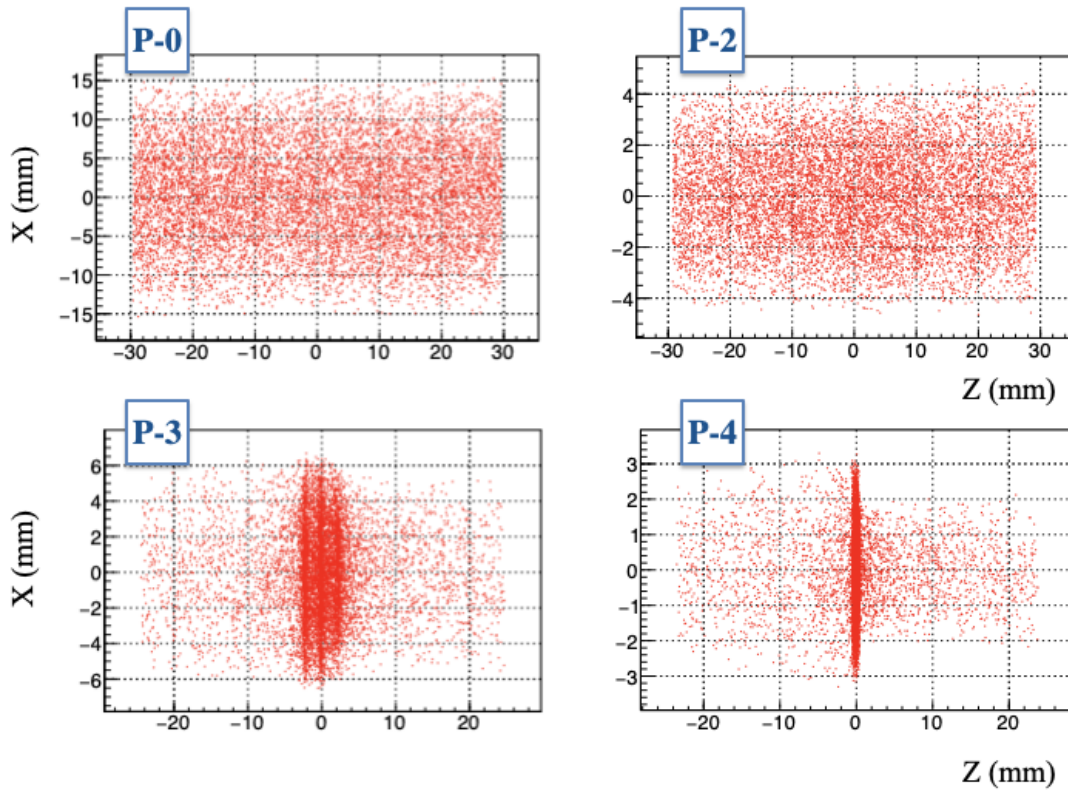
shown in the buncher layout in Figure 5.6.

Figure 5.11: The particle distributions in $X - Z$ plane with according positions shown in Figure 5.10.

Figure 5.11 demonstrates how the particle distribution behaves in the $X - Z$ plane along the structure associated with the numbers in Figure 5.10 when Figure 5.12 indicates the impacts in the longitudinal phase space of the buncher cavities in the positions numbered $P2$ and $P3$. Although the particle distribution in the spatial plane numbered with $P4$ indicates the smooth bunched beam at the end of the structure, the plot $P3$ in the figure illustrates three distinctive clusters. It is worth mentioning the reason that the particles create separated groups after the buncher cavities due to the energy difference provided by the applied voltage from the buncher cavities. In order to allocate/gather all particles in the central plane, the effect of mandatory second drift space, as offered in the DDHB concept, is obviously seen in this example.

While a typical RFQ phase width in the bunching process is about $\pm 25°$, this design with the concept of DDHB can provide much less phase window than the
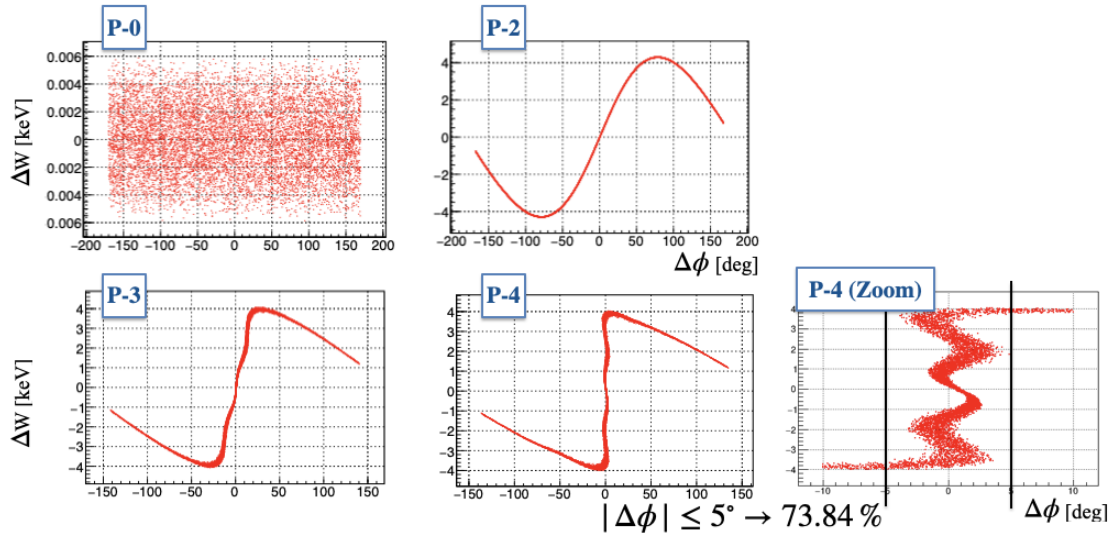
Figure 5.12: The longitudinal relative phase space plots.

RFQ case, in which the range is around $\pm 5°$. Although the capture rates of the design correspond to a relatively lower percentage than the RFQ one, the consequent particle captures of the structure as written in Table 5.7 are quite flexible with respect to the phase width from $\pm 3°$ to $\pm 20°$ by keeping the energy spread in ± 4 keV (6.6%).

In conclusion, a compact structure designed with the DDHB concept can fulfill a very sharp longitudinal beam focus with a small emittance and a fair capture rate of around 75%. For applications with a beam of medium current and medium beam energy, especially in the case of RFQ injection, a pre-bunched beam can provide a shorter length of the RFQ, which allows a more flexible vane-structure in the production stage, and an order of frequency transformation between the buncher and RFQ systems can fulfill special operations like high current beam injection into a cyclotron.

5.3.3 High current (30 mA) 100 keV Proton Beam Application

In the research on nuclear physics and industrial applications, particle accelerators in high-current ion beam demand high particle transmission and reduced longitudinal emittance. In general, such an accelerator line consists of a LEBT section, an RFQ, and a DTL, like the p-linac at GSI/FAIR [36], and the DTL needs to be fed by a small longitudinal emittance, matching its design acceptance. The DDHB concept in this section proposes an alternative feeding to the DTL by eliminating the RFQ machine. Since this concept provides a pre-bunched beam with a narrow phase width (small emittance), one example with a 100 keV, 30 mA proton beam with the parameters written in Table 5.8 is simulated to support the idea/proposal.
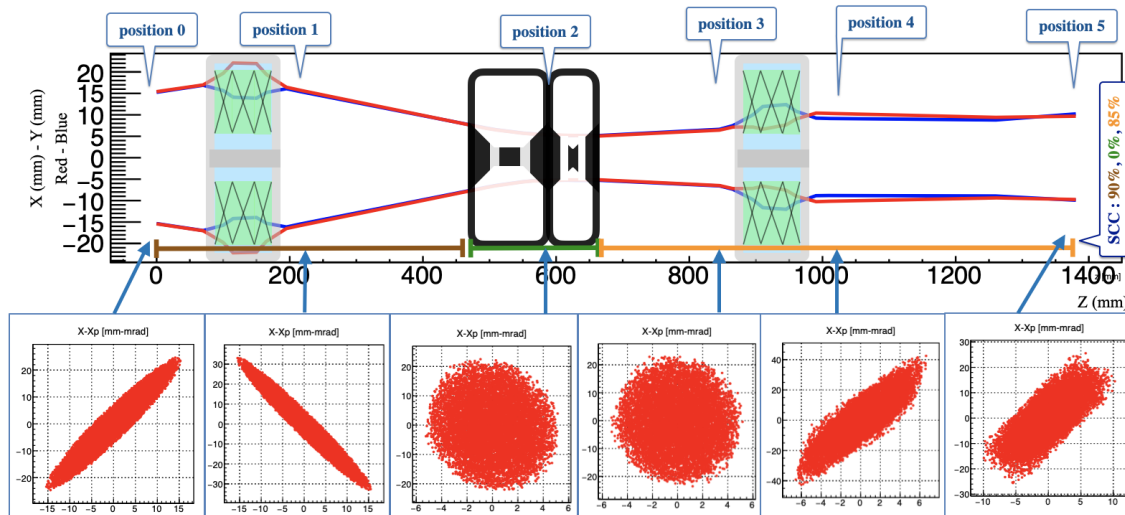

Figure 5.13: Example of one DDHB design simulated with the BCDC code. The plot shows the transverse beam envelope for a 100 keV, 30 mA proton beam and the transversal phase space distributions in the XX'-plane with the indicated positions.

In the example, the design includes two same-sized triplets as illustrated in Figure 5.13. The distance between the first triplets and the buncher cavities is about 280 mm. While the first triplet has strengths of 11.68, -18.75, and 11.68 [T/m], the second one has strengths of -15.4, 23.8, and -15.4 [T/m]. In a similar approach to the example explained in the previous section, the beginning quadrupole arrays were adjusted according to avoid the chromatic abbreviation in the structure and the small aperture of the second buncher.

Table 5.8: Design parameters and its results.

Design Parameter	30 mA	Output Paremeter	Result
Input Energy [keV]	100	$\varepsilon_{x,n,\text{rms}}$ [mm·mrad] $_{|\Delta\phi| \leq 20°}$	0.306
Frequency $(f - 2f)$ [MHz]	54, 108	$\varepsilon_{y,n,\text{rms}}$ [mm·mrad] $_{|\Delta\phi| \leq 20°}$	0.305
Beam Current [mA]	30 mA	$\varepsilon_{l,\text{rms}}$ [keV·deg] $_{|\Delta\phi| \leq 20°}$	32.951
Synchronous Phase	$-90°, +90°$	$\varepsilon_{l,\text{rms}}$ [keV·ns] $_{|\Delta\phi| \leq 20°}$	1.695
SCC %	90, 0, 85	Capture % $_{|\Delta\phi_f| \leq 20°}$	85.09
L_1, L_2 [mm]	110.2, 740.1	Capture % $_{|\Delta\phi_f| \leq 10°}$	47.99
V_1, V_2 [kV]	5.0, 2.3	Capture % $_{|\Delta\phi_f| \leq 5°}$	22.81
		Capture % $_{|\Delta\phi_f| \leq 4°}$	18.24
		Capture % $_{|\Delta\phi_f| \leq 3°}$	13.81
		Capture % $_{|\Delta\phi_f| \leq 2°}$	9.21

The particle distributions along the structure corresponded positions labeled with numbers in Figure 5.13 are demonstrated in the $X - Z$ plane in Figure 5.14, and in the energy-phase plane in Figure 5.15. The positions numbered $P2$ and $P3$ indicate
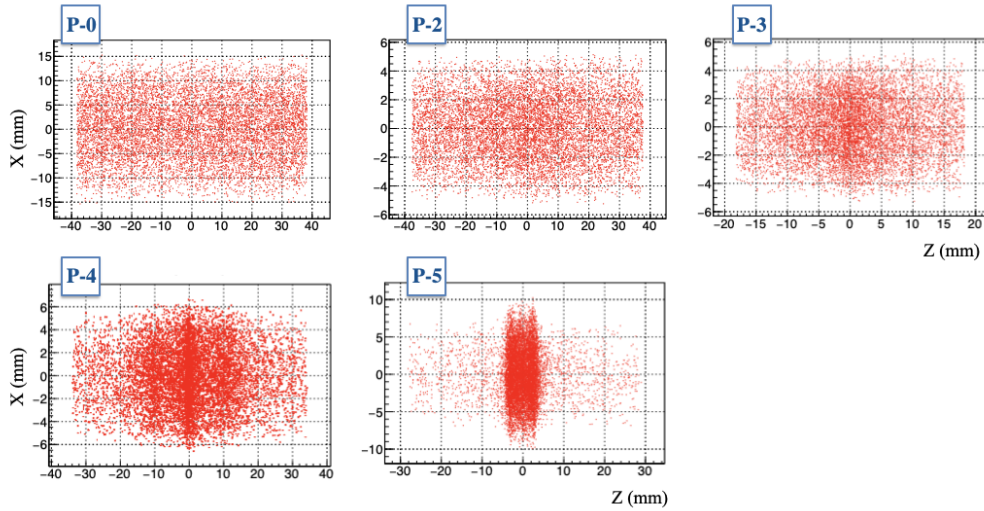

Figure 5.14: The particle distributions in $X - Z$ plane at positions shown in Figure 5.13.

the output distribution of f- and 2f-bunchers, and the particle cluster for $P3$ and $P4$ show to starting stage of the bunching process. The last position, $P5$, where the longitudinally bunched beam is focused, clearly explains the necessity of the end-drift in the DDHB concept. The outcome of these processes is to have a relatively high particle transmission of 85% in the phase window of $\pm20°$ within a length of the buncher system of 0.8 m. Moreover, the energy spread at the end is around 8%.

The adequate energy spread can be matched, and should be specified depending on applications. This consequence of the design has great potential to be a front-end of a DTL injection.
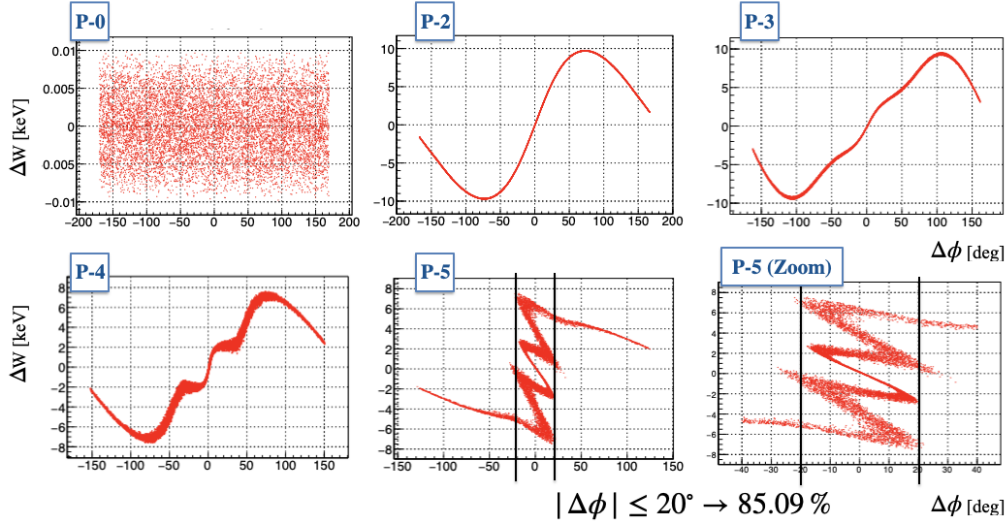

Figure 5.15: The longitudinal relative phase space plots.

In order to check the flexibility and/or limitation of this design, two alternative cases, as listed in the parameters in Table 5.9, were performed separately using the identical structure above. The one case is for a narrower acceptance width of $\pm 10°$, instead of $\pm 20°$, while the other is for a zero-current input beam. The output plots of the three simulations are shown in Figure 5.16.

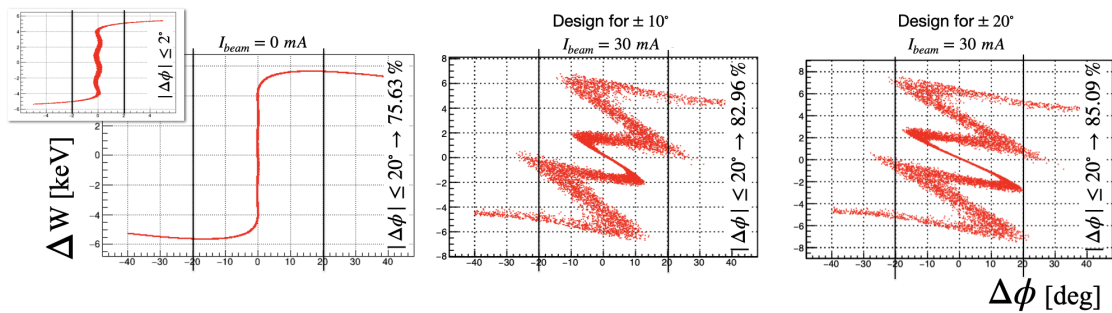
Figure 5.16: The output particle distributions for 0 mA and 30 mA ($\pm 10°$ and $\pm 20°$ acceptances) with zoom in $\pm 40°$ phase window.

Concerning the zero-current input beam, the bunch width is considerably shorter. Although the concept verifies its robustness according to beam current, as seen in

the acceptance rates for $\pm 2°$ in Table 5.9, the difference in capture rates of these two designs (0 mA and 30 mA for $\pm 20°$) indicates that the space charge inside the beam improves the bunch formation by capturing more particles into a widen phase width. A similar comparison and the purpose is presented in the conference IPAC23 [37]. On

Table 5.9: Parameters and results of the settings for the examples shown in Figure 5.1.

Parameter		Setting 1: 0 mA $|\Delta\phi_f| \leq 2°$	Setting 2: 30 mA $|\Delta\phi_f| \leq 10°$	Setting 3: 30 mA $|\Delta\phi_f| \leq 20°$
Input Energy [keV]		100	100	100
Frequency $(f-2f)$ [MHz]		54, 108	54, 108	54, 108
Beam Current [mA]		0	30	30
Synchronous Phase		$-90°, +90°$	$-90°, +90°$	$-90°, +90°$
SCC %		90, 0, 85	90, 0, 85	90, 0, 85
L_1,L_2 [mm]		110.2, 740.1	110.2, 740.1	110.2, 740.1
V_1,V_2 [kV]		2.65, 0.92	4.70, 2.15	5.0, 2.3
Capture %	$|\Delta\phi_f| \leq 2°$	**60.74**	13.23	9.21
Capture %	$|\Delta\phi_f| \leq 3°$	62.49	20.24	13.81
Capture %	$|\Delta\phi_f| \leq 4°$	64.00	27.18	18.24
Capture %	$|\Delta\phi_f| \leq 5°$	65.54	34.11	22.81
Capture %	$|\Delta\phi_f| \leq 10°$	70.05	**64.53**	47.99
Capture %	$|\Delta\phi_f| \leq 20°$	75.63	82.96	**85.09**

the other hand, the case for $\pm 10°$ results in a relatively lower particle acceptance of 64% than the one of 82% for $\pm 20°$, as listed in Table 5.9. The possible reason for this poor outcome is that the design limitation for the phase width is highly dependent on the ratio of L_1/L_2 as mentioned at the beginning of the chapter. When this ratio in the design is around 0.15, the total length should be increased in order to get a narrower phase width of $\pm 10°$ by decreasing that ratio. Since the optimization of such a task has been already demonstrated in Section 5.2, the enhancement of this design is indicated for the capabilities of one-based design for three options. Nevertheless, the capture ratio for the $\pm 10°$ case has an improvement compared to the based design of $\pm 20°$.

Chapter 6

Summary and Outlook

In this thesis, an improved pre-bunching system as an injector for low- and medium-current ion beam applications has been reported. First, the proposed concept and the relation of its essential parameters have been described. The developed methodology has allowed us to design an effective, simplified bunching system for injecting into several RF accelerators, like RFQs, cyclotrons, DTLs, etc., by obtaining small output emittances and considerable transmission rates. The effectiveness and the geometrical feasibility of the improved bunching method have been studied with three different levels of beam currents (0 ,10 ,30 mA) and two input energies (60 ,100 keV) at the same fundamental frequency of 54 MHz.

The study of the DDHB concept shows that a design with this technique provides an efficient beam formation; moreover, in the presence of beam currents, the output properties might be even enhanced w.r.t. particle capture rate during the end-drift provided by the DDHB method. Concerning space charge, the core of the beam distribution, after generating the initial bunch formation, behaves differently from the tail parts. Since the velocity of tails is relatively different from the core (due to the energy spread of the particles), they can travel through the central plane. On the other hand, the space charge force acts against the bunch formation on the core so that the core distribution moves slower than the outer parts of the beam. This investigation on the proposed harmonic bunching system offers much potential for improving the outcomes and simplifying the structures of the bunching system.

With respect to space charge forces, the comprehension of the bunching process, starting from a DC beam, is one of the essential parts of beam physics. Many

commercial codes (e.g. LORASR [1] TraceWin [2]) provide simulations with the function of such a beam in operation; however, their approaches are mostly hidden. In other words, a user cannot know what kind of operation this program uses. Therefore, one main task of this thesis was to develop a dedicated multi-particle tracking beam dynamics code - BCDC by computing the space charge effect during the bunch formation, starting from a DC beam. The BCDC code contains elementary routines, like drift, accelerating gap, or magnetic lens, for particle tracking; moreover, the next-neighboring-bunches (NNB) routine has been developed for the accurate numerical calculation of the electric space charge fields. By integrating only two next neighboring boxes into the main box, the impact of the space charge can be computed very precisely. It was checked that outer bunches have a minor effect at conditions, as discussed here. So all results of the designs in the thesis are presented by this dedicated tool of BCDC. Additionally, the BCDC program is also a powerful tool for simulations in the future on particular projects, while proof-of-principle designs were only developed in this thesis.

The applications in the thesis demonstrate that they provide flexibility to the output beam exclusively using the DDHB concept. Their designing aim is to reach high particle acceptance and/or narrow phase width depending on the following RF-accelerator. Since the main study is for high-current ion beam applications, the two examples with 60 keV,10 mA, and 100 keV,30 mA proton beams can allow for a beam injection into an RFQ unit with a significantly shortened and simplified front-end. Moreover, the design for the 100 keV,30 mA proton beams fulfills from a DDHB can provide the injection conditions into a drift tube linac. This alternative can be performed by changing the applied voltages at the buncher cavities, keeping the lengths L_1 and L_2 identical, and obtaining a narrower phase window than used in the RFQ case. Besides, in order to demonstrate the methodology in practice, one simulation is given by a 100 keV,1 mA proton beam for a conventional cyclotron injection. It was demonstrated that capture rates of around 70% can be reached into cyclotron phase acceptances as small as $\pm 5°$. Although numerous pre-bunching systems at low currents are operated at present, like at ATLAS, Argonne Lab. [29], and FRIB, MSU [30], their upgrades to higher current projects might profit from using a system based on the DDHB concept are described in this thesis.

Bibliography

[1] R. Tiede, G. Clemente, S. Minaev, H. Podlech, U. Ratzinger, and A. C. Sauer. LORASR code development. In *Proc. 10th European Conference, EPAC 2006, Edinburgh, UK*, volume 060626, pages 2194–2196, 2006.

[2] D. Uriot and N. Pichof. TraceWin Code.

[3] P. M. Lapostolle. Proton linear accelerators: A theoretical and historical introductions. In *Los Alamos Report LA-11601-MS*, 1989.

[4] D. Alesini. Linac. In *CERN Accelerator Introduction to Accelerator Physics (CAS 2019)*, 2021.

[5] N. C. Christofilos. Focussing system for ions and electrons, 1950. Patent-US2736799A.

[6] E. D. Courant, M. S. Livingston, and H. S. Snyder. The strong-focusing synchroton—a new high energy accelerator. *Phys. Rev.*, 88:1190–1196, Dec 1952. DOI:10.1103/PhysRev.88.1190.

[7] E. D. Courant and H. S. Snyder. Theory of the alternating-gradient synchrotron. *Annals of Physics*, 3(1):1–48, 1958. DOI:10.1016/0003-4916(58)90012-5.

[8] J. P. Blewett. The Focal Properties of Certain Quadrupole Lenses. Technical report, Brookhaven National Lab., Upton, N.Y., BNL-4654; ADD-JPB-13, 1959.

[9] U. Ratzinger. H-type Linac Structures. In *CERN Accelerator School RF Engineering (CAS 2005)*, 2005. DOI:10.5170/CERN-2005-003.351.

[10] H. Hähnel. Development of an ih-type linac for the acceleration of high current heavy ion beams. 2017. Dissertation, Johann Wolfgang Goethe Universität Frankfurt am Main.

[11] I. M. Kapchinskii and V. A. Teplyakov. A linear ion accelerator with spatially uniform hard focusing. pages 19–22. Prib. Tekh. Eksp., 1970. reportNumber: SLAC-TRANS-0099.

[12] J. Holzbauer, W. Hartung, F. Marti, E. Pozdeyev, and Q. Zhao. Electromagnetic design of a multi-harmonic buncher for the frib driver linac. In *Proc. Particle Accelerator Conference (PAC2011), New York, NY, USA*, 2011. PAC-2011-TUP091.

[13] T. P. Wangler. *RF Linear Accelerators.* John Wiley and Sons, Ltd, 2008. DOI:10.1002/9783527623426.ch1.

[14] C. Rossi, P. Bourquin, S. Cazaux, O. Delferriere, M. Desmons, R. Duperrier, A. France, J. B. Lallement, D. Leboeuf, A. M. Lombardi, S. Mathot, O. Piquet, M. Timmins, G. Vandoni, and M. Vretenar. The Radiofrequency Quadrupole Accelerator For The LINAC4. In *Proc. International Linear Accelerator Conference (LINAC'08), Victoria, BC, Canada*, 2008. MOP040.

[15] A. Schempp, M. Ferch, and H. Klein. A light ion four rod rfq injector. In *Proc. Particle Accelerator Conference (PAC1987), New York, NY, USA*, volume 870316, page 267, 1987. PAC1987-0267.

[16] P. Lapostolle and M. Weiss. Formulae and procedures useful for the design of linear accelerators. Technical report, CERN, Geneva, 2000.

[17] R. W. Hockney and J. W. Eastwood. *Computer Simulation Using Particles.* McGraw-Hill, London, 1981.

[18] A. Franchi, A. Bazzani, M. Comunian, A. Pisent, S. Rambaldi, and G. Turchetti. Halodyn: A 3d poisson-vlasov code to simulate the space charge effects in the high intensity trasco linac. In *Proc. 21st International Linear Accelerator Conference (LINAC02), Gyeongju, South Korea*, 2002.

[19] M. Reiser. *Theory and Design of Charged Particle Beams.* John Wiley and Sons, Ltd, 2008. DOI:10.1002/9783527622047.

[20] Wikipedia. Trilinear Interpolation. Last accessed March 2023.

[21] C. A. Valerio Lizarraga. Space charge compensation on the low energy beam transport of Linac4. 2015. Dissertation, CERN, https://cds.cern.ch/record/2047063.

[22] S. Humphries. *Charged particle beams*. Dover, Mineola, New York, 2013. 978-0-486-49868-3.

[23] D. Noll. Investigations on the transport of high-intensity beams using particle-in-cell simulations. 2016. Dissertation, Johann Wolfgang Goethe Universität Frankfurt am Main.

[24] B. Schlitt, A. Bechtold, U. Ratzinger, and A. Schempp. Design of the 7 MeV/u, 217 MHz Injector Linac for the Proposed Ion Beam Facility for Cancer Therapy at the Clinic in Heidelberg, 2000. MOD10.

[25] U. Ratzinger, A. Almomani, H. Hähnel, J. Kaiser, and R. Tiede. Combined zero degree structure beam dynamics and applications. In *Phys. Rev. Accel. Beams*, volume 22, page 114801. American Physical Society, 2019. DOI:10.1103/PhysRevAccelBeams.22.114801.

[26] R. Tiede, 2023. Private communication in 2023.

[27] R. Perry. Multiple Harmonic Buncher for a Linear Accelerator. In *Argonne Nat. LAb. Document - ANLAD74, Feb.1963 and Yale Conference on Linear Accelerators*, pages 279–287, 1963.

[28] C. Goldstein and A. Laisne. Third harmonic simulated buncher. In *Nuclear Instruments and Methods*, volume 61, pages 221–225, 1968. DOI:10.1016/0029-554X(68)90546-6.

[29] S.V. Kutsaev, R. Agustsson, D. Chao, S. Lynam, B. Mustapha, S. Sharamentov, and A.Yu. Smirnov. Four-harmonic buncher for radioactive and stable beams switching at the atlas facility. In *Nuclear Instruments and Methods in Physics Research Section A: Accelerators, Spectrometers, Detectors and Associated Equipment*, volume 905, pages 149–159, 2018.

[30] A.S. Plastun, P.N. Ostroumov, A.C.C. Villari, and Q. Zhao. Longitudinal Beam Dynamics in FRIB and ReA Linacs. In *Proc. 13th International Computational Accelerator Physics Conference (ICAP'18), Key West, FL, USA*, pages 330–334, 2019. DOI:10.18429/JACoW-ICAP2018-WEPAF04.

[31] L. M. Bollinger. Present status and probable future capabilities of heavy-ion linear accelerators. In *Proc. 10th International Conference on Cyclotrons and their Applications, East Lansing, Michigan, USA*, 1984.

[32] U. Ratzinger, R. Geier, S. Gustavsson, E. Nolte, and W. Schollmeier. The three-harmonics double-drift buncher at the munich heavy ion postaccelerator. In *Nuclear Instruments and Methods in Physics Research*, volume 205, pages 381–386, 1983. DOI:10.1016/0167-5087(83)90001-7.

[33] J. Knott, D. Warner, and M. Weiss. Adjustment of a Double Drift Harmonic Buncher and Bunch Shape Measurements. In *9th Proton Linear Accelerator Conference, CERN-PS-LIN-76-4*, 1976.

[34] U. Ratzinger. Effiziente hochfrequenz-linearbeschleuniger für leichte und schwere ionen. 1998. Habilitationsschrift, Johann Wolfgang Goethe Universität Frankfurt am Main.

[35] E. Sunar, U. Ratzinger, M. Syha, and R. Tiede. Harmonic Bunch Formation and Optional RFQ Injection. In *Proc. 31st International Linear Accelerator Conference (LINAC'22)*, pages 559–561, 2022. DOI:10.18429/JACoW-LINAC2022-TUPORI06.

[36] GSI. Proton linac project at fair, accessed on July 2023.

[37] E. Sunar, U. Ratzinger, and R. Tiede. The Double Drift Harmonic Buncher (DDHB) and Acceptance Investigations at Linac and Cyclotron Injections. In *Proc. 14th International Particle Accelerator Conference - IPAC'23*, pages 1740–1743, 2023. DOI:10.18429/jacow-ipac2023-tupa190.

Appendices

Appendix A

Trilinear Method

Consider that there is a cubic lattice with eight nodes labeled in C_{ijk} and the interpolation point C with coordinates of $C(x,y,z)$. The smaller differences in point C and the corners are represented with the subscript d as:

$$x_d = \frac{x - x_0}{x_1 - x_0} \quad , \tag{A.1}$$

$$y_d = \frac{y - y_0}{y_1 - y_0} \quad , \tag{A.2}$$

$$z_d = \frac{z - z_0}{z_1 - z_0} \quad , \tag{A.3}$$

where x_0 denotes the below position of $C(x,y,z)$ from the lattice points, x_1 represents the above position of $C(x,y,z)$ from the lattice points, y_0,y_1,z_0,z_1 are described in a similar way.

Starting with the interpolation in the $x-$direction, assume that the front and backward faces of the lattice are numerically tagged as 0 and 1. For example, when $C(x,y,z)$ along x-plane is intersected as shown in Figure A.1b, C_{0jk} defines the front intersection points. Thus, the function value of (x_0, y_0, z_0) can be written as:

$$c_{00} = c_{000}(1 - x_d) + c_{100}x_d \quad , \tag{A.4}$$

$$c_{01} = c_{001}(1 - x_d) + c_{101}x_d \quad , \tag{A.5}$$

$$c_{10} = c_{010}(1 - x_d) + c_{110}x_d \quad , \tag{A.6}$$

$$c_{11} = c_{011}(1 - x_d) + c_{111}x_d \quad , \tag{A.7}$$

After the x-direction, these values would be interpolated with the y-direction as given equations below:

$$c_0 = c_{00}(1 - y_d) + c_{10}y_d \quad , \tag{A.8}$$

$$c_1 = c_{01}(1 - y_d) + c_{11}y_d \quad . \tag{A.9}$$

Eventually, the interpolation along the z-direction would be added to the equations above:

$$c = c_0(1 - z_d) + c_1 \cdot z_d \quad . \tag{A.10}$$

The outcome of the trilinear interpolation does not depend on the order of these steps. In any other order of the three axes, the resulting interpolation brings similar values.

(a) The 8-corners with the point C.   (b) The sketch of 3D interpolation.
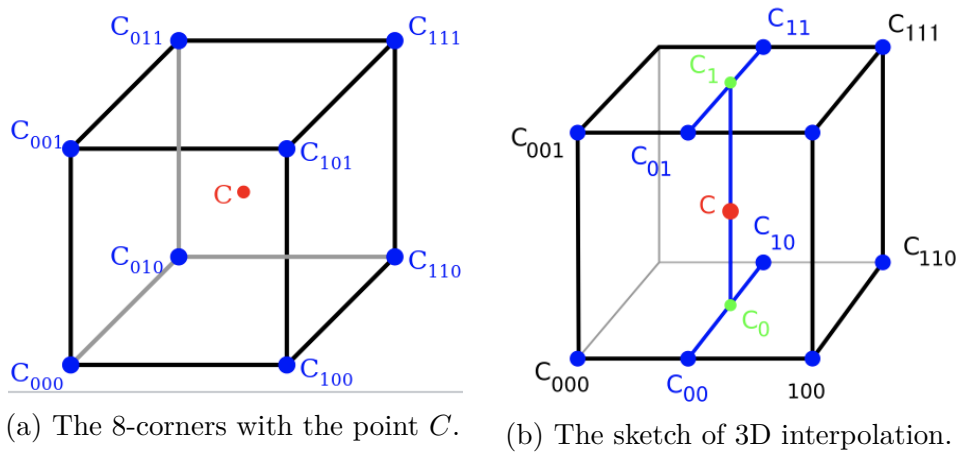
Figure A.1: The image at the left illustrates the cubic lattice of the eight corner points and the interpolation point C. The picture at the right indicates the same cube with the intersections nodes of point C [20].

Appendix B

Statistical Study in Field Computation and Interpolation

In the analysis of field calculations, in section 3.5.1, an interpolation method using a discrete set of grid points has been preferred to reduce computing complexity and to construct intermediate values necessitating that technique. By examining Figure 3.22, it becomes evident that the absence of interpolation leads to results characterized by a pronounced staircase model, particularly as the number of particles increases. This phenomenon reflects the inherent limitations of numerical simulations as statistical studies. In order to avoid the presence of a staircase model and to achieve smoother field calculations, the BCDC employs the triple interpolation method. Appendix A provides a comprehensive explanation of this method and its associated formulas. Although the trilinear interpolation assists in enhancing the accuracy of the simulations, the resulting field computations hold some thickness, as shown detailed in Figure 3.22, and Figure B.1 demonstrates the identical enlarging parts of the plots in Figure 3.22.

Considering to focus the central grid position, Figure B.1 indicates that the field calculations without and with the interpolation contain a similar thickness. Since this thick exists in both results, in order to investigate the reason, the study in this part would be performed by focusing on the one specified cell of the staircase model. The fact that the value of the field calculation in one cell demonstrates not one single value, as expected from the principle of the electric field inside a spherical volume, but an irregular fluctuation, as shown in the same figure. It is worth noting that the
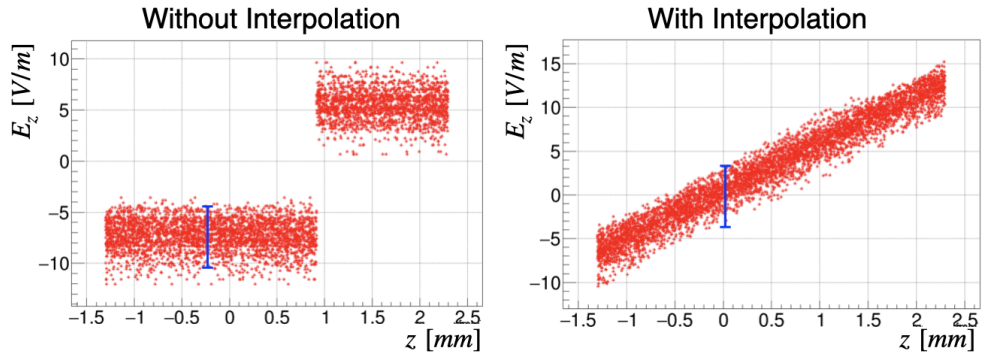
Figure B.1: The resulting field calculations focused on the central cell are plotted with and without integrated the trilinear interpolation method.

value in the center for the electric field should be zero; however, the centralized grid is not just positioned at the center, as clearly seen in Figures B.1 and B.2 (because meshing to cells in the algorithm starts from one border to another, not from the center).
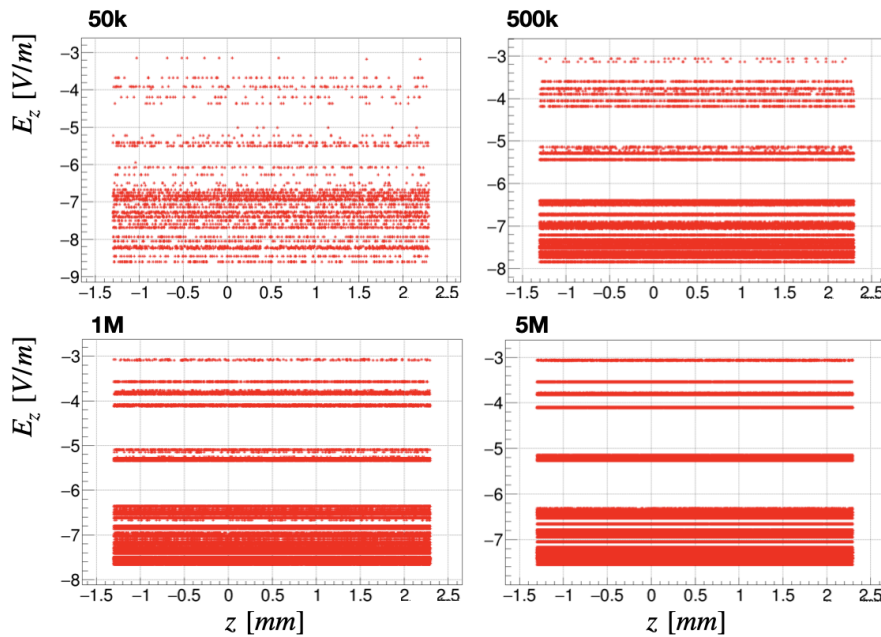

Figure B.2: The field calculations have been performed by increasing the macro particle numbers from 50k to 5M and these plots show the results focused on the central cell.

Furthermore to the investigation, three more simulations with higher numbers of macro-particles (500k, 1M, and 5M) have been performed. It is found that these

fluctuations are not random but discrete, as seen in Figure B.2. The expected single value becomes visible while increasing the macro-particle number, but there is more than one value. The reason is the plotting style, in which each line represents one cell at the same specified position in the z-direction, as indicated in the plots.
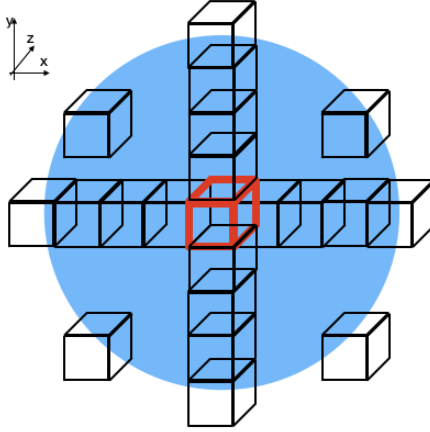
Figure B.3: The scheme represents the cross-section of the grid box. The red box is the central cell, where all computing plots belong to, and overlapped by the black surroundings contributed in the X-Y planes.

The schematic in Figure B.3 illustrates this impression. The chosen cell is highlighted in red, and the remained located black boxes are the contributors in the $X - Y$ planes overlapping the surroundings of the red box. Assuming this contribution, one line at the center and two near the borders of that cell have been chosen, and their resulting fields are drawn in Figure B.4.

When the particles on these lines are plotted in the spatial coordinates as in Figure B.5, it is clearly seen that these three lines represent the three different cells located around the selected cell $(x, y, z = 0)$.

As a final remark on Figure B.2, the simulation plots illustrate that some elevation between some lines occurs, which is more visible in the distributions of 1M and 5M particles. Since the particles are assigned into the cells by the method of CIC (cloud-in-cell) and with generating a weighting function, as shown in Figure 3.18a, inhomogeneous deposition occurs in this process, and the outer cells cause such a separation in the field computation.

After these investigations, one last step is tested by a small algorithm based on the particle-particle interaction method (courtesy of Dr. Rudolf Tiede). In such an
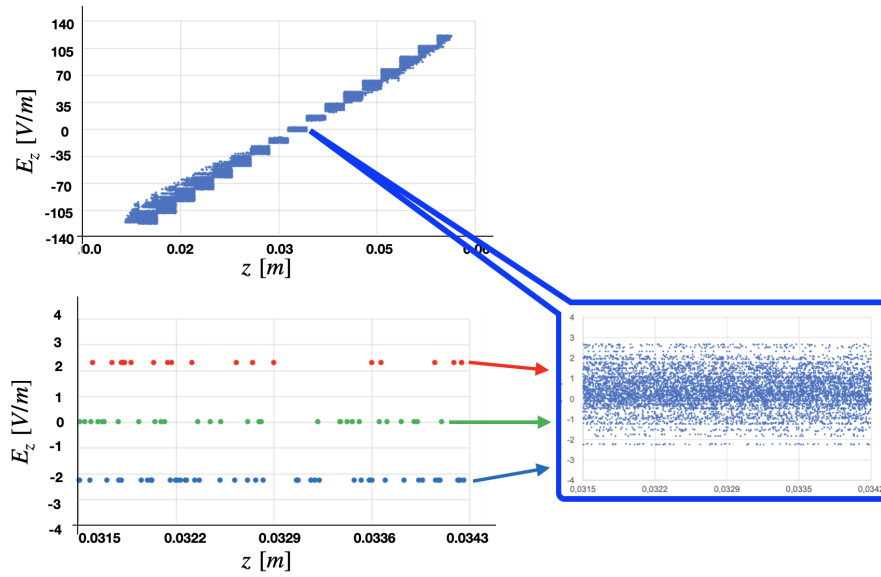
Figure B.4: The three chosen lines in the central cell. The red and blue lines are the chosen particles near the border of the cell and the green one is the particles located at the centre.
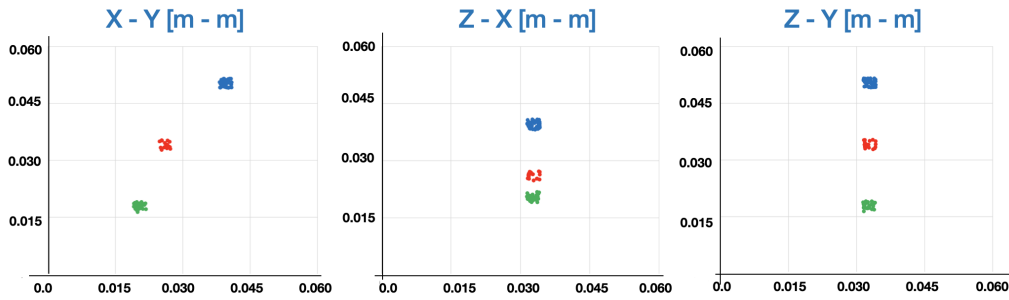

Figure B.5: The particle distributions on the chosen lines are plotted in the spatial coordinates.

algorithm, the computation of the particle interactions has required a limit length between two particles due to the formula of Coulomb's law. Otherwise, the electric field might easily go to infinity due to the ratio $\frac{1}{r^2}$ in that formula. Figure B.6 shows the field plots with respect to two different chosen sizes of that length; one-tenth of the mesh length and an equal length of the mesh. The plots in the figure indicate that the accuracy of the field computation changes with respect to the distance between two calculated particles. Moreover, the PPI method gives similar outcomes as the concept of PIC (particle-in-cell), shown in Figure B.6, where the results in both techniques contain the thickness.
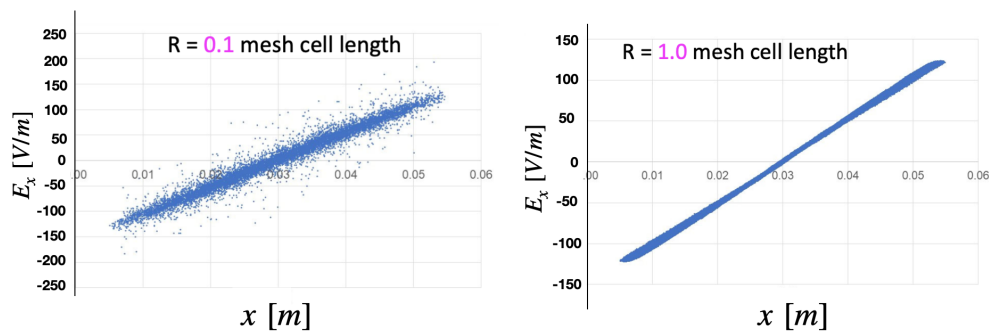
Figure B.6: The resulting field calculations by using particle-particle interaction method (courtesy of Dr. Rudolf Tiede).
The cell length represents to the distance used in the algorithm for the PIC method.

The cross-checked by another concept of the PPI, instead of the PIC, shows that statistical errors can occur independently of the numerical method. As a conclusion for the PIC method offered in the algorithm, the errors result from numerical (statistical) effects; hence, the field computation is highly dependent on the number of macro particles per cell and the number/size of meshes in the simulating box.

Acknowledgements